

Designing Advanced Functional Separators for  
High-performance Lithium-Sulfur Batteries

September 2019

He Yibo

Designing Advanced Functional Separators for  
High-performance Lithium-Sulfur Batteries

Graduate School of Systems and Information  
Engineering  
University of Tsukuba

September 2019

He Yibo

# ABSTRACT

Lithium-sulfur (Li-S) batteries have attracted considerable attention due to their high theoretical energy density. However, the undesirable polysulfides shuttle and overgrown lithium dendrites seriously hinder their practical applications. Separator is an essential component in rechargeable Li-S batteries. It not only can act as an isolator to prevent the electrical contact between cathode and anode, but also can serve as a reservoir of liquid electrolyte to regulate the diffusion of ions. Thus, employing the functional separators with ionic selectivity to simultaneously address the issues of polysulfides shuttle and lithium dendrites growth seems to be a reliable strategy. Herein, we have fabricated three-types functional separators and made corresponding investigations and analyses on their properties and electrochemical performance. Details are as follows:

Firstly, we construct a “polysulfide-phobic” surface by anchoring polysulfides anions on the VOPO<sub>4</sub> hosts. Due to the intrinsic electronegativity of polysulfides, the as-constructed “polysulfide-phobic” surface produces strong repulsion effect on the free polysulfide anions via Coulombic interactions, which is proved by the time/space-resolved operando Raman evidences and the visible permeation experiments. When we introduce the “polysulfide-phobic” interface between cathode and separator, the Li-S cell shows a high capacity retention of 75.3% with a low average capacity fading of 0.082% upon 300 cycles at 0.2 C.

Secondly, we use lithiated Nafion (Li@Nafion) with negatively charged -SO<sub>3</sub><sup>-</sup> instead of polysulfides-VOPO<sub>4</sub> to construct a more stable and efficient “polysulfide-phobic” surface. Meanwhile, we further introduce an Al<sub>2</sub>O<sub>3</sub> layer with uniform pore size between the lithium anode and routine separator (polypropylene/polyethylene/polypropylene, PEP) to aid in forming homogeneous Li ions fluxes, thus obtaining a

dendrite-free metallic-lithium anode. The Li-S with a Li@Nafion/PEP/Al<sub>2</sub>O<sub>3</sub> separator realizes a higher capacity retention (77.2%) with a lower capacity decay rate (0.022% per cycle) after 1000 cycles at an elevated rate of 1 C. Furthermore, the Li-S coin cells with high sulfur loadings (4.8 and 7.6 mg cm<sup>-2</sup>) also exhibit good electrochemical performance.

Thirdly, we develop a free-standing MOF@PVDF-HFP membrane instead of the tri-layered Li@Nafion/PEP/Al<sub>2</sub>O<sub>3</sub> separator. The highly ordered pore structure and narrow pore size window make the MOF@PVDF-HFP membrane not only can act as ionic sieve to inhibit polysulfides shuttle, but also can regulate uniform Li<sup>+</sup> fluxes to suppress the growth of lithium dendrites. After introducing a MOF@PVDF-HFP separator, the Li-S coin cell shows an ultralong long cycle life with low capacity decay of 0.015% per cycle upon 2000 cycles at 2 C. Moreover, the practical Li-S pouch cell with high sulfur loading (5.8 mg cm<sup>-2</sup>) also achieves a high reversible capacity (936 mA h g<sup>-1</sup>) after 200 cycles.

Through systematically studying the properties and comprehensively investing the electrochemical performance the three types of separators, it can be concluded that both the repulsion effect by Coulombic interactions and the blocking effect by physical barriers are able to mitigate the diffusion of polysulfide anions. Additionally, porous materials with small and uniform pore size can aid in regulating homogenous Li<sup>+</sup> fluxes to inhibit the growth of lithium dendrites. In this case, it seems that the materials with small and uniform pore size seem to be more reliable to develop the multifunctional separators for Li-S batteries. This research provides a new insight and way for constructing functional separators to develop advanced Li-S batteries.

# TABLE OF CONTENTS

ABSTRACT .....	I
TABLE OF CONTENTS .....	III
LIST OF FIGURES .....	VII
LIST OF TABLES .....	XV
Chapter 1. General introduction .....	1
1.1 Historical development of lithium-sulfur batteries .....	1
1.2 Configurations of lithium-sulfur batteries .....	2
1.2.1 Cathode.....	3
1.2.2 Anode .....	3
1.2.3 Separator.....	4
1.2.4 Electrolyte .....	5
1.3 Principles of lithium-sulfur batteries .....	7
Chapter 2. Technical challenges of lithium-sulfur batteries.....	9
2.1 Introduction .....	9
2.2 Insulating nature of sulfur .....	9
2.3 Shuttle of soluble polysulfides .....	10
2.4 Volume expansion of sulfur cathode .....	12
2.5 Degradation of the lithium-metal anode.....	12
Chapter 3. Effective strategies to address the issues in lithium-sulfur batteries .....	15
3.1 Introduction .....	15
3.2 Stabilizing sulfur cathodes .....	15

3.2.1 Porous carbon-based cathodes .....	16
3.2.2 Metal oxides/sulfides-based cathodes.....	17
3.2.3 Polymer-based cathodes .....	19
3.3 Protecting lithium-metal anodes .....	22
3.3.1 In-situ protection .....	22
3.3.2 Ex-situ protection.....	24
3.4 Modifying separators .....	25
3.4.1 Carbon-based separators.....	26
3.4.2 Inorganic metal oxides/sulfides-based separators.....	27
3.4.3 Organic polymer-based separators.....	29
Chapter 4. Target and outline of this dissertation.....	31
4.1 Motivation of this research .....	31
4.2 Target of this research .....	32
4.3 Outline of this thesis.....	33
Chapter 5. Building a “polysulfides-phobic” interface to restrain shuttle effect.....	35
5.1 Introduction.....	35
5.2 Experiment and characterization.....	37
5.2.1 Chemicals and materials .....	37
5.2.2 Synthesis of Li <sub>2</sub> S <sub>6</sub> in DOL/DME.....	37
5.2.3 Fabrication of flexible S <sub>6</sub> <sup>2-</sup> -VOPO <sub>4</sub> /PP membranes.....	37
5.2.4 Preparation of graphene@sulfur cathode materials.....	38
5.2.5 Lithium-sulfur cells assembly .....	39
5.2.6 Characterization.....	39
5.2.7 Raman Measurements .....	40

5.2.8 Ionic conductivity .....	40
5.2.9 Transference number of lithium ions .....	40
5.2.10 Electrochemical measurements .....	41
5.3 Results and discussions .....	41
5.3.1 Immobilization of polysulfides on VOPO <sub>4</sub> .....	41
5.3.2 The effect of S <sub>6</sub> <sup>2-</sup> -VOPO <sub>4</sub> on the polysulfide anions .....	46
5.3.3 Permselectivity of S <sub>6</sub> <sup>2-</sup> -VOPO <sub>4</sub> /PP membrane .....	50
5.3.4 Electrochemical performance of lithium-sulfur batteries .....	53
5.4 Summary .....	58
Chapter 6. Fabricating a tri-layer separator to restrain shuttle effect and inhibit lithium dendrites growth .....	59
6.1 Introduction .....	59
6.2 Experiment and characterization .....	61
6.2.1 Chemicals and materials .....	61
6.2.2 Synthesis of Li <sub>2</sub> S <sub>6</sub> in DOL/DME .....	61
6.2.3 Fabrication of Li@Nafion/PEP/Al <sub>2</sub> O <sub>3</sub> membranes .....	61
6.2.4 Li/Li symmetric cells assembly .....	62
6.2.5 Lithium-sulfur cells assembly .....	62
6.2.6 Characterization and electrochemical measurements .....	63
6.3 Results and discussions .....	63
6.3.1 Properties of Li@Nafion/PEP/Al <sub>2</sub> O <sub>3</sub> membrane .....	63
6.3.2 Ionic selectivity of Li@Nafion/PEP/Al <sub>2</sub> O <sub>3</sub> membranes .....	66
6.3.3 Lithium plating/stripping stability .....	68
6.3.4 Electrochemical performance of lithium-sulfur batteries .....	71
6.4 Summary .....	76

Chapter 7. Developing a free-standing membrane to simultaneously inhibit shuttle effect and Li dendrites growth .....	77
7.1 Introduction.....	77
7.2 Experiment and characterization.....	78
7.2.1 Chemicals and materials .....	78
7.2.2 Synthesis of Li <sub>2</sub> S <sub>6</sub> in DOL/DME.....	79
7.2.3 Fabrication of MOF@PVDF-HFP membranes .....	79
7.2.4 Li//Li symmetric cells assembly.....	79
7.2.5 Lithium-sulfur coin cells assembly.....	80
7.2.6 H-type lithium-sulfur glass cells assembly .....	80
7.2.7 Lithium-sulfur pouch cells assembly .....	81
7.2.8 Characterization and electrochemical measurements .....	81
7.3 Results and discussions .....	81
7.3.1 The morphology and structure of MOF@PVDF-HFP membranes.....	81
7.3.2 MOF@PVDF-HFP membrane as an ionic sieve.....	86
7.3.3 Lithium plating/stripping stability .....	89
7.3.4 Electrochemical performance of lithium-sulfur batteries .....	92
7.3.5 The characterization of MOF@PVDF-HFP after cycling .....	98
7.4 Summary.....	101
Chapter 8. Conclusions .....	103
List of research results .....	106
Acknowledgements.....	108
REFERENCES .....	110

# LIST OF FIGURES

Figure 1.1 World's energy demand increased rapidly .....	1
Figure 1.2 Schematic illustration of the inner structure of a Li-S battery.....	3
Figure 1.3 Lithium salts for preparing the electrolyte of Li-S batteries. ....	6
Figure 1.4 Organic solvents for preparing the electrolyte of Li-S batteries.....	6
Figure 1.5 The schematic of operation mechanism in a single Li-S cell and its typical discharge-charge voltage profile <sup>24</sup> in ether-based electrolytes.....	7
Figure 2.1 The intrinsic and extrinsic problems of Li-S batteries .....	9
Figure 2.2 Schematic illustration of shuttle of dissolved polysulfide ions <sup>39</sup> .....	11
Figure 2.3 Schematic illustrates the formation of lithium dendrites. ....	13
Figure 2.4 Schematic illustrates the problems caused by the lithium dendrites. ..	13
Figure 3.1 Schematic illustrations of confining polysulfides in cathode via physical constraint or chemical bonding.....	15
Figure 3.2 (a) A schematic diagram of the sulfur (yellow) confined in CMK-3, (b) charge/discharge profiles of CMK-3/S electrode. <sup>58</sup> (c) TEM image and corresponding elemental maps of a DHCS-S sphere. <sup>59</sup> (d) A schematic diagram and corresponding TEM image of CMK-3/S@PANS@TPS particle, (e) cycling performance of various electrodes at 0.25 C. <sup>60</sup> ...	17
Figure 3.3 (a) LiPSs diffuse out of cathode and are immobilized on perovskite (PrNP) promoter, facilitating their redox reaction. <sup>61</sup> (b) Visualized adsorption of Li <sub>2</sub> S <sub>4</sub> on graphene and CoS <sub>2</sub> . <sup>62</sup> (c) SEM image of ZnO@S/CNT. <sup>63</sup> (d) Cycle stability of various cathodes at 1600 mA g <sup>-1</sup> . <sup>63</sup> .....	18
Figure 3.4 (a) Schematic illustrates fabrication of PAH/PAA/(PEO/PAA) by the layer- by-layer (LbL) deposition. <sup>64</sup> (b) Synthetic scheme of S <sub>8</sub> with DIB to form	

sulfur copolymers.<sup>65</sup> (c) SEM images of the S-TTCA-I.<sup>66</sup> (d) Cycling performance with a charge/discharge profile inset.<sup>65</sup> (e) The cycling performance and Coulombic efficiencies of Li-S cells with different cathodes.<sup>66</sup> ..... 21

Figure 3.5 Schematic of the morphologies of lithium deposited on the substrate (a) without lithium polysulfide and (b) with lithium polysulfide. SEM images of cycled lithium metal electrodes (c) without and (d) with the addition of  $\text{Li}_2\text{S}_8$  (0.18 M). Scale bars, 20  $\mu\text{m}$ .<sup>67</sup> (e) Schematic of the cell with the  $\text{Li}_3\text{N}$  layer, (f) the charge-discharge profiles and (g) cycling performance of Li-S batteries with different lithium anodes at 0.2 C.<sup>68</sup> ..... 22

Figure 3.6 (a) Schematic diagrams of stabilizing the lithium metal by a hollow carbon nanosphere layer, (b) cross-section SEM image of the carbon spheres coated lithium metal.<sup>74</sup> (c) Optical images of lithium foil surface exposed in atmosphere, (d) cycling performance of Li-S cells with different lithium anodes.<sup>75</sup> ..... 25

Figure 3.7 (a) Schematic illustration of Li-S cell with a carbon-based separator, (b) long-term cycling performance of various separators at 0.6 C.<sup>80</sup> (c) SEM image of carbon-coated Glass Fiber with its photograph inset, (d) Cycling performance of Li-S cells with PGF and CGF at a current density of 0.2 C.<sup>81</sup> ..... 26

Figure 3.8 (a) Schematic illustration of Li-S cell with a  $\text{MoS}_2$ /Celgard separator, (b) cross section SEM image of a  $\text{MoS}_2$  layer, (c) cycling performance of the Li-S cells with different separators at 0.5 C.<sup>82</sup> ..... 28

Figure 3.9 (a) Schematic of Li-S cell with an ion selective separator, in which the separator allows the  $\text{Li}^+$  transport while blocks the diffusion of polysulfide

anions, (b) SEM image of Nafion-PP/PE/PP membrane. <sup>77</sup> (c) Charge/discharge profiles and (d) cycling performance of the cell with different separators at 1 C. <sup>83</sup> .....	29
Figure 4.1 Fabricating a functional separator that can simultaneously suppress the polysulfides shuttle and the growth of lithium dendrites. ....	32
Figure 4.2 The research routes and main target of this research. ....	32
Figure 5.1 Schematic illustrations of constructing (a) a hydro-phobic surface by anchoring hydrophobic groups on the substrate and (b) a polysulfide-phobic surface by immobilizing polysulfides on the polar materials. ....	36
Figure 5.2 (a) XRD pattern and (b) FE-SEM image of layered VOPO <sub>4</sub> ·2H <sub>2</sub> O .....	42
Figure 5.3 The color change of a Li <sub>2</sub> S <sub>6</sub> solution after introducing VOPO <sub>4</sub> sheets with the increase of rest time. ....	42
Figure 5.4 (a) Wide-scan survey XPS spectra of pristine VOPO <sub>4</sub> and S <sub>6</sub> <sup>2-</sup> -VOPO <sub>4</sub> . (b) S 2p and (c) V 2p elemental XPS spectra of S <sub>6</sub> <sup>2-</sup> -VOPO <sub>4</sub> . ....	43
Figure 5.5 (a) Raman peak assignments for S-S and V-S stretching modes within obtained spectra. (b) Raman spectra collected on the surface of VOPO <sub>4</sub> after different aging time. (c) Raman peak assignments: at the pristine state (black trace) and after 2 hours aging (blue trace), respectively. (d) Time-dependence of specific Raman peak intensities, which directly read from the operando spectra. ....	45
Figure 5.6 The relationship between the amount of VOPO <sub>4</sub> and the adsorbed amount of polysulfides. ....	46
Figure 5.7 Zeta potential results of (a) the pristine VOPO <sub>4</sub> powder and (b) the S <sub>6</sub> <sup>2-</sup> -VOPO <sub>4</sub> dispersed in 2-propanol. ....	47
Figure 5.8 (a) Above: schematic illustration the operation process of Raman information; below: the obtained Raman spectra at different distances away from	

VOPO<sub>4</sub>/polysulfide solution interface. (b) The enlarged Raman spectra in the square of (a). Because of the too big size of Raman laser spot (1~2 μm), the Raman information/signal obtained from near the interface is inevitably composed of both surface adsorbed polysulfides and dissolved polysulfide anions. (c) Time/space (x/y-axis) resolved contour plots evolution of specific Raman peak intensities. (d) The concentrations of adsorbed/dissolved polysulfide at different place with the schematic of repulsion effect of the VOPO<sub>4</sub> surface anchored with towards the free polysulfides anions in the solution..... 49

Figure 5.9 (a) Digital photos, (b) top-view and (c) side-view FE-SEM images of VOPO<sub>4</sub>/PP membrane. (d) FE-SEM image of S<sub>6</sub><sup>2-</sup>-VPP separator with the corresponding elemental maps of V and S within the squared area. (e) Electrochemical impedance spectra of PP and S<sub>6</sub><sup>2-</sup>-VPP separators..... 50

Figure 5.10 (a) Schematic diagram of V-type device. Optical images of the diffusion of polysulfides: visualized V-type glass devices with (b) a routine PP separator and (c) a S<sub>6</sub><sup>2-</sup>-VPP separator. .... 51

Figure 5.11 The characteristic of Li<sup>+</sup> transference number. (a) Polarization curves of symmetric cells with different separators. Electrochemical impedance spectra (b) with pure PP separator and (c) with S<sub>6</sub><sup>2-</sup>-VPP separator, respectively. The insets of EIS spectra for the batteries with different separators are the equivalent circuit models. R<sub>0</sub>: resistance of the electrolyte, R<sub>ct</sub>: charge transfer resistance at the electrodes, CPE: constant phase element about the double layer capacitance, W<sub>0</sub>: Warburg impedance. .... 52

Figure 5.12 (a) The inner structure, (b) cycling performance, and (c) corresponding charge/discharge curves at 0.1 C of the cell with a S<sub>6</sub><sup>2-</sup>-VPP membrane as separator and a carbon paper without S as cathode. .... 54

Figure 5.13 The inner structure of the assembled Li-S coin cell.....	55
Figure 5.14 (a) The rate performance of Li-S cells with different separators. (b) Voltage profiles of Li-S cell with a $S_6^{2-}$ -VPP separator. ....	55
Figure 5.15 (a) Comparison of cycling performance of Li-S cells with different separators. (b) Selective CV curves of Li-S cells with a $S_6^{2-}$ -VPP separator at 0.2 mV $s^{-1}$ ... ..	57
Figure 5.16 PXRD patterns of $S_6^{2-}$ -VPP separator before and after cycling. Inset presents the FE-SEM image of $S_6^{2-}$ -VPP separator after cycling.....	58
Figure 6.1 (a) Building a “polysulfide-phobic” surface to prevent the diffusion of polysulfides in chapter 5. (b) Building a “polysulfide-phobic” surface by Li@Nafion and introducing an $Al_2O_3$ layer to simultaneously restrain the polysulfides shuttle and lithium dendrites growth in chapter 6.....	59
Figure 6.2 SEM images of (a) PEP membrane, (b) Li@Nafion layer with loading of 1.0 $mg\ cm^{-2}$ and (c) $Al_2O_3$ layer. (d) Cross-section SEM image of Li@Nafion/PEP/ $Al_2O_3$ with Li@Nafion loading of 1.0 $mg\ cm^{-2}$ . SEM images of Li@Nafion layer with loading of (e) 0.3 and (f) 2.9 $mg\ cm^{-2}$ . ...	64
Figure 6.3 (a) Electrochemical impedance spectra and (b) corresponding ion conductivities of various separators.....	64
Figure 6.4 (a) $N_2$ adsorption/desorption isotherms and (b) corresponding pore size distributions of $Al_2O_3$ layer. ....	65
Figure 6.5 The optical photographs of various separators with the liquid electrolyte after different time. ....	66
Figure 6.6 The visualized V-type glass devices with various separators. The insides of the left and right chambers are DOL/DME with and without $Li_2S_6$ , respectively. ....	67

Figure 6.7 The characteristic of $\text{Li}^+$ transference number. (a) The potentiostatic polarization curve of Li-S cell with a LNPA separator. (b) The electrochemical impedance spectra before and after polarization.....	68
Figure 6.8 Schematic diagram of the inner structure of Li//Li symmetric cell. ....	68
Figure 6.9 Li stripping/plating performance in Li//Li symmetric cells at $2 \text{ mA cm}^{-2}$ ( $5 \text{ mA h cm}^{-2}$ ) with different separators. (a) PEP, (b) Li@Nafion/PEP, (c) PEP/ $\text{Al}_2\text{O}_3$ , and (d) Li@Nafion/PEP/ $\text{Al}_2\text{O}_3$ . (e) Li plating/stripping behaviour of cell with a Li@Nafion/PEP/ $\text{Al}_2\text{O}_3$ separator at high current-density of $5 \text{ mA cm}^{-2}$ ( $2.5 \text{ mA h cm}^{-2}$ ). ....	70
Figure 6.10 The cycled lithium metal electrodes from the cells with various separators: (a, b) PEP, (c, d) Li@Nafion/PEP, (e, f) PEP/ $\text{Al}_2\text{O}_3$ , and (g, h) Li@Nafion/PEP/ $\text{Al}_2\text{O}_3$ . ....	71
Figure 6.11 (a) The rate performance of Li-S cells with different separators. (b) Voltage profiles of Li-S cell with a Li@Nafion/PEP/ $\text{Al}_2\text{O}_3$ separator. ....	72
Figure 6.12 (a) The discharge capacities and (b) capacity retentions of the Li-S cells with various separators. ....	73
Figure 6.13 The initial charge/discharge profiles of the Li-S cells with Li@Nafion/PEP/ $\text{Al}_2\text{O}_3$ separators with high sulfur loadings of (a) $4.8$ and (b) $7.6 \text{ mg cm}^{-2}$ at $0.05 \text{ C}$ . (c) The cycling performance of the cell with high sulfur loadings at $0.2 \text{ C}$ . ....	75
Figure 7.1 Developing (b) a free-standing MOF@PVDF separator instead of (a) the tri-layered separator to simultaneously inhibit shuttle effect and lithium dendrites growth .....	77
Figure 7.2 Schematic illustration of the preparation process of a free-standing MOF@PVDF-HFP membrane. ....	82

Figure 7.3 (a) Digital photos, (b) FE-SEM image with elemental maps of Cu and F, and (c) cross-section FE-SEM image of MOF@PVDF-HFP separator.....	82
Figure 7.4 PXRD patterns of PVDF-HFP, MOF particles and MOF@PVDF-HFP. ....	83
Figure 7.5 FT- IR spectra of PVDF-HFP, MOF particles and MOF@PVDF-HFP. ....	84
Figure 7.6 TGA curves PVDF-HFP, MOF particles and MOF@PVDF-HFP.....	85
Figure 7.7 (a) N <sub>2</sub> adsorption/desorption isotherms with the corresponding pore size distributions of (b) pure MOF and (c) MOF@PVDF-HFP membranes. ....	86
Figure 7.8 (a) The schematic image of visible H-type Li-S glass cell. Optical images of visible H-type cells with (b) PP separator and (c) MOF@PVDF-HFP separator during a discharging process. ....	87
Figure 7.9 (a) The characteristic of Li <sup>+</sup> transference number: polarization curves of symmetric cells with different separators. The EIS spectra of the cell with (b) a PP separator and (c) a MOF@PVDF-HFP separator before and after polarization.....	88
Figure 7. 10 Electrochemical impedance spectra of MOF@PVDF-HFP separator. ....	88
Figure 7.11 (a) Lithium plating/stripping stability of the symmetric cell with PP separator and MOF@PVDF-HFP separator. (b) Lithium plating/stripping stability of the cell with a MOF@PVDF-HFP separator at a high current density of of 10 mA cm <sup>-2</sup> with the selected voltage profiles insets. ....	90
Figure 7.12 Digital photos of the detached Li//Li symmetric cells with (a) a PP separator and (b) a MOF@PVDF-HFP separator after cycling. SEM images of (c, d) pristine lithium metal, (e, f) from the PP-cell, and (g, h) from the MOF@PVDF-HFP cell.....	91
Figure 7.13 Cyclic voltammograms profiles at different scan rates of Li-S cells: (a) PP and (b) MOF@PVDF-HFP separator. The linear fits of the peak currents for cells with (c) PP separator and (d) MOF@PVDF-HFP separator.....	93

Figure 7. 14 (a) The comparison of rate performance of Li-S cells assembled by different separators at various current densities. (b) Voltage profiles of Li-S cell assembled by a MOF@PVDF-HFP separator.....	94
Figure 7.15 (a) The cycling performance of Li-S cells with different separators. (b) Cycle stability of Li-S cell with MOF@PVDF-HFP membranes with different thickness.....	95
Figure 7.16 Ultralong-term cycling performance with selected voltage profiles of Li-S cell with a MOF@PVDF-HFP separator at 2 C. ....	96
Figure 7. 17 (a) Schematic of the inner structure and (b) digital photograph of a Li-S pouch cell with a MOF@PVDF-HFP separator. (c) Cyclic stability of the Li-S pouch cell at 0.1 C under various degrees bending state. ....	98
Figure 7. 18 PXRD patterns of MOF@PVDF-HFP membranes at different stages. ....	98
Figure 7. 19 FT-IR spectra of MOF@PVDF-HFP at different stages.....	99
Figure 7. 20 FE-SEM image with the corresponding elemental maps of Cu, F and S of MOF@PVDF-HFP membrane after cycling in Li-S coin cell. ....	100
Figure 7. 21 (a) Survey XPS and (b) Cu 2p XPS spectra of MOF@PVDF-HFP before and after cycling. (c) Cu 2p and (d) S 2p XPS spectra of MOF@PVDF-HFP membrane after cycling. In (c) and (d), (-●-) represents experimental XPS curve, where (-o-) represents the fitted XPS curve by using Gaussian-Lorentzian function after performing a Shirley background correction. ..	101

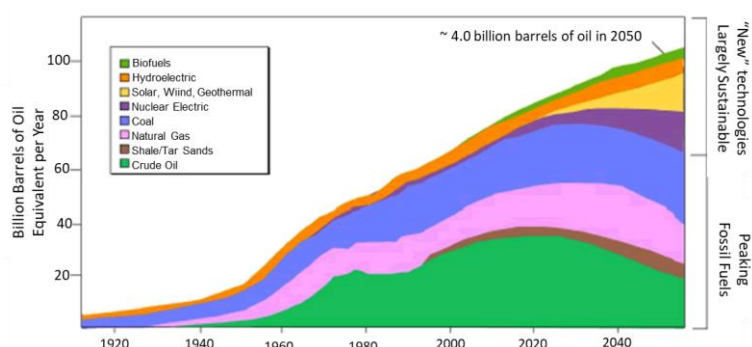
## LIST OF TABLES

Table 1.1 Basic requirements of separators for lithium-based batteries. ....	5
Table 7.1 Comparison of Li-S cell in this work with other Li-S batteries.....	97
Table 8.1 Summary of the properties of the three types of separators.....	104

# Chapter 1. General introduction

## 1.1 Historical development of lithium-sulfur batteries

With the rapid increase of energy demand, high-efficiency and eco-friendly energy storage technologies based on the renewable sources are urgently required to be developed and adopted (Figure 1.1). In the last few decades, rechargeable batteries, such as lead-acid (Pb-acid) batteries, alkaline (Zn-Mn) batteries, nickel metal-hydride (Ni-MH) batteries, and lithium-ion (Li-ion) batteries, have been proved feasible for electrical energy storage and applied in many fields. Among various kinds of rechargeable battery systems, Li-ion batteries have become prominent because of their higher energy density. Nevertheless, for the current Li-ion battery technology based on the insertion-compound cathode and anode materials, its energy density has almost reached the ceiling due to the limited capacities of insertion-oxide cathodes ( $\sim 250 \text{ mA h g}^{-1}$ ) and graphite anodes ( $\sim 370 \text{ mA h g}^{-1}$ ).<sup>1</sup> Therefore, alternative electrode materials that offer higher capacities need to be further developed. Meanwhile, some important parameters relating to energy density, cycle life, cost, safety, and environmental compatibility should take into consideration.



Sources: Lynn Orr, *Changing the World's Energy Systems*, Stanford University Global Climate & Energy Project.

Figure 1.1 World's energy demand increased rapidly. (Photo: energyandcapital.com)

Sulfur is one of the most abundant elements in earth's crust. Theoretically, it can offer a high capacity of  $1675 \text{ mA h g}^{-1}$ , which is quite higher than those of the transition-metal oxide cathode materials. More importantly, the environmental friendliness and low cost of sulfur also greatly meet the requirements of renewable and clean energy development. Lithium metal possesses low standard potential ( $-3.04 \text{ V vs. SHE}$ ), ultra-high theoretical capacity ( $3860 \text{ mA h g}^{-1}$ ), as well as light weight ( $0.53 \text{ g cm}^{-3}$ ), thus it is considered as an ideal anode material for rechargeable batteries. Thus, the exploitation of lithium-sulfur (Li-S) batteries based on sulfur cathode and lithium-metal anode is an inevitable trend.

The invention of Li-S batteries dates to 1962, when Herbert and Ulam patented a primary battery employing sulfur as cathodic material and lithium as anodic material.<sup>2</sup> Since then, some scientists and researches turn their attentions to development of Li-S batteries. Few years later, the voltage of the battery was obtained by introducing organic solvents, such as polycarbonate (PC), N,N-Dimethylformamide (DMF), dimethyl sulfoxide (DMSO) and so on.<sup>3</sup> However, research relative to sulfur-based batteries ceased in the 1990 with the success of Lithium-ion batteries (LIBs).<sup>4, 5</sup> After 2000, the rapid development of emerging applications came up with higher demands on the battery energy density, leading to the resurgent of Li-S batteries.<sup>5-7</sup> In the recent years, the number of scientific publications on the topic of Li-S batteries grows exponentially.

## 1.2 Configurations of lithium-sulfur batteries

Generally, a Li-S cell is composed of cathode, anode, separator, electrolyte and battery shell (Figure 1.2).

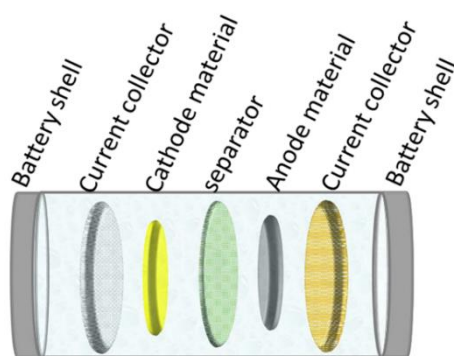


Figure 1.2 Schematic illustration of the inner structure of a Li-S battery.

### 1.2.1 Cathode

The cathode includes cathode materials and cathode current collector. In general, the crucial ingredient for electrode material is sulfur, but its poor electrical conductivity makes it not a good choice for direct use as cathode material of batteries. Therefore, in order to make the sulfur available for Li-S batteries, various approaches have been conducted to improve its electrical conductivity. The most commonly used strategies are directly mixing sulfur with some conductive additives (e.g. carbon materials) or employing some conductive materials to fabricate sulfur-composites materials. Current collector is a conductive solid part that connect to the electrode with external loading. Its main function for different types of batteries is similar: supporting the electrode and collecting the accumulated electrical energy from the electrode.<sup>8</sup> The good conductivity of current collector plays significant role in improving the electrochemical performance of batteries. Currently used collectors for cathode are mostly aluminium foils or carbon papers.

### 1.2.2 Anode

The anode of Li-S batteries is commonly fabricated by pressing a lithium metal foil on the current collector. The widely applied anode current collectors for Li-S batteries are copper foils or copper meshes. Recently, some lithium metal-free anodes (e.g. carbon,

silicon, alloy, and tin) have aroused considerable attentions owing to their high conductivity, low weight and high safety.<sup>9, 10</sup> It should be noted that when the cathode material is sulfur, the metal-free anodes should be pre-lithiated before they are used as lithium sources for assembling Li-S batteries.

### 1.2.3 Separator

Separator is placed between cathode and anode to separate the two electrodes. Besides, the separator can also act as electrolyte reservoir to enable the transportation of ions.<sup>10</sup> Although the separator does not take part in the cell reaction, its physical and chemical properties greatly influencing the electrochemical performance of Li-S batteries, including energy density, rate performance, cycle life as well as safety. In this case, some important factors should be taken into consideration while choosing appropriate separators for Li-S batteries<sup>11, 12</sup>: 1) Separators must be chemically and electrochemically stable to the electrode materials and electrolyte; 2) The separators should have good wettability for absorbing and retaining liquid electrolyte to realize low internal resistance and high ionic conductivity; 3) The separators should have good mechanical strength to withstand the penetration of electrode materials; 4) Available thickness and appropriate porosity greatly influence the ionic conductivity of separators; 5) Separators should be as flat as possible while laying out and immersing in liquid electrolyte to avert the misalignment when they are used to assemble Li-S batteries. Table 1.1 presents the basic requirements of separators not only for batteries.<sup>10</sup> The commercial separators for Li-S batteries are generally microporous polyethylene (PE) and laminates of polypropylene (PP) and polyethylene.

Table 1.1 Basic requirements of separators for lithium-based batteries.<sup>11</sup>

Parameter	Requirement
Chemical and electrochemical stabilities	Stable for a long period of time
Wettability	Wet out quickly and completely
Mechanical property	>1000 kg cm <sup>-1</sup> (98.06 MPa)
Thickness	20–25 μm
Pore size	<1 μm
Porosity	40–60%
Permeability (Gurley)	<0.025 s μm <sup>-1</sup>
Dimensional stability	No curl up and lay flat
Thermal stability	<5% shrinkage after 60 min at 90 °C
Shutdown	Effectively shut down the battery at elevated temperatures

#### 1.2.4 Electrolyte

Electrolyte is also an essential component to enable the normal operation of Li-S batteries. The main function of the electrolyte in a battery is to transport ions between the electrodes.<sup>13</sup> The available target of Li<sup>+</sup> ionic conductivity should be higher than 10<sup>-4</sup> S cm<sup>-1</sup> in the operation temperature range.<sup>3</sup> For practical cells, high chemical and electrochemical stabilities of electrolyte are also required. The most common electrolyte concept for Li-S battery is a simple lithium salt with a small to medium sized anion, which is dissolved in a matrix of one or two solvents based on small organic molecules, offering a concentration close to 1 M.<sup>14</sup> The typical lithium salts for preparing electrolyte are lithium trifluoromethanesulfonate (LiTf), lithium bis(trifluoromethanesulfonyl)imide (LiTFSI), Lithium hexafluorophosphate (LiPF<sub>6</sub>), and Lithium perchlorate (LiClO<sub>4</sub>) (Figure 1.3).<sup>13</sup> The organic solvents include ethers tetrahydrofuran (THF), 1,2-dimethoxyethane (DME), and 1,3-dioxolane (DOL), sulphones, carbonates, glymes, and so on (Figure 1.4).<sup>3</sup>

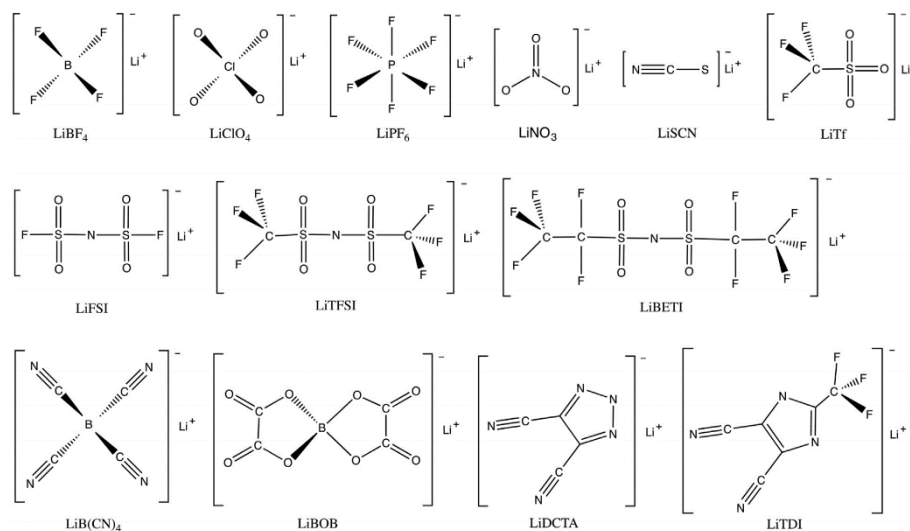


Figure 1.3 Lithium salts for preparing the electrolyte of Li-S batteries.<sup>13</sup>

Besides the non-aqueous organic liquid electrolytes, some special electrolyte systems such as ionic liquid-based electrolytes,<sup>15-17</sup> gel polymer electrolytes,<sup>18-20</sup> and solid electrolytes<sup>21-23</sup> also have been exploited and applied in Li-S batteries.

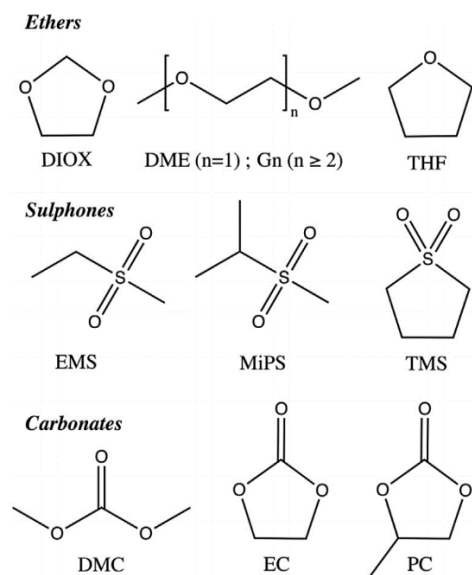


Figure 1.4 Organic solvents for preparing the electrolyte of Li-S batteries.<sup>3</sup>

### 1.3 Principles of lithium-sulfur batteries

The Li-S cell can store electrical energy in sulfur electrode. A schematic of the components in a Li-S cell and its typical discharge-charge voltage profile<sup>24</sup> in ether-based electrolytes are presented in Figure 1.5.

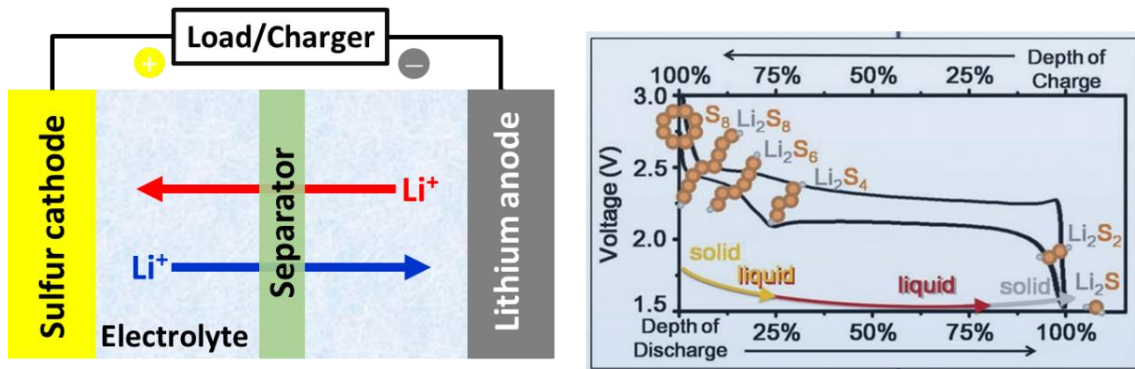
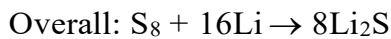
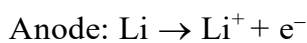


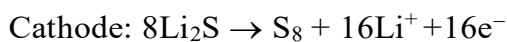
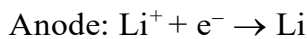
Figure 1.5 The schematic of operation mechanism in a single Li-S cell and its typical discharge-charge voltage profile<sup>24</sup> in ether-based electrolytes.

Li-S batteries operated based on a reversible electrochemical reaction of  $16\text{Li} + \text{S}_8 \leftrightarrow 8\text{Li}_2\text{S}$ .<sup>4, 6</sup> Specific reactions at cathode and anode are as follows:

Discharge:



Charge:



Although these reactions look simply, the actual charge/discharge process involves a series of complex electrochemical conversion. During the discharging

process, in the anode side, lithium metal is oxidized to form lithium ions ( $\text{Li}^+$ ) and electrons. In the cathode side, the sulfur is firstly reacted with transferred  $\text{Li}^+$  to reduce to long-chain lithium polysulfide species ( $\text{S}_8 \rightarrow \text{Li}_2\text{S}_8 \rightarrow \text{Li}_2\text{S}_6 \rightarrow \text{Li}_2\text{S}_4$ ) at an average voltage of  $\sim 2.35$  V (vs  $\text{Li}/\text{Li}^+$ ), which corresponds a fast-kinetic process because of the high solubility of long-chain lithium polysulfides. This process contributes around 25% of the theoretical capacity ( $418 \text{ mA h g}^{-1}$ ) of sulfur.<sup>25</sup> Then the generated long-chain lithium polysulfides are further reacted with  $\text{Li}^+$  ions to form insoluble short-chain lithium sulfide species ( $\text{Li}_2\text{S}_4 \rightarrow \text{Li}_2\text{S}_2 \rightarrow \text{Li}_2\text{S}$ ) at a relatively low platform at  $\sim 2.1$  V (vs  $\text{Li}/\text{Li}^+$ ), relating to a slow kinetic process. This process contributes the remaining 75% of the theoretical capacity ( $1257 \text{ mA h g}^{-1}$ ) of sulfur.<sup>26</sup> The reconversion of  $\text{Li}_2\text{S}$  to elemental sulfur occurs during the subsequent charging process through the formation of a series of lithium polysulfides intermediates.<sup>27</sup> Overall, the operation of Li-S batteries undergo a solid-liquid-solid transition, which is quite different from other energy storage battery systems. This is also part of the reasons causing poor electrochemical performance of practical Li-S batteries.

## Chapter 2. Technical challenges of lithium-sulfur batteries

### 2.1 Introduction

Although Li-S battery possess high energy density in theory, several challenges seriously limit its practical applications and need to be addressed for future commercialization.<sup>24</sup> In this section, the intrinsic and extrinsic problems of Li-S batteries (Figure 2.1) would be discussed.

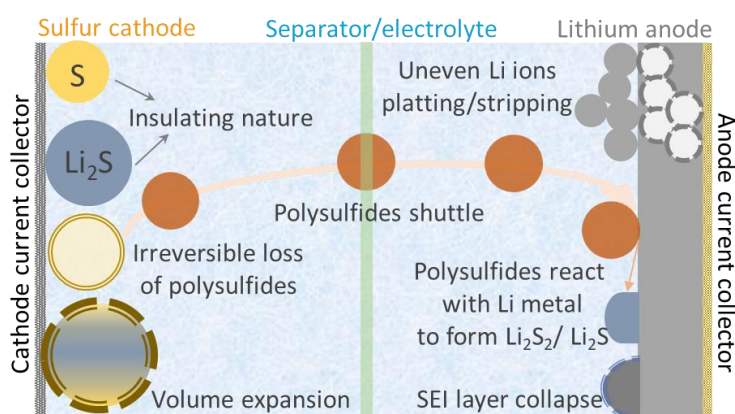


Figure 2.1 The intrinsic and extrinsic problems of Li-S batteries.

### 2.2 Insulating nature of sulfur

The combination of sulfur cathode and lithium anode can offer high specific capacity. However, both sulfur and its final-discharge product  $\text{Li}_2\text{S}$  are electrical insulation with very poor electronic conductivity around  $\sim 10^{-30} \text{ S cm}^{-2}$ , which seriously constrains the efficient electrochemical reactions. The sluggish electrochemical reaction kinetics results in incomplete conversion reactions.<sup>28</sup> Thus, even after repeated cycling, unreacted sulfur clusters still exist in the cathode, leading to low utilizations of the active materials.<sup>29</sup> The observation of the cycled cathode also indicates that the fast reaction kinetics at the upper discharge plateau

of ~2.35 V is not enough to realize full utilization of sulfur. In addition, at the relative lower discharge plateau of ~2.1 V, the high resistance gives rise to more difficult conversion of polysulfides to lithium sulphides due to the sluggish reaction kinetics of the liquid-solid process.<sup>30, 31</sup> What's worse, during the reiterated cycling process, the continuous precipitation of insulative discharge products  $\text{Li}_2\text{S}$  will create a passive layer on the surface of cathode, resulting in increased overpotential and limiting an ideal capacity output.<sup>32</sup> In this case, in order to obtain high utilization of sulfur, introducing conductive additives in the cathode is always required. A uniform dispersion of sulfur in the conductive host or on the conductive substrate is necessary for good electrical contact, which is beneficial to achieve a smooth conversion of sulfur.<sup>29, 30, 33</sup>

## 2.3 Shuttle of soluble polysulfides

During the discharging/charging process, the generated lithium polysulfides are highly soluble in the most organic electrolytes of Li-S batteries. The dissolved polysulfides in the liquid organic electrolyte have high electrochemical activity and good mobility. The relocation of soluble polysulfide anions within region of cathode facilitates a uniform distribution of active materials. Additionally, the dissolved polysulfides can act as redox mediators to assist the redox reactions in the cell.<sup>28, 34, 35</sup> These positive features of soluble lithium polysulfides are conducive to make the active materials to access for the Li ions from electrolyte and electrons from conductive hosts/substrates, enhancing the utilization of active materials and improving the rate performance.<sup>36-38</sup>

However, due to the high mobility and the concentration difference between cathode region and anode region, the dissolved polysulfides can easily diffuse from cathode side to anode side (Figure 2.2).<sup>39</sup> The migrating polysulfide anions can

chemically react with lithium metal anode to form insoluble lithium sulfides ( $\text{Li}_2\text{S}_2/\text{Li}_2\text{S}$ ). Upon charging, the remaining unreacted polysulfides are partially reduced by lithium ions to form relatively shorter chain polysulfides, which can diffuse back to cathode region resulted from the electric field from anode to cathode.<sup>32, 40-42</sup> The repeated migration of polysulfide ions between cathode and anode causes the so-called “shuttle effect”, which gives rise to a serious of adverse problems and seriously affects the electrochemical performance of Li-S batteries,<sup>43-45</sup> including: (1) the chemical reaction between polysulfides and lithium metal leads to irreversible loss of active materials and rapid decay of capacity; (2) the generated insulating lithium sulfides on the surface of lithium anode will form a passivate layer, causing a high resistance and severe polarization of the cell; (3) upon the repeated cycling, the continuous dissolution, relocation and redeposition of the active material species cause irreversible rearrangement distribution of sulfur within the cathode, which passivates the cathode and increase the cell impedance due to the uneven distribution of insulating sulfur.<sup>24, 32, 38</sup> As a result, the dissolution of polysulfides leads to a serious of unfavourable effects, including rapid capacity decay, poor Coulombic efficiency, poor rate performance and short cycle life.

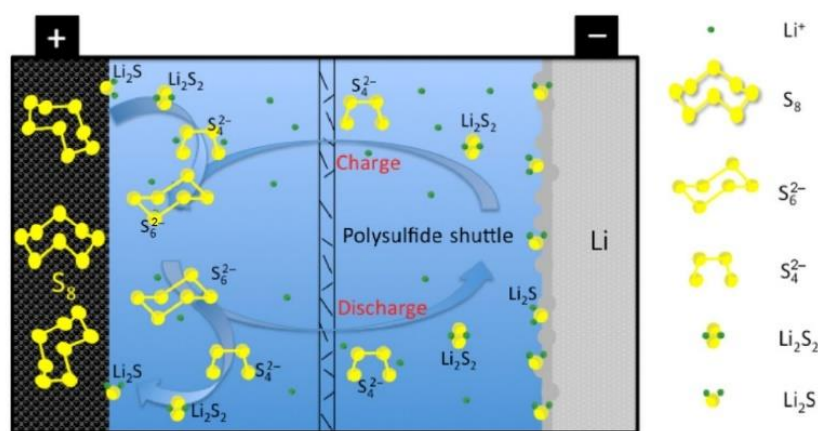


Figure 2.2 Schematic illustration of shuttle of dissolved polysulfide ions.<sup>39</sup>

## 2.4 Volume expansion of sulfur cathode

The density of sulfur is  $2.07 \text{ g cm}^{-3}$ , while the density of  $\text{Li}_2\text{S}$  is  $1.66 \text{ g cm}^{-3}$ . The big difference between them lead to a large volume expansion of active materials up to 80% upon lithiation.<sup>24</sup> The repeated volume change of the electrode easily causes collapse of the cathode structure and pulverization of the cathode.<sup>4, 46, 47</sup> Besides, the cathode with damaged integrity results in detachment of sulfur from the cathode host or conductive agents.<sup>37, 38</sup> Without a good electrical contact with conductive matrix, the insulating sulfur will lose access to electrons, becoming inactive.<sup>48, 49</sup> The isolate sulfur is difficult to take part in the following electrochemical reactions, resulting in increased cell impedance and rapid capacity fade.<sup>50, 51</sup>

In this regard, providing appropriate void spaces within the cathode is necessary, because it is beneficial for accommodating the big volume change of the active materials and preserving cathode integration.<sup>46</sup> However, combining the intrinsic low density of sulfur with a big volume host would further decrease the volumetric energy density of the battery.<sup>52-54</sup> Therefore, an appropriate porosity of cathode is quite important for achieving high volumetric energy density of Li-S batteries.<sup>38, 52, 55</sup>

## 2.5 Degradation of the lithium-metal anode

Apart from the improvement of sulfur cathode for Li-S batteries, some serious issues associated with lithium metal anode also need to be addressed.<sup>8, 9, 56</sup> The lithium metal has good activity, which allows it easily to react with the organic solvents of electrolytes to generate a solid electrolyte interphase (SEI) layer on the surface of lithium anode.<sup>24, 32</sup> The formed SEI layer can prevent the further reaction

between organic electrolyte and the active lithium metal, offering a relatively good chemical and electrochemical stability of the battery.

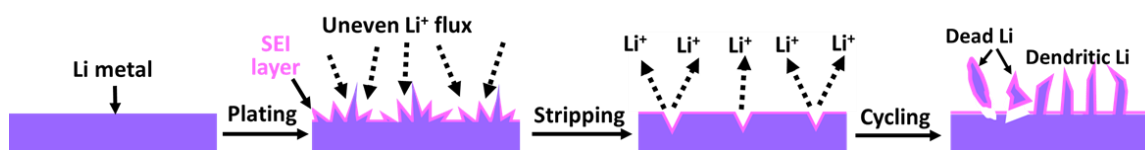


Figure 2.3 Schematic illustrates the formation of lithium dendrites.

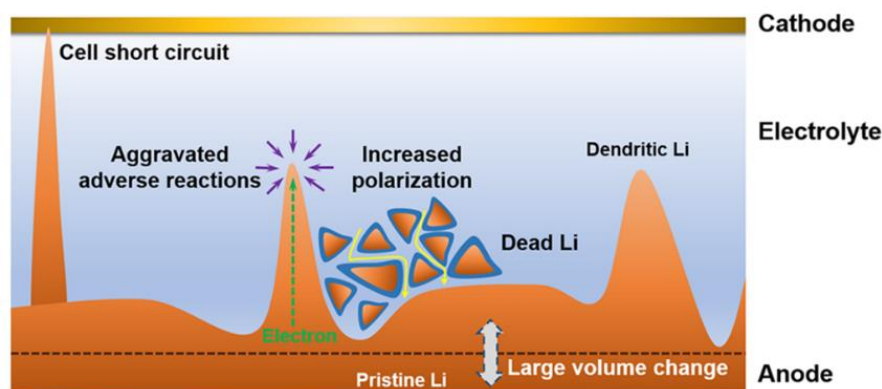


Figure 2.4 Schematic illustrates the problems caused by the lithium dendrites.<sup>57</sup>

However, the uncontrol growth of lithium dendrites seriously destabilize the anode circumstances within the cell. The formation of the lithium dendrites is originally caused by the change of lithium crystal morphologies during the continuous charging/discharging process (Figure 2.3). At a low charge/discharge current density, the concentration gradient of electric field and the preferred transfer of Li ions to rough surface regions of the electrode leads to the instable lithium crystal morphologies, which are known as “lithium dendrites”. In the case of high charge/discharge current density, because of the consumption of anions near the anode, a space charge is produced in the electrolyte. It drives ions away from regions circumambient a growing dendrite and masses them on the dendrite tip, accelerating the growth of dendrites. Therefore, no matter charging/discharging at low rate or high rate, the rough and dendritic deposition of lithium

metal would be produced. The growth of lithium dendrites brings several fatal obstacles for Li-S batteries (Figure 2.4)<sup>57</sup>: (1) the spiculate lithium dendrites can damage the formed SEI layer via the reaction between lithium metal and electrolyte, giving rise to unstable electrochemical environment in the cell; (2) the growth of lithium dendrites would greatly increase the active surface area of the lithium metal and accelerates the side reaction between electrolyte and lithium metal, resulting in irreversible loss of active lithium metal and rapid consumption of electrolyte; (3) due to the electrical insulation of side reaction products between electrolyte and lithium metal, the wrapped lithium metal loss the approachability to the current collectors and become electrically isolated, directly causing a lot of “dead lithium”; (4) the porous and uneven solid state interface (SEI) layer will increase the diffusion distance and resistance of Li ions and electrons, leading to a high polarization; (5) when the sharp dendrites penetrate the separator, it would cause the directly electrical contact between cathode and anode, resulting internal short and explosion ensue.<sup>19-22</sup> In short, the growth of lithium dendrites not only significantly reduces the energy density and Coulombic efficiency of Li-S batteries, but also induces the serious safety issue. Therefore, efficient strategies need to be developed stabilize the lithium metal anode, achieving high-performance of Li-S batteries.

# Chapter 3. Effective strategies to address the issues in lithium-sulfur batteries

## 3.1 Introduction

Recently, many efforts have been devoted and various strategies have been dedicated to address the above issues. Based on the reported research papers, the effective strategies can be categorized into three types: (1) designing porous structure of cathode materials; (2) constructing a protective layer on the surface of lithium metal anode; (3) introducing functional interlayer/separator between cathode and anode. Herein, we present an overview of the state-of-the-art strategies for high-performance Li-S batteries. This Chapter will be summed up into three parts: stabilizing sulfur cathodes, protecting lithium-metal anodes, and modifying separators.

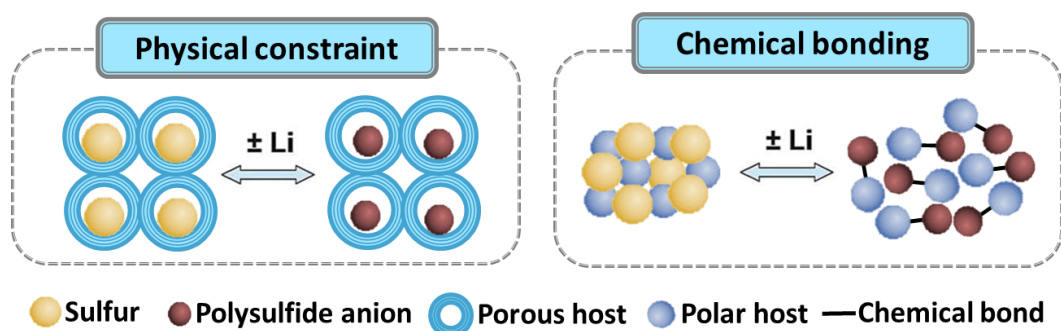


Figure 3.1 Schematic illustrations of confining polysulfides in cathode via physical constraint or chemical bonding.

## 3.2 Stabilizing sulfur cathodes

Fabricating stable sulfur cathodes is one of the most widely approaches to improve the performance of Li-S batteries. A suitable sulfur cathode not only can

accommodate the volume variation during the charging and discharging process, but also can entrap the soluble intermediate polysulfides via physical constraint/chemical bonding (Figure 3.1). Many efforts have been devoted to construct stable sulfur cathodes. The most popular pathway is to introduce porous materials and/or polar materials as sulfur hosts.

### 3.2.1 Porous carbon-based cathodes

Among various porous materials, conductive porous carbon-based materials are regarded as excellent hosts for the sulfur in Li-S batteries due to their superior electrical conductivity. The porous structure not only can guarantee a good electrical contact between sulfur and hosts, but also is able to stand the volume change during the cycling because of the density difference between  $\text{Li}_2\text{S}_2/\text{Li}_2\text{S}$  and sulfur. More importantly, the porous structure also can provide a physical constraint for the soluble polysulfide intermediates. Nazar et al. employed highly ordered CMK-3 as sulfur hosts (Figure 3.2a) for Li-S batteries.<sup>58</sup> The nanostructured CMK-3/S composites shows an impressive discharge capacity of  $1005 \text{ mA h g}^{-1}$  (Figure 3.2b), which is quite higher than that of the conventional carbon/S electrode (on average between 300 and  $420 \text{ mA h g}^{-1}$ ).<sup>58</sup> Lou group fabricated a carbon/sulfur composite by confining the sulfur within a double-shelled carbon sphere (Figure 3.2c).<sup>59</sup> The complex shell structure of the hollow carbon spheres can not only effectively mitigate the shuttle effect by encapsulating the polysulfides within the cavities, but also withstand the volume change upon the long-term cycling of Li-S batteries, delivering a high reversible capacity ( $690 \text{ mA h g}^{-1}$ ) after 100 cycles at a current density of  $0.1 \text{ C}$ .<sup>59</sup> Chen group developed an in-situ wrapping strategy to build a compact layer on carbon/sulfur composite particles (Figure 3.2d, e).<sup>60</sup> A sulfurized polyacrylonitrile (PANS) layer was grown on

CMK-3/S by free radical polymerization of acrylonitrile, and a triphenylphosphine sulfide (TPS) was formed on the top of PANS via introducing triphenylphosphine in the 1 M LITFSI within DOL/DME electrolyte (1:1, v/v). The special construction of cathode allows the polysulfides diffusion with the interior of the wrapped region of the composites to achieve a high utilization of the active materials but prevents the polysulfides migration to outside of the composites for inhibiting the shuttle effect. As a result, the CMK-3/S@PANS@TPS cathode significantly improves the Coulombic efficiency (98.2%) and cycle life of the Li-S batteries, achieving a high capacity retention ration of 89% at 0.25 C upon 100 cycles (Figure 3.2f).<sup>60</sup>

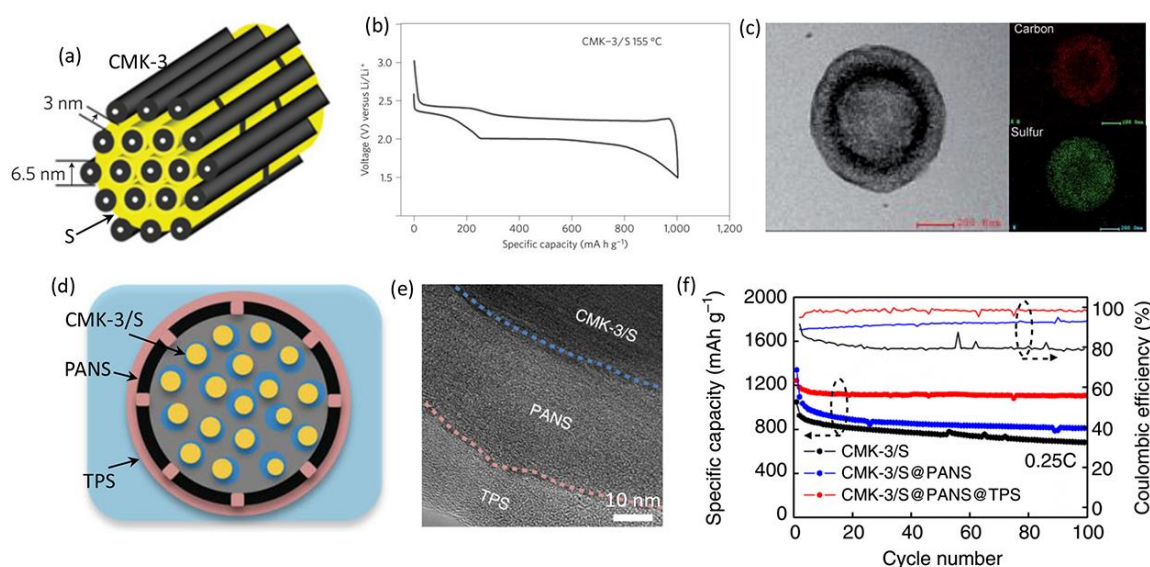


Figure 3.2 (a) A schematic diagram of the sulfur (yellow) confined in CMK-3, (b) charge/discharge profiles of CMK-3/S electrode.<sup>58</sup> (c) TEM image and corresponding elemental maps of a DHCS-S sphere.<sup>59</sup> (d) A schematic diagram and corresponding TEM image of CMK-3/S@PANS@TPS particle, (e) cycling performance of various electrodes at 0.25 C.<sup>60</sup>

### 3.2.2 Metal oxides/sulfides-based cathodes

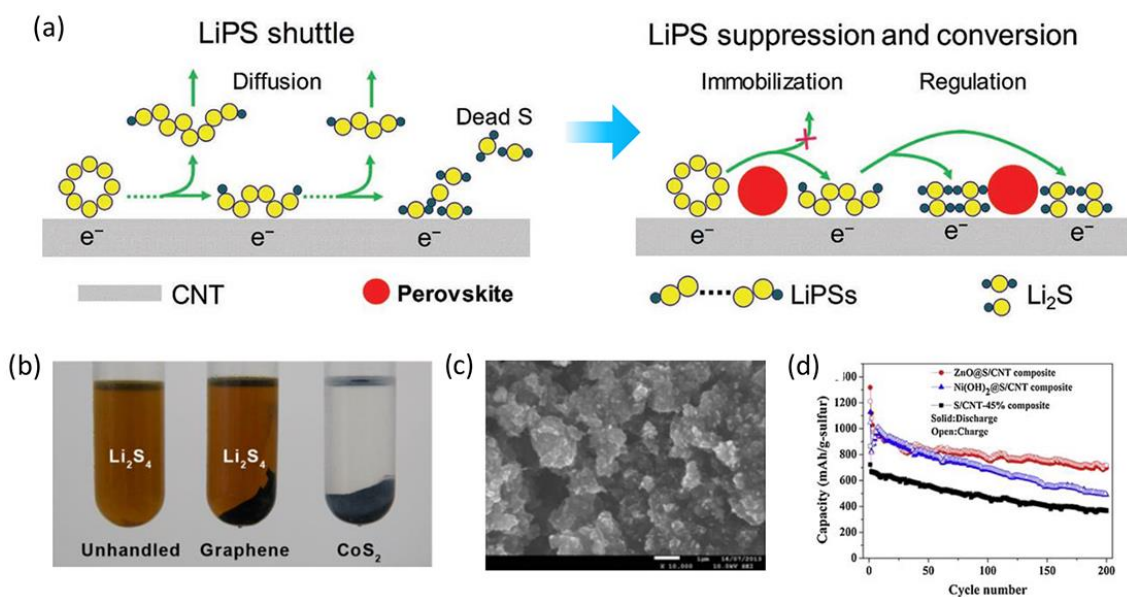


Figure 3.3 (a) LiPSs diffuse out of cathode and are immobilized on perovskite (PrNP) promoter, facilitating their redox reaction.<sup>61</sup> (b) Visualized adsorption of Li<sub>2</sub>S<sub>4</sub> on graphene and CoS<sub>2</sub>.<sup>62</sup> (c) SEM image of ZnO@S/CNT.<sup>63</sup> (d) Cycling performance of various cathodes at 1600 mA g<sup>-1</sup>.<sup>63</sup>

As the metal oxides/sulfides can facilitate the chemisorption of generated lithium polysulfides, a lot of metal oxides/sulfides were employed as sulfur hosts to prepare the cathode materials for Li-S batteries. In general, the metal oxides/sulfides possess many active sites, which can combine the lithium polysulfides via chemical bonding, hence affording high capacity and good cycle stability. Zhang and Huang *et al.*<sup>61</sup> reported the use of Ba<sub>0.5</sub>Sr<sub>0.5</sub>Co<sub>0.8</sub>Fe<sub>0.2</sub>O<sub>3-δ</sub> perovskite nanoparticles (PrNPs) as a promoter to anchor the polysulfides and guide the deposition of lithium sulfides (Figure 3.3a). On one hand, the abundant exposed active sites (O and Sr sites) on PrNPs facilitated the surface interactions between the lithium polysulfides and PrNPs to immobilize polysulfides. On the other hand, the variable- and high-valence transition metal ions (Fe and Co ions) introduced by PrNPs benefited for the uniform deposition of lithium sulfides.<sup>61</sup>

They also incorporated sulfiphilic cobalt disulfide ( $\text{CoS}_2$ ) into the carbon/sulfur cathode materials. The strong interaction between the active sites on the  $\text{CoS}_2$  and lithium polysulfides (Figure 3.3b) effectively mitigated the shuttle effect and facilitated the redox reactions of polysulfides.<sup>62</sup> With a 15% concentration of  $\text{CoS}_2$  in the  $\text{CoS}_2/\text{S}/\text{graphene}$  composite, a low capacity decay rate of 0.034% was achieved after 200 cycles at 0.2 C. Gu *et al.*<sup>63</sup> used a simple and low cost ball-milling method fabricated nickel hydroxide wrapped sulphur/carbon nanotubes ( $\text{Ni}(\text{OH})_2@\text{S}/\text{CNT}$ ) composites (Figure 3.3c) and zinc oxide wrapped sulphur/carbon nanotubes ( $\text{ZnO}@\text{S}/\text{CNT}$ ) composites as cathode materials for Li-S batteries. By introducing the  $\text{Ni}(\text{OH})_2$  and  $\text{ZnO}$  on the surface of  $\text{S}/\text{CNT}$  composites, the cyclic stability of the Li-S batteries were significantly enhanced (Figure 3.3d). After 200 cycles at 1 C, the  $\text{Ni}(\text{OH})_2@\text{S}/\text{CNT}$ -based and the  $\text{ZnO}@\text{S}/\text{CNT}$ -based Li-S cells can still deliver high discharge capacities of 490 and 698  $\text{mA h g}^{-1}$ , respectively.<sup>63</sup>

### 3.2.3 Polymer-based cathodes

In general, polymer is used as the binder for electrode materials in battery system, such as polyvinylidene Fluoride (PVDF) and polytetrafluoroethylene (PTFE). Recently, some polymers and their derivatives also have been increasingly sought out as sulfur hosts for their application in the development of Li-S batteries, because their unique chain structures and functional groups aid in restraining the shuttle effect through physical absorption and/or chemical bonding. Additionally, the good flexibility of polymers is beneficial for improving the mechanical strength and alleviating the volume expansion of the cathode. Kim *et al.*<sup>64</sup> reported a layer by layer polymer deposition strategy to develop stable cathode for Li-S batteries. They deposited a single

poly(allylamine hydrochloride) /poly(acrylic acid) (PAH/PAA) priming bi-layer with overcoated bi-layers of (polyethylene oxide/poly(acrylic acid))<sub>n</sub> (PEO/PAA)<sub>n</sub> on sulfur cathode materials (Figure 3.4a). The PAH/PAA layer was formed via the spin coating a mixed aqueous solution containing PAA (pH 3.5) and PAH (pH 7.5). Sequentially, the (PEO/PAA)<sub>n</sub> multilayers were introduced on the sulfur cathode via dipping deposition from PEO/PAA solution. Each solution was prepared by adding 0.1 M lithium bis(tri-fluoromethanesulfonyl)imide (LiTFSI), and the pH of the solution should be adjusted to allow for the hydrogen bonding between the proton rich carboxylic acids of PAA and the ether oxygen of PEO.<sup>64</sup> The research results indicated that the presence of a PAH/PAA bilayer on the sulfur cathode can act as a priming layer to aid in the further deposition of PEO/PAA layer. The PAH/PAA/(PEO/PAA)<sub>3</sub> coated layer can minimize the polysulfides diffusion rate while allowing the diffusion of lithium ions. Chung *et al.*<sup>65</sup> fabricated processable polymeric materials by directly copolymerization the vinylic monomers with elemental sulfur (Figure 3.4b). The tunable thermomechanical properties enables a high content of sulfur in the copolymer. The sulfur-modified copolymer cathodes exhibited a high specific capacity of 823 mA h g<sup>-1</sup> after 100 cycles at 0.1 C (Figure 3.4d).<sup>65</sup> Meanwhile, a class of organosulfur compounds(Figure 3.4c) were also fabricated by employing the porous trithiocyanuric acid (TTCA) crystals as precursors.<sup>66</sup> Applied the sulfur-rich polymers as cathode materials in Li-S batteries, The cells showed a high reversible capacity of 945 mA h g<sup>-1</sup> at 0.2 C after 100 cycles, achieving a high capacity retention of 92% (Figure 3.4e).<sup>66</sup>

In a word, confining sulfur within cathode is an effective approach to improve the electrochemical performance of Li-S batteries. However, despite some issues of Li-S batteries can be addressed by employing porous and/or polar materials to design unique

structure of sulfur cathode in the case of low sulfur loading, new challenges will be brought. On the one hand, the more serious volume expansion at high sulfur loading accelerate fatigue failure of the cathode structure. On the other hand, the electrical insulating property of most polar materials needs high content of conductivity additives to enhance the electrical conductivity of the cathode, thus resulting in a low sulfur ratio in the cell, which would inevitably sacrifice the overall energy density.

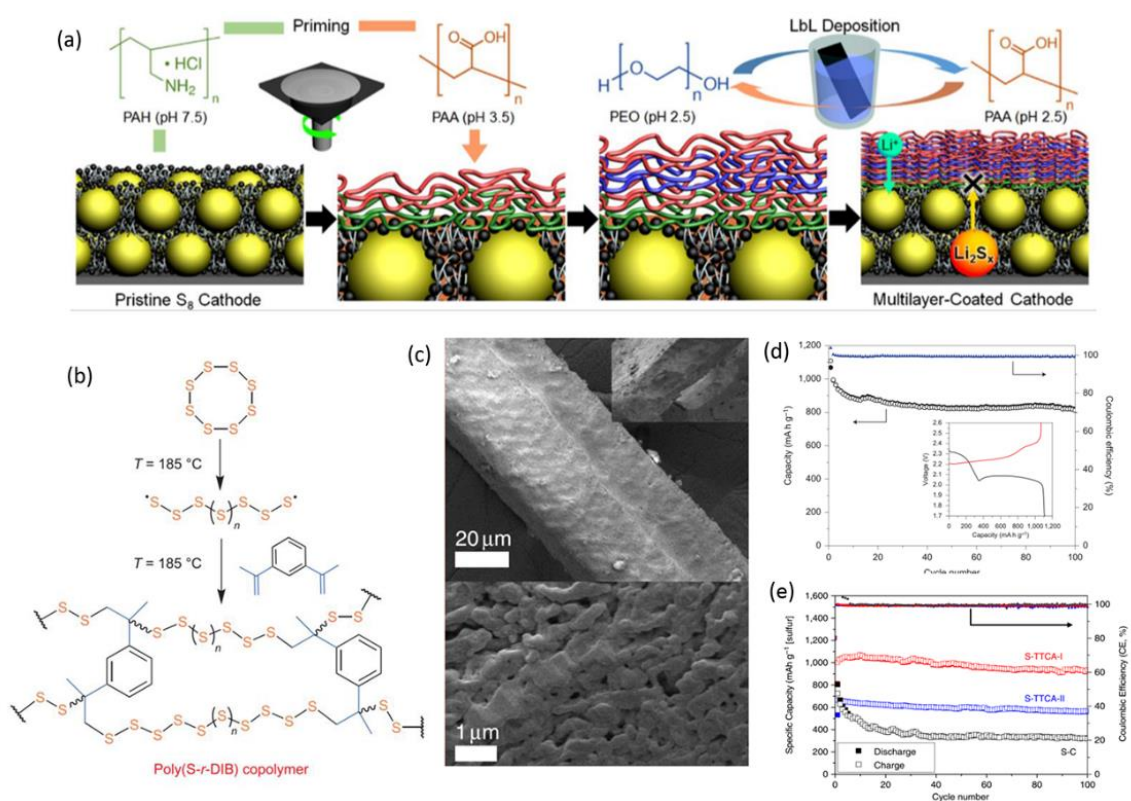


Figure 3.4 (a) Schematic illustrates fabrication of PAH/PAA/(PEO/PAA) by the layer-by-layer (LbL) deposition.<sup>64</sup> (b) Synthetic scheme of S<sub>8</sub> with DIB to form sulfur copolymers.<sup>65</sup> (c) SEM images of the S-TTCA-I.<sup>66</sup> (d) Cycling performance with a charge/discharge profile inset.<sup>65</sup> (e) The cycling performance and Coulombic efficiencies of Li-S cells with different cathodes.<sup>66</sup>

### 3.3 Protecting lithium-metal anodes

Apart from the cathode issue, the deactivation of metallic lithium anodes is also a serious problem leading to premature failure of the Li-S battery. In order to improve the cycling performance of Li-S batteries, approaches aiming to reinforce solid electrolyte interface (SEI) layers on the lithium metal anodes were extensively adopted, including adding additives into electrolytes, adjusting the components of electrolytes, introducing artificial layer on the surface of lithium anodes. Herein, the strategies are categorized into two parts: (1) including introducing additives into electrolytes and adjusting the components of electrolytes are identified as the *in-situ protection*; (2) introducing artificial layer on the surface of lithium anodes is regarded as the *ex-situ protection*.

#### 3.3.1 In-situ protection

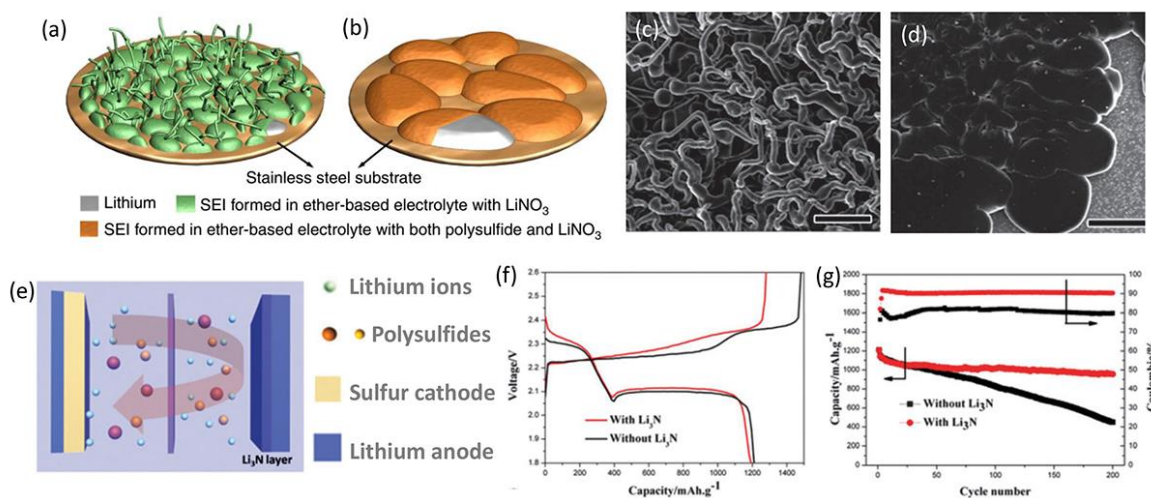


Figure 3.5 Schematic of the morphologies of lithium deposited on the substrate (a) without lithium polysulfide and (b) with lithium polysulfide. SEM images of cycled lithium metal electrodes (c) without and (d) with the addition of  $\text{Li}_2\text{S}_8$  (0.18 M). Scale bars, 20  $\mu\text{m}$ .<sup>67</sup> (e) Schematic of the cell with the  $\text{Li}_3\text{N}$  layer, (f) the charge-discharge profiles and (g) cycling performance of Li-S batteries with different lithium anodes at 0.2 C.<sup>68</sup>

In liquid electrolytes, a lot of organic and inorganic compounds have been introduced as additives to promote the formation of stable SEI layer during the initial cycles that activating lithium metal anodes. Electrolyte additives are generally deemed sacrificial. An ideal additive for electrolyte should react with lithium to some degree to form a chemically and physically stable SEI layer but should avoid too reactive to consume too much lithium. The formed SEI layer are beneficial for preventing the further side reaction between electrolyte and lithium metal anodes in the subsequent cycling process, inhibiting the decomposition of electrolytes and irreversible consumption of active lithium metal.<sup>57, 69</sup> The first-principles calculations and microgravimetric measurements also theoretically and experimentally demonstrated that an available SEI layer can aid in obtaining highly efficient lithium metal anodes,<sup>70</sup> which is quite essential to achieve high energy density of lithium metal-based batteries. *Cui et al.*<sup>67</sup> reported that the manipulating chemical reactions between lithium, lithium nitrate ( $\text{LiNO}_3$ ) and lithium polysulfide ( $\text{Li}_2\text{S}_8$ ) can effectively inhibit the growth of lithium dendrites. Both  $\text{Li}_2\text{S}_8$  and  $\text{LiNO}_3$  served as additives to be introduced in ether-based electrolyte, which capacitates a synergetic effect to form a uniform and stable SEI layer on the surface of lithium metal anodes (Figure 3.5a, b).<sup>67</sup> The formed SEI layer greatly reduce the decomposition of electrolyte and can greatly minimize the electrolyte. Additionally, they observed that the formation of lithium dendrites can be effectively suppressed at a practical current density of  $2 \text{ mA cm}^{-2}$  up to a deposited areal capacity of  $6 \text{ mA h cm}^{-2}$  (Figure 3.5c, d).<sup>67</sup> *Ma et al.*<sup>68</sup> in-situ constructed a  $\text{Li}_3\text{N}$  protective layer on the lithium anode surface via directly making the lithium metal react with nitrogen ( $\text{N}_2$ ) gas at the at room temperature. The polycrystalline  $\text{Li}_3\text{N}$  layer showed a high ionic conductivity that enable the fast migration of  $\text{Li}^+$ . Besides, the  $\text{Li}_3\text{N}$  layer can simultaneously inhibit the growth of lithium dendrites and prevent side reaction between polysulfides-contained electrolyte and lithium metal

anode (Figure 3.5e). As a result, lower polarization (Figure 3.5f) and a higher reversible capacity ( $956 \text{ m A h g}^{-1}$ ) after 200 cycles at 0.2 C (Figure 3.5g) was obtained after employing a  $\text{Li}_3\text{N}$  protected lithium metal as anode for Li-S batteries.<sup>68</sup> Besides adding additives into electrolyte, Archer's group demonstrated the application of hybrid electrolytes, such as ionic liquid-based hybrid electrolytes, as well as liquid electrolytes with halogenated salt solid blends, can effectively inhibit the growth of lithium dendrites and realize stable lithium metal anodes in carbonate electrolyte.<sup>71-73</sup>

### 3.3.2 Ex-situ protection

Except for adding the additives in electrolytes to in-situ generate the stable SEI layers, beforehand introducing an artificial SEI layer on the surface of lithium anodes were also widely applied to promote a stable lithium plating/stripping process, mechanically suppressing the growth of lithium dendrites. Zheng *et al.*<sup>74</sup> introduced a monolayer composed of interconnected amorphous hollow carbon spheres on the surface of lithium metal anode to facilitate the formation of a stable SEI layer (Figure 3.6a, b). The chemically stable carbon layer on the surface of lithium metal has a Young's modulus ( $\sim 200 \text{ Gpa}$ ), which is strong enough to inhibit the growth of lithium dendrites. Moreover, the weakly bound between the carbon layer and the current collector of lithium metal can move up and down to adjust available space to accommodate the volume change of lithium metal anodes during cycling.<sup>74</sup> Kozen *et al.*<sup>75</sup> developed a new strategy to stabilize the lithium metal anode via directly introducing atomic layer deposition (ALD) protection layers on the surface of lithium metal, creating a new phase between various corrosive surroundings and the metal anodes. As shown in Figure 3.6c, the pristine lithium foil almost immediately begins tarnishing after air exposure less than 1 min, while the ALD  $\text{Al}_2\text{O}_3$  protected lithium foil greatly delayed the onset of surface tarnishing up to 20 h.<sup>75</sup> Furthermore, the Li-S battery with a protected lithium

anode maintained about 90% of its initial capacity after 100 cycles at 0.1 C (Figure 3.6d), and the Li-S with a bare lithium metal anode can only kept 50% of its initial capacity, indicating that the introduction of a ALD  $\text{Al}_2\text{O}_3$  layer on lithium metal anode can effectively improve the electrochemical performance of Li-S batteries.<sup>75</sup>

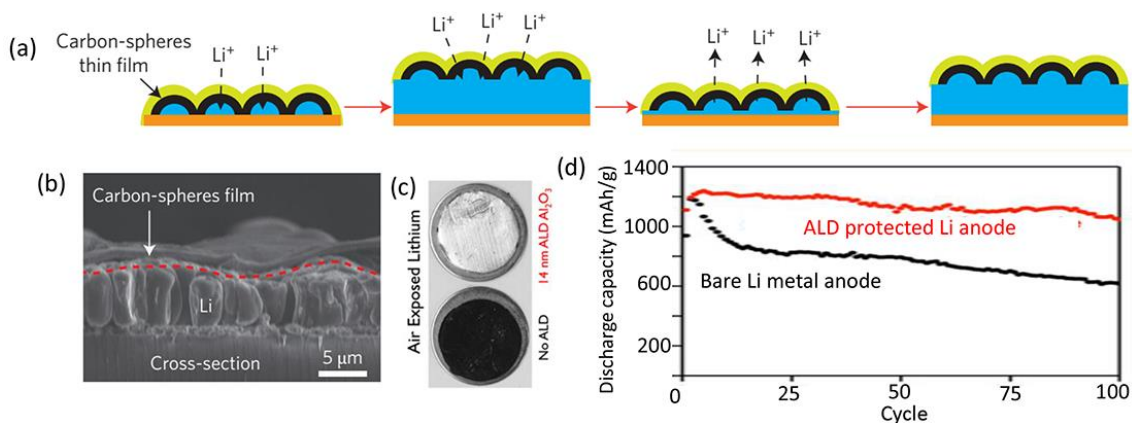


Figure 3.6 (a) Schematic diagrams of stabilizing the lithium metal by a hollow carbon nanosphere layer, (b) cross-section SEM image of the carbon spheres coated lithium metal.<sup>74</sup> (c) Optical images of lithium foil surface exposed in atmosphere, (d) cycling performance of Li-S cells with different lithium anodes.<sup>75</sup>

It should be noted that although introducing an addition layer on the surface of lithium metal can simultaneously suppress the reaction between polysulfides and lithium metal and prevent the growth of lithium dendrites, it generally increases the interfacial resistance between lithium anode and electrolyte.

### 3.4 Modifying separators

Owing to without adverse influence on the cathode and anode, functional separators have been attracted considerable attentions recent years. Modifying the common separators by functional materials has been demonstrated that can effectively inhibit the shuttle effect via physical obstruction and/or chemical bonding.<sup>76-79</sup> In this case, separator modification seems to be more reliable to

obtain high-performance Li-S batteries for practical applications. The materials used for modifying separators are basically the same with the materials for stabilizing cathode, including carbon-based materials, inorganic metal oxides/sulfides-based materials, and polymer-based materials. Some novel materials such as black phosphorus and metal-organic framework (MOF) were also exploited and applied for constructing functional separators.

### 3.4.1 Carbon-based separators

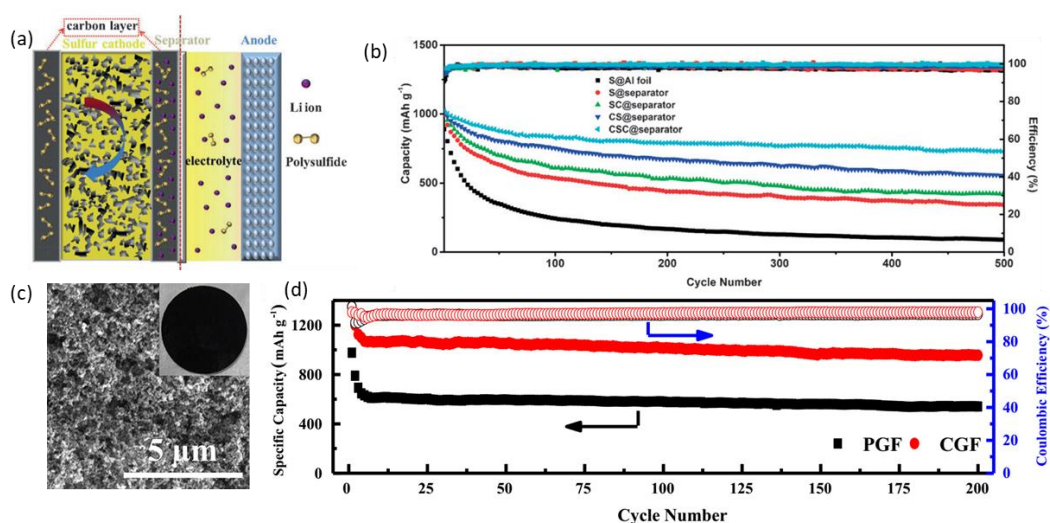


Figure 3.7 (a) Schematic illustration of Li-S cell with a carbon-based separator, (b) long-term cycling performance of various separators at 0.6 C.<sup>80</sup> (c) SEM image of carbon-coated Glass Fiber with its photograph inset, (d) Cycling performance of Li-S cells with PGF and CGF at a current density of 0.2 C.<sup>81</sup>

Owing to the extraordinary electrical conductivity, large surface area, good thermostability and chemical stability, carbon-based materials become one of the most popular choice to modify the separators for Li-S batteries. The widely applied materials include carbon particles,<sup>78-80</sup> carbon nanofibers/nanotubes,<sup>84-89</sup> graphene or graphene oxide sheets,<sup>90-94</sup> and various porous carbon-based materials.<sup>81, 83, 95-97</sup> A typical

scheme of carbon-modification separator for impeding the shuttle of polysulfides is shown in Figure 3.7a.<sup>80</sup> Introducing a carbon interlayer between the cathode and traditional separator can not only block the diffusion of polysulfide anions by physical obstruction, but also can serve as an additional current collector to facilitate the electrons transport into active material. Such a design is beneficial for enhancing the utilization of active materials and improving the cycle stability of Li-S batteries. As a result, the Li-S batteries with a carbon coated separator achieved a discharge capacity of 730 mA h g<sup>-1</sup> at 0.6 C after 500 cycles with a small capacity decay rate of 0.058% per cycle (Figure 3.7b).<sup>80</sup> Zhu *et al.*<sup>81</sup> coated a conductive carbon (Super P) particle layer onto one side of the ordinary Glass Fiber (GF) membrane (Figure 3.7c) by a doctor blade casting method. When the separator applied in the Li-S battery (the carbon layer toward the sulfur cathode), outstanding cyclic stability with a high reversible capacity of 956 mA h g<sup>-1</sup> after 200 cycles at 0.2 C (Figure 3.7d).<sup>81</sup>

### 3.4.2 Inorganic metal oxides/sulfides-based separators

Because the metal oxides/sulfides can immobilize polysulfides by the chemical interaction between the polysulfides and the heteroatom dopants (such as B, N, O, and S, etc.) or the exposed metal sites on the polar materials, inorganic metal oxides/sulfides and their composites are employed as modifiers to fabricate the functional separators for Li-S batteries. Vanadium oxide (V<sub>2</sub>O<sub>5</sub>) with good solid-state Li<sup>+</sup> conductivity, is a popular cathode material for lithium-ion battery. A micrometer-scale V<sub>2</sub>O<sub>5</sub> layer coated on the commercial separators can effectively mitigate the polysulfides diffusion without negatively influence on the transportation of Li<sup>+</sup>.<sup>98</sup> Besides of blocking the shuttle effect, multi-component-based separators are also beneficial for further address the corrosion problem of Li anodes. Al<sub>2</sub>O<sub>3</sub> are generally employed as a functional coating on the separator to improve the electrochemical performance of lithium-ion batteries. The good

thermal stability of  $\text{Al}_2\text{O}_3$  is in favour of controlling the thermal shrinkage of separator. Moreover, the intrinsic hydrophilicity of  $\text{Al}_2\text{O}_3$  can greatly improve the liquid electrolyte wetting behaviour of the separator.<sup>99, 100</sup> Owing to these advantages,  $\text{Al}_2\text{O}_3$  recently are used for Li-S batteries in two ways, one is as sulfur hosts in cathode,<sup>101, 102</sup> another is as a function layer on the routine separator. When the  $\text{Al}_2\text{O}_3$  layer faced to cathode, it can block the migration of polysulfides via chemical adsorbing and physical obstacle.<sup>100, 103, 104</sup> Tang *et al.*<sup>82</sup> introduced a  $\text{MoS}_2$  layer on the surface of commercial Celgard membrane (Figure 3.8b). The  $\text{MoS}_2$ /Celgard separator acted as an ion sieve that allowed  $\text{Li}^+$  transition while prevent the undesired migration of polysulfide anions (Figure 3.8a).<sup>82</sup> Meanwhile, attributed to the good  $\text{Li}^+$  conductivity of the separator, the Li-S battery delivered an initial discharge capacity of  $808 \text{ mA h g}^{-1}$  at  $0.5 \text{ C}$  and maintained  $401 \text{ mA h g}^{-1}$  after 600 cycles with a low capacity decay rate of  $0.083\%$  per cycle (Figure 3.8c).<sup>82</sup>

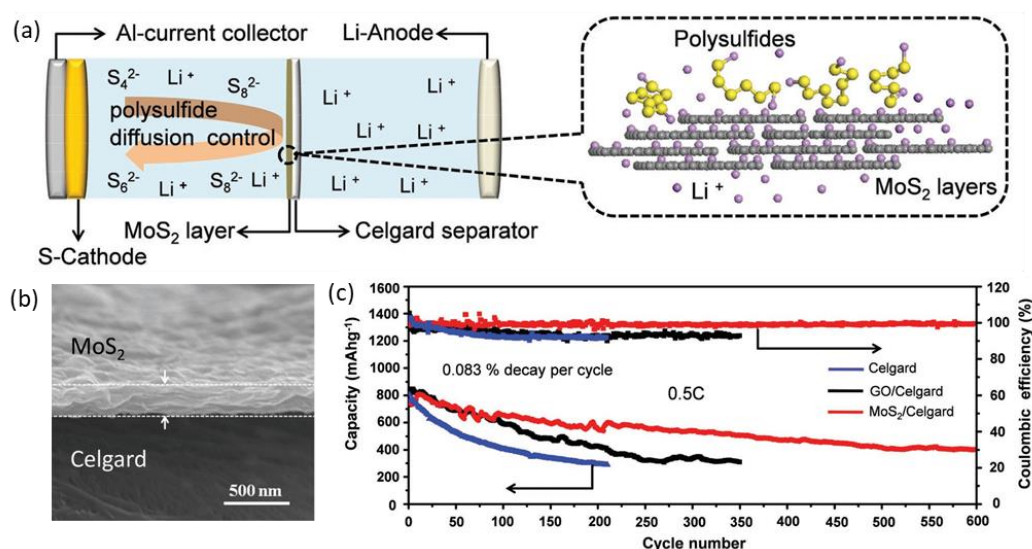


Figure 3.8 (a) Schematic illustration of Li-S cell with a  $\text{MoS}_2$ /Celgard separator, (b) cross section SEM image of a  $\text{MoS}_2$  layer, (c) cycling performance of the Li-S cells with different separators at  $0.5 \text{ C}$ .<sup>82</sup>

### 3.4.3 Organic polymer-based separators

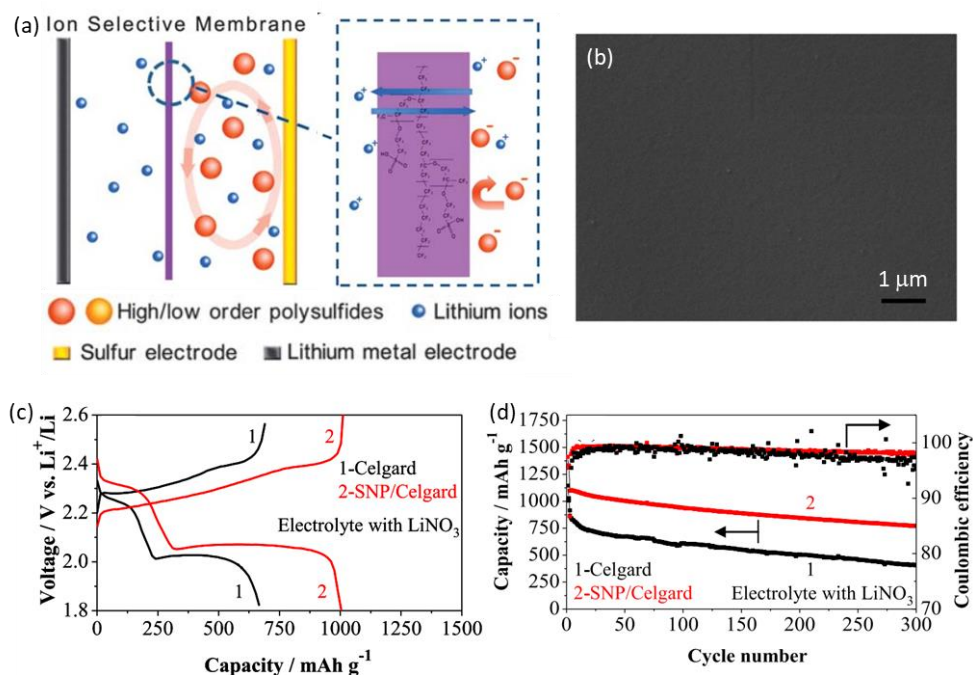


Figure 3.9 (a) Schematic of Li-S cell with an ion-selective separator, in which the separator allows the Li<sup>+</sup> transport while blocks the diffusion of polysulfide anions, (b) SEM image of Nafion-PP/PE/PP membrane.<sup>77</sup> (c) Charge/discharge profiles and (d) cycling performance of the cell with different separators at 1 C.<sup>83</sup>

Except as binders or as functional additives in cathode, polymers recently are used to fabricate separators owing to their good flexibility as well as unique chemical properties.<sup>39, 105</sup> Nafion, a typical polymeric material, possesses a lot of sulfonate-ended perfluoroalkyl ether groups (–SO<sub>3</sub><sup>–</sup>), which allow the hopping of positively charged species while block the diffusion of positively charge species.<sup>77, 83, 106-108</sup> Thus, introducing a Nafion layer onto the separator in Li-S batteries can effectively mitigate the shuttle effect (Figure 3.9a, b).<sup>77</sup> Cai *et al.*<sup>83</sup> coated a lithiated-Nafion-based separator in Li-S batteries, achieving a more higher discharge capacity (1330 mA h g<sup>-1</sup>) at 0.2 C than that of a common Celgard-battery (Figure 3.9c). Furthermore, the lithiated-Nafion-based

cell achieved a high reversible capacity of  $770 \text{ mA h g}^{-1}$  even after 300 cycles at a current density of 1 C (Figure 3.9d).<sup>83</sup> In addition, because the poly(styrenesulfonate) (PSS) also has an appropriate  $-\text{SO}_3^-$  groups on its surface, the separators coated with PSS layer also can work as an electrostatic shield towards polysulfide anions.<sup>109,110</sup> Carboxyl acid groups exhibits good cationic permselectivity, separators grafted carboxyl acid groups also benefit for suppress polysulfides shuttle.<sup>111</sup> Proton-doped conductive polymers, such as polypyrrole (Ppy), polyaniline (PANI), as well as polythiophene (PT), can employ the protons as bridges to combine with polysulfides through hydrogen bonds (H-bonds).<sup>112,113</sup> Furthermore, the conductive polymers with good electronical and ionic conductivity can reduce the interfacial resistance of the batteries, realizing improved rate capability.<sup>114-116</sup>

## Chapter 4. Target and outline of this dissertation

### 4.1 Motivation of this research

Rechargeable Li-S batteries are considered as one of the most promising candidates for next generation electrochemical energy storage systems. However, their practical applications are seriously limited by a series of problems. Recently, massive efforts, including fabricating sulfur-composites cathode materials, introducing stable SEI layer to protect lithium metal anodes and employing functional materials to modify the separators, have been devoted to improving the electrochemical performance of Li-S batteries. Despite some issues can be addressed by stabilizing sulfur cathode and protecting lithium anode, new challenges will be brought. On one hand, introducing too much insulative materials in the cathode will lead to a low sulfur ratio in the cell, which would inevitably sacrifice the overall energy density. On the other hand, introducing an addition layer on the surface of lithium metal will increase the interfacial resistance between lithium anode and electrolyte, resulting poor rate performance. Thus, it seems that modifying separators are more reliable to achieve high performance of Li-S batteries. Nevertheless, numerous strategies have been developed to use functional separators to restrain the shuttle effect, little attentions focus on employing separators to inhibit the growth of lithium dendrites. Besides, although enhanced electrochemical performance of Li-S coin cells with low sulfur loading can be easily achieved, how to develop a high-quality separator for high-performance practical Li-S pouch cell with high sulfur loading is still needed to put in a lot of efforts to exploited and study. Therefore, functional separators that can simultaneously suppress the undesirable polysulfides shuttle and the uncontrolled growth of lithium dendrites (Figure 4.1) should be further developed for comprehensively enhancing the electrochemical performance of practical Li-S batteries.

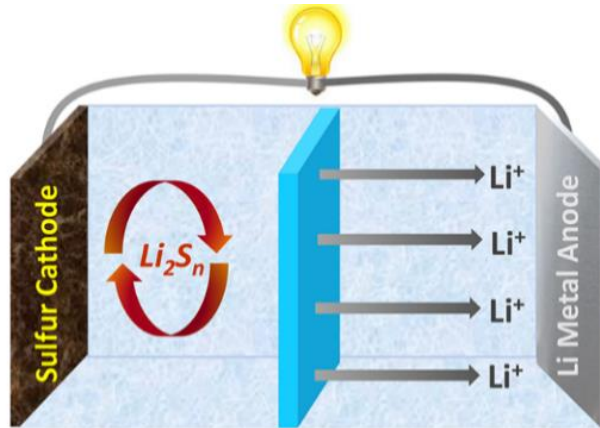


Figure 4.1 Fabricating a functional separator that can simultaneously suppress the polysulfides shuttle and the growth of lithium dendrites.

#### 4.2 Target of this research

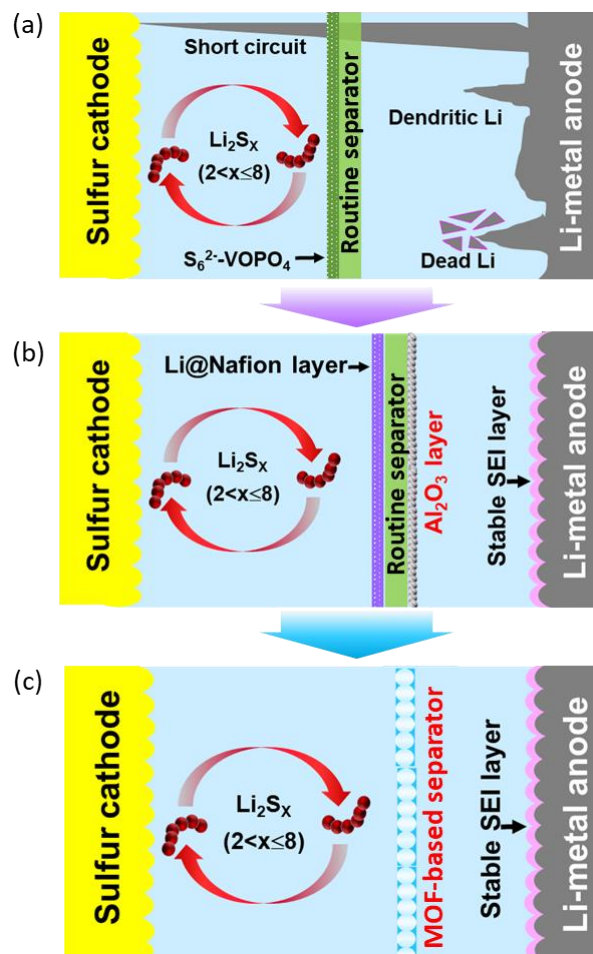


Figure 4.2 The research routes and main target of this research.

The main target of this research is aiming to develop high-quality separators to enhance the utilization of active materials and prolong the cycle life of Li-S batteries.

Details are as follows:

(1) Introducing a functional layer between cathode and routine separator to inhibit the diffusion of polysulfides by physical barrier or repulsion effect (Figure 4.2a);

(2) Coating a function layer on the routine separator faced anode side to suppress the growth of lithium dendrites by regulating the uniform transportation of lithium ions (Figure 4.2b);

(3) Fabricating a free-standing separator with multifunction to simultaneously prevent the polysulfides shuttle and the lithium dendrites growth (Figure 4.2c).

### 4.3 Outline of this thesis

This dissertation consists of the following 8 chapters:

Charter 1 is a general introduction of Li-S batteries, including the historical development, configurations and principles of Li-S batteries.

Chapter 2 introduces the technical challenges of lithium-sulfur batteries, including the insulating nature of sulfur, the shuttle of soluble polysulfides, volume expansion of sulfur cathode, and degradation of the lithium-metal anode.

Chapter 3 illustrates the effective strategies to address the issues in lithium-sulfur batteries, including stabilizing sulfur cathodes, protecting lithium-metal anodes, and modifying separators.

Chapter 4 proposes the motivation and target of this research.

Chapter 5 introduces how to build a “polysulfides-phobic” interface for inhibiting the polysulfides shuttle. The corresponding XPS spectra, Raman observations,

permeation experiments, and electrochemical tests also will be provided to demonstrate the effectivity of the proposed “polysulfides-phobic” strategy;

Chapter 6 introduces respectively employing a lithiated Nafion (Li@Nafion) layer to suppress the polysulfides shuttle by Columbic repulsion and an Al<sub>2</sub>O<sub>3</sub> layer to inhibit the lithium dendrites growth by regulating uniform lithium ions fluxes;

Chapter 7 introduces developing a free-standing MOF-based separator to simultaneously address the issues of polysulfides shuttle and lithium dendrites growth. Moreover, the reliability of practicability of the MOF-based separators also will be demonstrated by the practical Li-S pouch cell with high sulfur loading;

Chapter 8 makes a conclusion of the whole dissertation.

# Chapter 5. Building a “polysulfides-phobic” interface to restrain shuttle effect

## 5.1 Introduction

Rapid development of electric vehicles and portable electronics come up with high demands of the novel energy storage systems in regard to high energy density and long-cycle life. Owing to their ultrahigh theoretical specific capacity ( $1675 \text{ mA h g}^{-1}$ ), rechargeable Li-S batteries are attracted considerable attentions.<sup>117-119</sup> However, the fatal effects aroused by undesirable polysulfides shuttle would give rise to low sulfur utilization and rapid decay of capacity.<sup>1, 120, 121</sup> Thus, the actual performance of Li-S batteries is difficult to reach the theoretical value, and their practical applications are still up against enormous challenges.<sup>122-124</sup>

Over the past decades, enormous efforts have been devoted to addressing aforesaid issues.<sup>40, 80, 125-129</sup> One of the most popular strategies to restrain shuttle effect is introducing porous materials and/or polar materials as the hosts of sulfur. Thus, the produced polysulfides intermediates can be confined within holes of the porous hosts by physical adsorption or anchored by polar materials via chemical bonding.<sup>130-135</sup> Despite the polysulfides shuttle can be indeed mitigated to some degree by the adsorption/bonding strategies, it is unable to immobilize the polysulfides too long time due to unstable cathode structure suffered from the violent volume expansion.<sup>136, 137</sup> In addition, the insulative nature of most polar materials needs high content of conductivity additive, thus leading to a low sulfur ratio, which is difficult to achieve high energy density of the battery. In this case, introducing a barrier layer on the separator towards the cathode seems more reliable, since it would not bring any negative influences on the cathode.

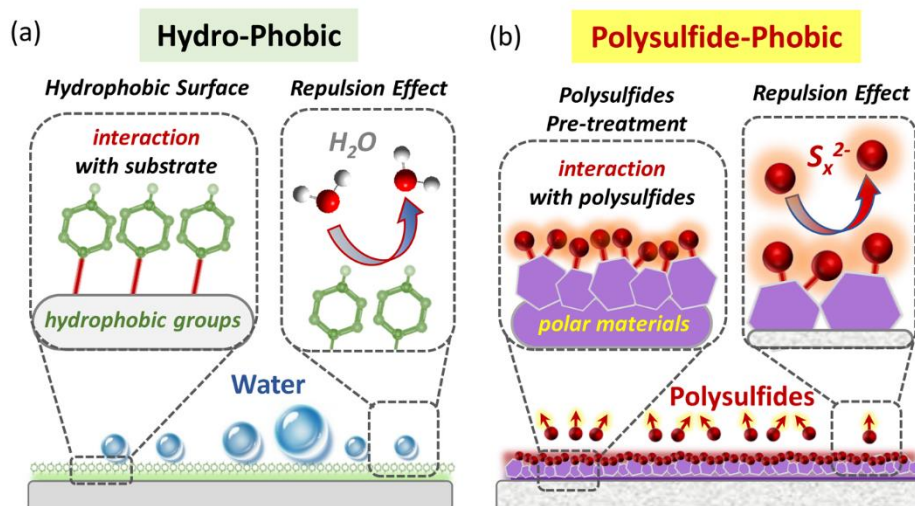


Figure 5.1 Schematics of (a) a hydro-phobic surface by anchoring hydrophobic groups on the substrate and (b) a polysulfide-phobic surface by immobilizing polysulfides on the polar materials.

The hydrophobic effect is a very important nonspecific interaction in biological owing to its significant guiding significance in fundamental researches and practical applications. According to the hydrophobic mechanism of some biological materials (*e.g.* lotus leaves, butterfly wings, fish scales, *et al.*), a large number of artificial hydrophobic surfaces have been built by introducing various hydrophobic groups on the substrates (Figure 5.1a). The popular hydrophobic groups include ethyl, ethyl, n-butyl, and so on.<sup>138</sup> The constructed hydrophobic surfaces have strong repulsion effect on the approaching  $H_2O$  molecules, producing a self-cleaning surface to reduce the dust contamination erosion and accumulation.<sup>139</sup> Herein, enlightened by the hydrophobic repulsion effect towards the water molecules, we render a novel strategy that building a “polysulfide-phobic” interface to mitigate the shuttle of polysulfide anions. Owing to the electronegativity of polysulfide anions, we employed the polysulfides themselves as the polysulfide-phobic groups to construct the polysulfide-phobic surface, in which the polar materials are used as substrates to anchor the polysulfides by chemical bonding to form a

stable interface (Figure 5.1b). The as-constructed polysulfide-phobic surface can reject the diffusion of polysulfides ions by the Coulomb repulsion.

## 5.2 Experiment and characterization

### 5.2.1 Chemicals and materials

Vanadium pentoxide ( $V_2O_5$ ), sulfur ( $S_8$ ), sodium thiosulfate ( $N_2S_2O_3$ ) and 1, 3-dioxolane (DOL, >99.9%) were purchased from Tokyo Chemical Industry Co., Ltd. Phosphoric acid ( $H_3PO_4$ , 85%), hydrochloric acid (HCl, 35%~37%), 2-propanol and 1,2-dimethoxymethane (DME, >99.9%) were obtained from FUJIFILM Wako Pure Chemical Corporation. Lithium sulfide ( $Li_2S$ , 99.9% purity), lithium bis(trifluoromethanesulfonyl)imide (LiTFSI) and lithium nitrate ( $LiNO_3$ ) were purchased from Sigma-Aldrich. Celgard 2400 (PP) membranes were obtained from Celgard company.

### 5.2.2 Synthesis of $Li_2S_6$ in DOL/DME

The  $Li_2S_6$  solution was synthesized according to a reported method.<sup>140</sup> In detail,  $S_8$  powder and  $Li_2S$  powder were mixed with a molar ratio of 3:4 in a glass bottle under protection of Argon. Then a mixed solvent of DME and DOL, with a volume ratio of 1:1 was added into the glass bottle under mild stirring. After continuously stirring at 50 °C for 12 h, a red-brown  $Li_2S_6$  solution was finally obtained.

### 5.2.3 Fabrication of flexible $S_6^{2-}$ -VOPO<sub>4</sub>/PP membranes

Preparation of VOPO<sub>4</sub>·2H<sub>2</sub>O precursor. The bulk VOPO<sub>4</sub>·2H<sub>2</sub>O precursor was prepared according a reflux method reported by the reference.<sup>141, 142</sup> Briefly, 2.4 g  $V_2O_5$  was added into a mixture of  $H_3PO_4$  (13.3 mL) and  $H_2O$  (67.7 mL) under stirring. After refluxing at 110 °C for 16 h, the system was naturally cooled down to room temperature. The resulting luminous yellow precipitate was collected by filtration, washed several

times with acetone. Finally, the as-prepared products were dried in vacuum oven at 60 °C for 12 h to obtain VOPO<sub>4</sub>·2H<sub>2</sub>O powder.

Preparation of VOPO<sub>4</sub>/PP membranes. To prepare flexible VOPO<sub>4</sub>/PP membranes, 100 mg VOPO<sub>4</sub>·2H<sub>2</sub>O yellow powder was dispersed in 200 mL 2-propanol. After stirring for 1 h, the obtained suspension was ultrasonicated in iced water for 5 h to exfoliate the bulk VOPO<sub>4</sub>·2H<sub>2</sub>O, then the VOPO<sub>4</sub> nanosheets suspension with a concentration of 0.5 mg mL<sup>-1</sup> was obtained. The flexible VOPO<sub>4</sub>/PP membranes were fabricated via a simple and mild self-assembly strategy. In detail, 30 ml VOPO<sub>4</sub> nanosheets suspension was firstly filtered through a conventional PP filter membrane. After the 2-propanol solvent was removed, the obtained VOPO<sub>4</sub>/PP membranes (abbreviated as VPP) were dried at 60 °C for 12 h in a vacuum oven before using.

Fabrication of S<sub>6</sub><sup>2-</sup>-VOPO<sub>4</sub>/PP membranes. The as-prepared VOPO<sub>4</sub>/PP membranes were firstly cut into wafers with diameter of 16 mm. Then the small VOPO<sub>4</sub>/PP wafers were immersed in Li<sub>2</sub>S<sub>6</sub> solution for 12 h under the protection of Argon. After fully reaction with polysulfides, the small VOPO<sub>4</sub>/PP wafers were washed several times by immersing in pure DME solvent to remove the redundant Li<sub>2</sub>S<sub>6</sub>. Finally, the S<sub>6</sub><sup>2-</sup> treated VOPO<sub>4</sub>/PP (abbreviated as S<sub>6</sub><sup>2-</sup>-VPP) membranes were dried by vacuum valve before using.

#### 5.2.4 Preparation of graphene@sulfur cathode materials

The graphene@sulfur composite materials were prepared by a self-assembled method.<sup>143</sup> In detail, Na<sub>2</sub>S<sub>2</sub>O<sub>3</sub> power (79 mg) was added in GO suspension (1 mg mL<sup>-1</sup>, 24 mL). After stirring for 1 h, the mixed Na<sub>2</sub>S<sub>2</sub>O<sub>3</sub>/GO solution was treated by an ultrasonic processing for 0.5 h. Then, HCl (5 M, 0.1 mL) was introduced. After continually stirring for 0.5 h, the obtained yellow brown muddy liquid mixture was sealed in a glass vial, which was heated at 95 °C for 4 h. After the GO was completely reduced

to form reduced graphene oxide (RGO), the products were washed by ultrapure water to remove the extra impurities and ions. Lastly, the obtained reduced graphene oxide/sulfur (RGO@S) hybrid composites was freeze-dried for 10 h. The sulfur content calculated by thermogravimetric analysis (TGA) was about 87%.

### 5.2.5 Lithium-sulfur cells assembly

All Li-S coin cells were assembled in an Argon filled glove box with moisture and oxygen contents below 1 ppm. The cathode was prepared mixing the RGO@S, carbon black and PVDF (8:1:1 by weight) in NMP to form a slurry. Then the mixed slurry was coated on the aluminium foil. After drying at 70 °C for 12 h in a vacuum oven, the mixture coated aluminium foil was cut into wafers with diameter of 11 mm to be used as cathodes (sulfur loading~ 1 mg cm<sup>-2</sup>). The anodes were prepared by directly pressing Li metal foils on stainless steel foils. The electrolyte was 1 M LiTFSI in DOL and DME (1:1 by volume) with 2 wt% LiNO<sub>3</sub> as additive. The addition amount of electrolyte in every cell was about 30 μL. The commercial Celgard 2400 (PP) and the as-prepared S<sub>6</sub><sup>2-</sup>-VPP membranes with diameter of 16 mm were used as separators. It should be noted that the S<sub>6</sub><sup>2-</sup>-VOPO<sub>4</sub> coating layer was faced to cathode side. Standard 2032 coin cells were used to evaluate the electrochemical performance of Li-S batteries.

### 5.2.6 Characterization

LEO Gemini Supra 35 system and SU8020 field-emission scanning electron microscopy (FE-SEM) was used to reveal the morphologies of the samples. The X-ray diffraction (XRD) patterns were performed by scanning from 5° to 50° under an operating voltage of 40 kV and a current of 40 mA on a Bruker D8 Advanced diffractometer fitted with Cu-Kα X-rays ( $\lambda = 1.5406\text{\AA}$ ) radiation. X-ray photoelectron spectroscopy (XPS) spectra was obtained from the AXIS ULTRA (Kratos Analytical Ltd.) using Al Ka

radiation (1486.6 eV) as an excitation source. Zeta potentials were measured by using the Electrophoretic Light Scattering (ELS) (Malvern Instruments Ltd). The materials were dispersed into 2-propanol. Thermogravimetric analysis (TGA) data were obtained from an AXIS ULTRA under the protection of N<sub>2</sub> atmosphere in a temperature range from 20 to 500 C at a heating rate of 5 C min<sup>-1</sup>.

### 5.2.7 Raman Measurements

The Raman spectra were obtained by a Renishaw in Via microscope Spectrometer. A 50×long working distance lens (Olympus America Inc.) was employed. The confocal slit was 4.0 μm. The collection time of Raman spectrum was about 45~60 s. During operando testing, the sample (plate and electrolyte solution) is sealed within an Ar-gas tight home-made cell. Besides, the SiO<sub>2</sub> wrapped gold nanoparticles with diameter around 40 nm<sup>144</sup> were used as enhanced additives, which were coated on the surface of VOPO<sub>4</sub> before assembly. As for the time/space-resolution operando testing, the Au@SiO<sub>2</sub> nano particles were dispersed into the as-prepared polysulfide solution.

### 5.2.8 Ionic conductivity

The ionic conductivity was performed carried out by a symmetric coin cell assembled by two stainless steel electrodes. The separators (PP or S<sub>6</sub><sup>2-</sup>-VPP membranes) were saturated with same electrolyte with Li-S coin cells. The value of ionic conductivity was calculated from EIS according to the following equation (Equation 5.1).<sup>82</sup>

$$\sigma = d/(RA) \quad (\text{Equation 5.1})$$

In which  $\sigma$  is the ionic conductivity (S cm<sup>-1</sup>),  $d$  refers to the thickness of separator (cm),  $R$  stands for the resistance ( $\Omega$ ), and  $A$  represents the area of stainless steel electrode (cm<sup>2</sup>).

### 5.2.9 Transference number of lithium ions

The Li<sup>+</sup> transference number was evaluated by a potentiostatic polarization

method in a Li//Li symmetric coin cell, and the separator was PP membrane or S<sub>6</sub><sup>2-</sup>-VPP membrane saturated with 0.3 M Li<sub>2</sub>S<sub>6</sub> electrolyte. The potentiostatic polarization process was performed with a constant potential at 20 mV for 10000s to record the current at initial and steady-state. Besides, before and after the potentiostatic polarization, the EIS were also needed to be collected. The Li<sup>+</sup> transference number was calculated according to the following equation (Equation 5.2).<sup>145, 146</sup>

$$t_{Li^+} = I_{ss}(\Delta V - I_0 R_0) / I_0(\Delta V - I_{ss} R_{ss}) \quad (\text{Equation 5.2})$$

In which  $t_{Li^+}$  stands for the Li<sup>+</sup> transference number,  $I_0$  and  $I_{ss}$  is the current at initial and steady-state (mA),  $R_0$  and  $R_{ss}$  presents for the resistance before and after the potentiostatic polarization ( $\Omega$ ),  $\Delta V$  is the potentiostatic potential (V).

### 5.2.10 Electrochemical measurements

Cyclic voltammetry (CV) and electrochemical impedance spectroscopy (EIS) were carried out by using Solartron 1470 system. CV curves were collected at various scan rates within a potential window of 1.7~2.8 V versus Li/Li<sup>+</sup>. The EIS was measured in a frequency range of 100 kHz to 0.01 Hz with amplitude of 5 mV. The galvanostatic charge/discharge were carried out by using a Hokuto system at room temperature. Cycling stability of Li-S cells were measured galvanostatically at various charge/discharge rates within a potential window of 1.7~2.8 V versus Li/Li<sup>+</sup>. The mass specific capacities were calculated based on the total mass of sulfur in this paper.

## 5.3 Results and Discussions

### 5.3.1 Immobilization of polysulfides on VOPO<sub>4</sub>

Herein, we employed the 2D vanadyl phosphate (VOPO<sub>4</sub>) sheets with a typical layered structure as the polar materials to anchor the polysulfides. The VOPO<sub>4</sub> sheets were obtained from vanadyl phosphate dihydrate (VOPO<sub>4</sub>·2H<sub>2</sub>O) with a typical two

dimensional layered structure, in which the  $\text{VOPO}_4$  sheets form the linked vertex-sharing  $\text{VO}_6$  octahedra and phosphate  $\text{PO}_4$  tetrahedra.<sup>147</sup> The X-ray powder diffraction (XRD) pattern of the pristine bulk  $\text{VOPO}_4 \cdot 2\text{H}_2\text{O}$  precursor is shown in Figure 5.2a. All the characteristic peaks can be readily indexed to the tetragonal  $\text{VOPO}_4 \cdot 2\text{H}_2\text{O}$  (JCPDS card NO. 84-0111) with  $P4/nmm$  space group ( $a = 6.202 \text{ \AA}$ ,  $b = 6.202 \text{ \AA}$ ,  $c = 7.410 \text{ \AA}$ ).<sup>147</sup> The Field emission scanning electron microscopy (FE-SEM) image (Figure 5.2b) further exhibits the characteristic layered structure of the bulk  $\text{VOPO}_4 \cdot 2\text{H}_2\text{O}$ , of which the  $\text{VOPO}_4$  sheets were tightly stacked. After a period of strong ultrasonication treated in 2-propanol solution, the hydrogen bonds between the  $\text{H}_2\text{O}$  molecules and  $\text{VOPO}_4$  sheets were destroyed and pure  $\text{VOPO}_4$  sheets were obtained.<sup>147</sup>

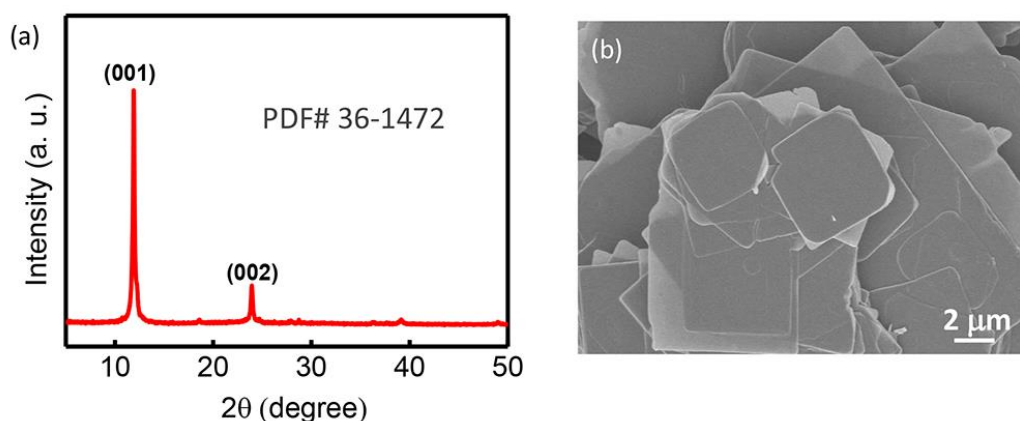


Figure 5.2 (a) XRD pattern and (b) FE-SEM image of layered  $\text{VOPO}_4 \cdot 2\text{H}_2\text{O}$ .

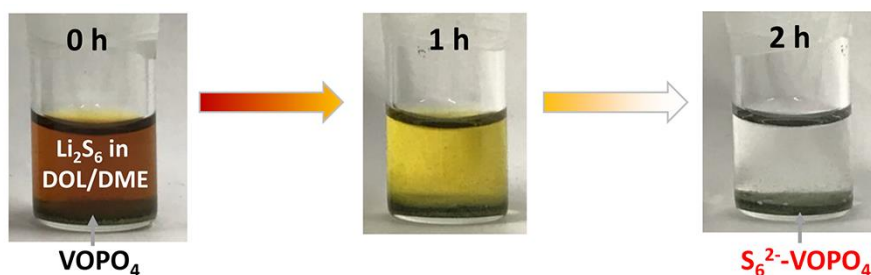


Figure 5.3 The color change of a  $\text{Li}_2\text{S}_6$  solution after introducing  $\text{VOPO}_4$  sheets with the increase of rest time.

The immobilization of polysulfides on the VOPO<sub>4</sub> sheets was carried out by adding VOPO<sub>4</sub> sheets into a Li<sub>2</sub>S<sub>6</sub> DME/DOL solution. From the Figure 5.3, we can see that the color of rufous Li<sub>2</sub>S<sub>6</sub> solution gradually faded with the increase of rest time, indicating a strong interaction between the polysulfides and VOPO<sub>4</sub> sheets. X-ray photoelectron spectroscopy (XPS) was employed to analyze the surface compositions and chemical states of VOPO<sub>4</sub> before and after treating in Li<sub>2</sub>S<sub>6</sub> solution. As shown in Figure 5.4a, obvious S 2s and S 2p peaks appear on the survey spectrum of Li<sub>2</sub>S<sub>6</sub>-treated VOPO<sub>4</sub>, suggesting that effective absorption of VOPO<sub>4</sub> sheets towards polysulfides. In addition, the deconvoluted S 2p XPS spectrum exhibited two distinct peaks at 164.2 and 162.9 eV (Figure 5.4b), which are assigned to bridging sulfur (S<sub>B</sub><sup>0</sup>) and terminal sulfur (S<sub>T</sub><sup>-1</sup>), respectively.<sup>149</sup> The splitting of S 2p peaks is rationally resulted from the change of complex chemical environment of S. In the meanwhile, the V 2p peaks of VOPO<sub>4</sub> at 524.6 and 517.1 eV assigned to V 2p<sub>1/2</sub> and V 2p<sub>3/2</sub> were shifted to lower binding energies 523.8 and 516.4 eV after treating in Li<sub>2</sub>S<sub>6</sub> solution (Figure 5.4c), further confirming that a new local environment of V was formed after anchored with polysulfide species.

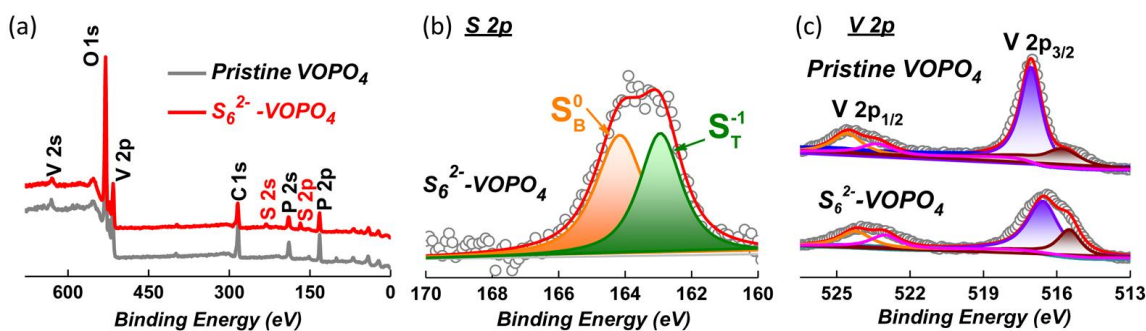


Figure 5.4 (a) Wide-scan survey XPS spectra of pristine VOPO<sub>4</sub> and S<sub>6</sub><sup>2-</sup>-VOPO<sub>4</sub>. (b) S 2p and (c) V 2p elemental XPS spectra of S<sub>6</sub><sup>2-</sup>-VOPO<sub>4</sub>.

Then, we employed the time-resolved operando Raman spectroscopy to further investigate the variation trend of polysulfide adsorption state. As shown in Figure 5.5a

and 5.5b, profiting by the shell-isolated nanoparticle-enhanced Raman spectroscopy (SHINER) technology, surface information of VOPO<sub>4</sub> was obtained after soaking into polysulfide (S<sub>6</sub><sup>2-</sup>)-contained solution. It should be noted that the tested samples were pre-deposited by SiO<sub>2</sub>@Au-based surface-enhanced additive to reduce the interference information. After treated within polysulfides solution, the shift of original VOPO<sub>4</sub>-related Raman peaks (PO<sub>4</sub> stretching and PO<sub>4</sub> bending/stretching, etc.) exhibit well coincide with the corresponding change of local environment, which was revealed by XPS observation. Additionally, a pair of new peaks located at 218 and 358 cm<sup>-1</sup> were appeared, assigning to the adsorbed S<sub>6</sub><sup>2-</sup> and S<sub>8</sub><sup>2-</sup> polysulfide species (S-S stretching modes,  $\nu_s$ ). It should be mentioned that although the as-prepared polysulfide solution is dominated by S<sub>6</sub><sup>2-</sup>, a small amount of S<sub>8</sub><sup>2-</sup> can be detected, which was resulted from the typical polysulfides disproportionate reactions. According to the Raman spectrum of vanadium sulfide, this newly appeared peak can be ascribed to the V-S stretching mode within surface anchored with polysulfide species.<sup>148</sup> Furthermore, from the time-resolution spectroscopic information (Figure 5.5c, d), it can be seen that the adsorption of polysulfide gradually increased and finally reached a saturation point after 75 min aging.

On the contrary, no obvious desorption can be observed during the continuous soaking/aging, implying that the polysulfides-saturated VOPO<sub>4</sub> surface kept a stable state. In this case, the evidence obtained from Raman results demonstrated the chemical adsorption interaction between VOPO<sub>4</sub> host and polysulfide is stable and it can reach to a saturation state. The relationship between the amount of VOPO<sub>4</sub> and the adsorbed amount of polysulfides is shown in Figure 5.6. It can be concluded that when the available vacancies of VOPO<sub>4</sub> are fully occupied by polysulfides, the absorbed polysulfides satisfy the relational expression of  $m_{PS}=0.35 m_V$  ( $m_V$  represents the mass of VOPO<sub>4</sub> while  $m_{PS}$

stands for the mass of absorbed polysulfides, which was calculated by the mass difference between the  $S_6^{2-}$ -VOPO<sub>4</sub> and pristine VOPO<sub>4</sub>).

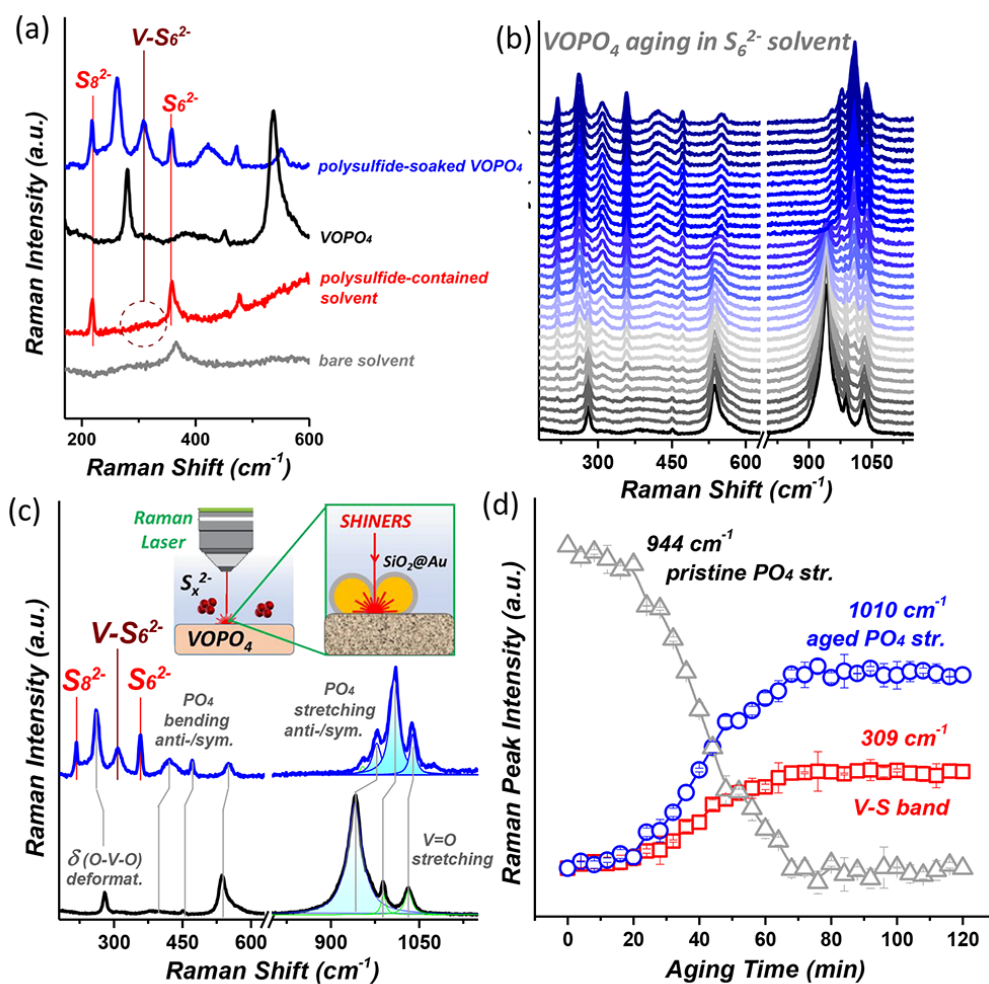


Figure 5.5 (a) Raman peak assignments for S-S and V-S stretching modes within obtained spectra. (b) Raman spectra collected on the surface of VOPO<sub>4</sub> after different aging time. (c) Raman peak assignments: at the pristine state (black trace) and after 2 hours aging (blue trace), respectively. (d) Time-dependence of specific Raman peak intensities, which directly read from the operando spectra.

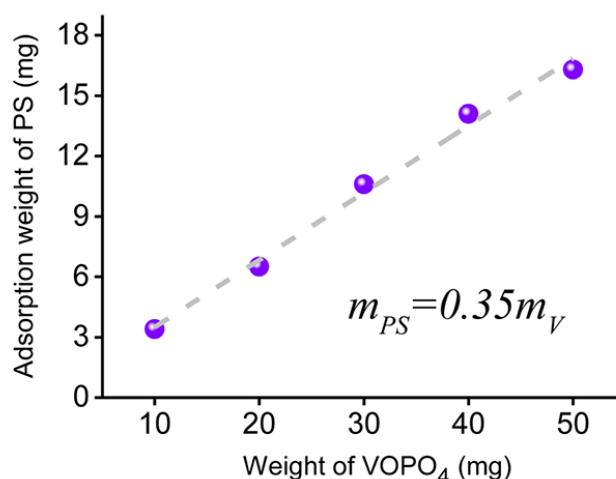


Figure 5.6 The relationship between the amount of VOPO<sub>4</sub> and the adsorbed amount of polysulfides.

### 5.3.2 The effect of S<sub>6</sub><sup>2-</sup>-VOPO<sub>4</sub> on the polysulfide anions

Zeta potential analysis was employed to reveal the surface charge of S<sub>6</sub><sup>2-</sup>-treated VOPO<sub>4</sub>. Both the VOPO<sub>4</sub> and S<sub>6</sub><sup>2-</sup>-treated VOPO<sub>4</sub> powder were dispersed in 2-propanol. As shown in Figure 5.7, the pristine VOPO<sub>4</sub> shows a Zeta-potential of 0.26 mV, suggesting that the pure VOPO<sub>4</sub> is electrically neutral. On the contrary, the S<sub>6</sub><sup>2-</sup>-treated VOPO<sub>4</sub> exhibits a value of -31.70 mV, indicating the electronegativity of the S<sub>6</sub><sup>2-</sup>-VOPO<sub>4</sub>.

To further elucidate the effect of S<sub>6</sub><sup>2-</sup>-treated VOPO<sub>4</sub> on the dissolved polysulfide anions, the advanced time/space-resolved operando Raman observation was employed (Figure 5.8). It is worth emphasizing that the Raman laser beam herein was focused on the polysulfide-contained solution near the interlayer rather than the VOPO<sub>4</sub> surface, thus we can collect the information of concentration distributions of soluble polysulfides in different spaces with the solution. It can be seen from the inset of Figure 5.8a that the related Raman signals were collected by shifting the laser beam away from the VOPO<sub>4</sub>

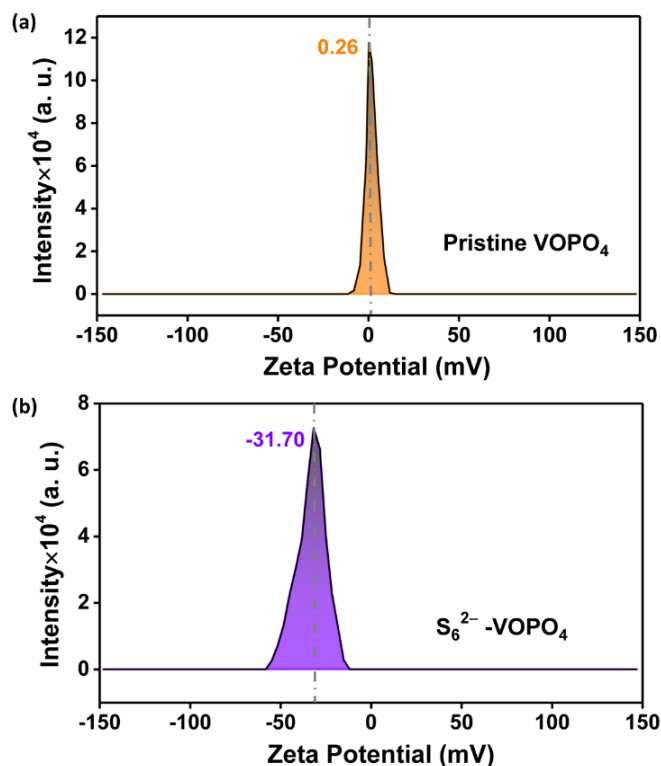


Figure 5.7 Zeta potential results of (a) the pristine VOPO<sub>4</sub> powder and (b) the S<sub>6</sub><sup>2-</sup>-VOPO<sub>4</sub> dispersed in 2-propanol.

after different aging times. It should be noted that due to the too big size of Raman beam (1~2 μm in diameter), although the laser spot was just focused on the solution region near the solid/liquid interface, some adsorption information from surface can inevitably be collected. In this case, the characteristic peak of surface adsorbed V-S<sub>6</sub><sup>2-</sup> (307 cm<sup>-1</sup>) was observed from the several initial spectra recorded near the VOPO<sub>4</sub> surface (bottom black traces, Figure 5.8a), then gradually reduced as the divorcing/removing laser beam away from VOPO<sub>4</sub> surface, and finally disappeared (upper blue traces, Figure 5.8a). In another word, the collected Raman information of polysulfides were attributed to two sections: surface adsorbed and bulk dissolved, which are illustrated in Figure 5.8b. As summarized in Figure 5.8c, the peak intensity of S-S stretching mode was composed of adsorbed polysulfides and dissolved polysulfides (ν<sub>s</sub> within S<sub>6</sub><sup>2-</sup>, upper pattern in Figure 5.8c).

Fortunately, the independent peak located at  $309\text{ cm}^{-1}$  corresponding to the V-S stretch within adsorbed polysulfide exhibits an obvious change trend of adsorbed polysulfide (middle pattern in Figure 5.8c). In this case, the time/space-distribution of dissolved polysulfide can be normalized based on the intensity distribution of non-overlapped V-S stretch (bottom pattern in Figure 5.8c).

With the accumulation of polysulfide species on the surface of  $\text{VOPO}_4$ , the concentration of dissolved polysulfides shows a distinct gradient distribution (red blocks, Figure 5.8d). To be specific, in the region close to the surface anchored with polysulfides, the concentration of dissolved polysulfides is much lower than the one recorded in the dissolved solution. Besides, the concentration gaps of dissolved polysulfide are gradually increased till reached to the saturation point of adsorption (around 75 min soaking). The results implied that the surface anchored with negatively charged polysulfide anions can evolve into a polysulfide-phobic surface, which can prevent the migration of polysulfide anions (Figure 5.8d). This repulsion effect can be rationally attributed to the charge interaction, a typical Coulomb interaction between immobilized polysulfides and dissolved polysulfide anions. Evidences provided by Raman spectroscopy convincingly demonstrated that the polysulfide-phobic interface can repulse the approaching polysulfide anions. Such a unique repulsion effect also can be further interpreted as a “self-defence” mechanism against the migration of polysulfide anions. To our best knowledge, this is a very original/novel employment strategy/mode for the polar hosts of polysulfide anions in Li-S battery techniques. More significantly, not merely limited within  $\text{VOPO}_4$ , the built theoretical model can be further employed to develop other polar materials as polysulfide hosts to construct a polysulfides-phobic surface/interface. Certainly, the polar materials anchored with polysulfides should be keep stable during continues charging/discharging process in a Li-S battery system.

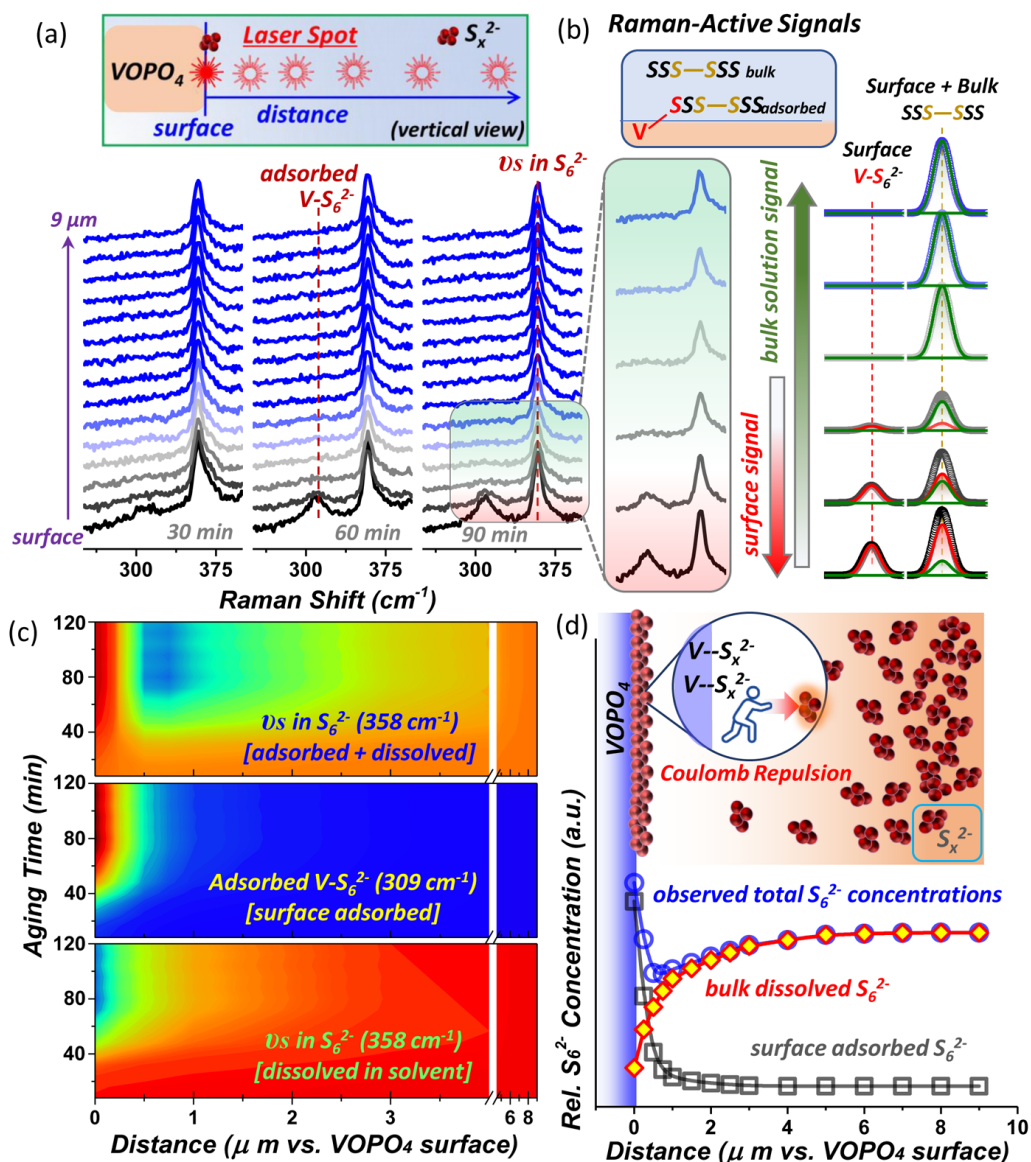


Figure 5.8 (a) Above: schematic illustration the operation process of Raman information; below: the obtained Raman spectra at different distances away from VOPO<sub>4</sub>/polysulfide solution interface. (b) The enlarged Raman spectra in the square of (a). Because of the too big size of Raman laser spot (1~2 μm), the Raman information/signal obtained from near the interface is inevitably composed of both surface adsorbed polysulfides and dissolved polysulfide anions. (c) Time/space (x/y-axis) resolved contour plots evolution of specific Raman peak intensities. (d) The concentrations of adsorbed/dissolved polysulfide at different place with the schematic of repulsion effect of the VOPO<sub>4</sub> surface anchored with towards the free polysulfides anions in the solution.

### 5.3.3 Permselectivity of $S_6^{2-}$ -VOPO<sub>4</sub>/PP membrane

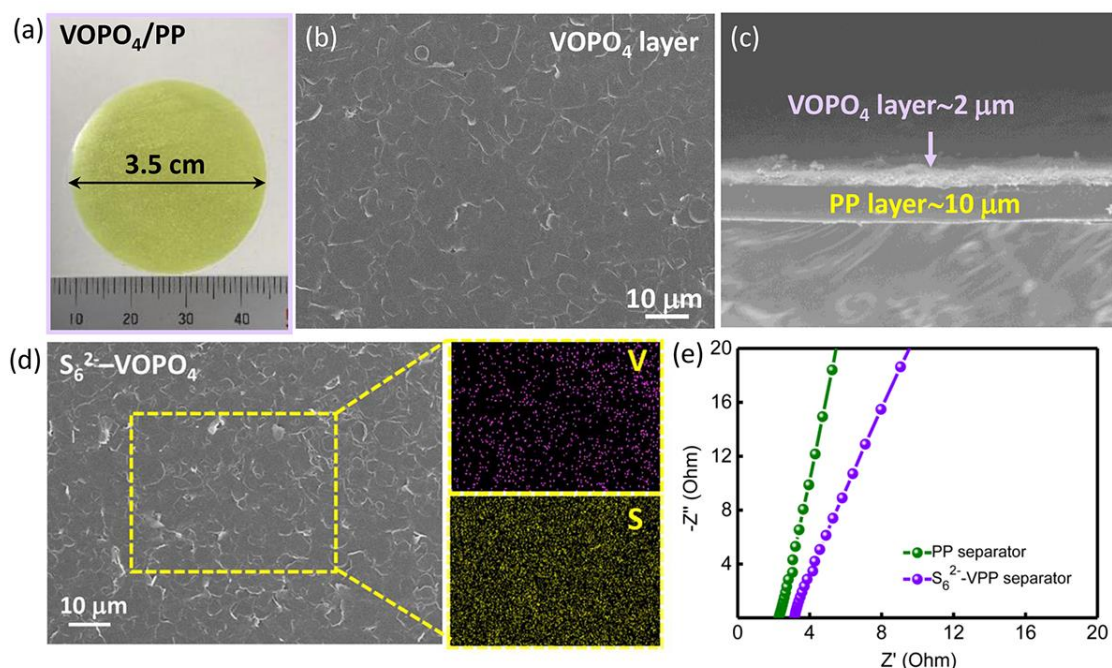


Figure 5.9 (a) Digital photos, (b) top-view and (c) side-view FE-SEM images of VOPO<sub>4</sub>/PP membrane. (d) FE-SEM image of  $S_6^{2-}$ -VPP separator with the corresponding elemental maps of V and S within the squared area. (e) Electrochemical impedance spectra of PP and  $S_6^{2-}$ -VPP separators.

After confirming that the anchored polysulfides can evolve into a polysulfide-phobic surface, we fabricated VOPO<sub>4</sub>/PP (abbreviated as VPP) membranes and then treated them in a Li<sub>2</sub>S<sub>6</sub> DME/DOL solution to comprehensively evaluate their reliability and practicability in Li-S batteries. The thin VPP membranes (Figure 5.9a) were fabricated by vacuum filtering a small amount of exfoliated VOPO<sub>4</sub>/2-propanol dispersion onto conventional PP membranes. The corresponding FE-SEM images show the VOPO<sub>4</sub> sheets with a uniform distribution on the PP membrane (Figure 5.9b). The cross-section SEM image reveal that the thicknesses of the VOPO<sub>4</sub> layer and the PP layer are about 2 and 10 μm, respectively (Figure 5.9c). Then the as-prepared VPP membranes

were immersed in a  $\text{Li}_2\text{S}_6$  DME/DOL solution to immobilize the polysulfides on the surface of  $\text{VOPO}_4$  (abbreviated as  $\text{S}_6^{2-}$ -VPP), forming a polysulfide-phobic surface. The FE-SEM image and the corresponding EDX maps of V and S elementals suggested that the polysulfides distributed uniformly on the surface of  $\text{VOPO}_4$  sheets (Figure 5.9d). The ion conductivity was carried out by using a stainless steel/stainless steel symmetric coin cell with different separator/electrolyte systems. From the Figure 5.9e, it can be seen that the ion conductivity of the  $\text{S}_6^{2-}$ -VPP saturated with electrolyte system was calculated to be  $0.11 \text{ mS cm}^{-1}$  at room temperature, which was only slightly lower than that of a pure PP/electrolyte system ( $0.14 \text{ mS cm}^{-1}$ ), indicating that introduction of a thin  $\text{VOPO}_4$  layer almost has no any negative influences on the  $\text{Li}^+$  transport.

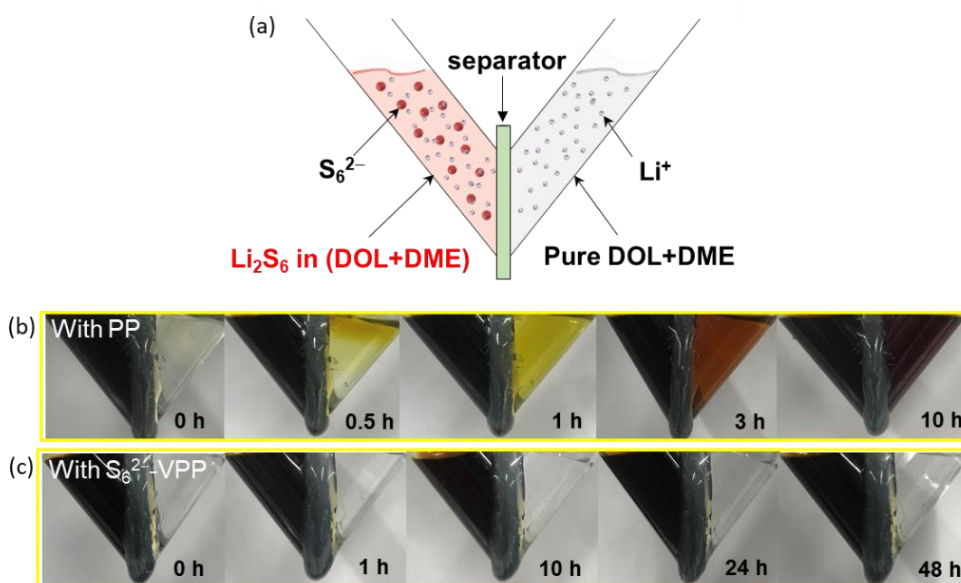


Figure 5.10 (a) Schematic diagram of V-type device. Optical images of the diffusion of polysulfides: visualized V-type glass devices with (b) a routine PP separator and (c) a  $\text{S}_6^{2-}$ -VPP separator.

Then visualized V-type glass devices were designed and assembled to intuitively observe the availability of  $\text{S}_6^{2-}$ -VPP separator on blocking the polysulfides shuttle (Figure 5.10a). The DOL/DME solvent with  $0.3 \text{ M Li}_2\text{S}_6$  was injected in the left chamber and the

pure solvent without polysulfides was injected in the right chamber. The two chambers were separated by pure PP separator or the  $S_6^{2-}$ -VPP separator. For the V-type device with a routine PP separator, it can be seen that the red-brown polysulfides gradually passed through the separator from left chamber to right chamber and reached a highest level after 10 h rest (Figure 5.10b), suggesting that the pure PP is difficult to inhibit the polysulfides diffusion. To the contrary, no obvious polysulfides diffusion phenomenon can be observed from the V-type device with a  $S_6^{2-}$ -VPP separator even after 48 h rest (Figure 5.10c), convincingly demonstrating that the  $S_6^{2-}$ -VPP separator can effectively prevent the penetration of dissolved polysulfide species.

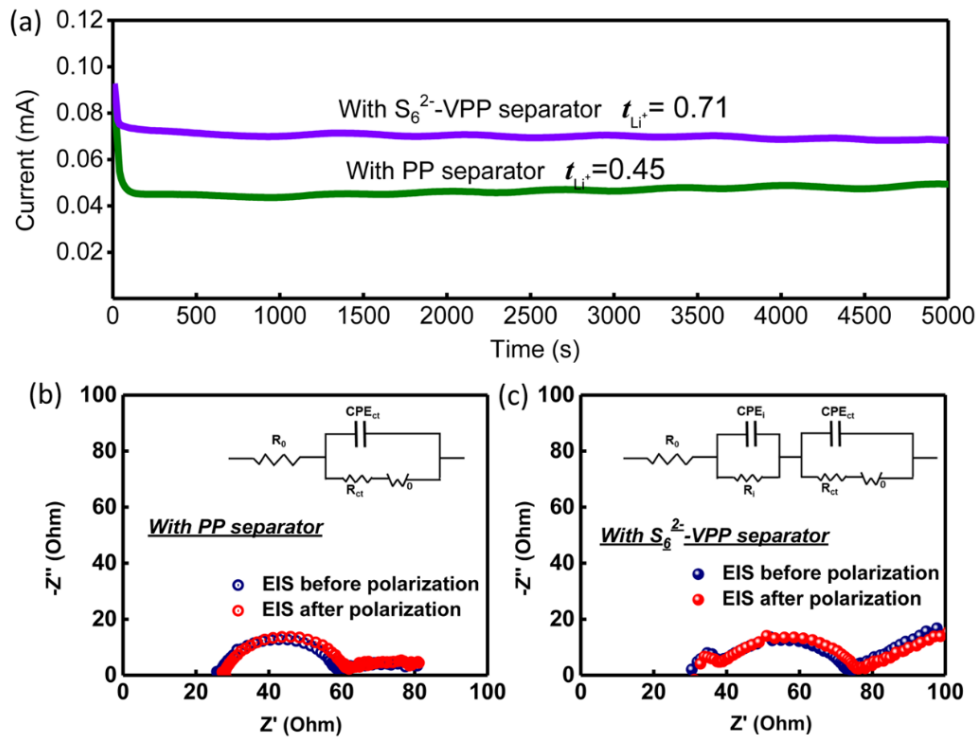


Figure 5.11 The characteristic of  $Li^+$  transference number. (a) Polarization curves of symmetric cells with different separators. Electrochemical impedance spectra (b) with pure PP separator and (c) with  $S_6^{2-}$ -VPP separator, respectively. The insets of EIS spectra for the batteries with different separators are the equivalent circuit models.  $R_0$ : resistance of the electrolyte,  $R_{ct}$ : charge transfer resistance at the electrodes, CPE: constant phase element about the double layer capacitance,  $W_0$ : Warburg impedance.

The lithium ions transference number ( $t_{Li^+}$ ) associated with a  $Li_2S_6$  DME/DOL electrolyte was further measured to verify the permselectivity of  $S_6^{2-}$ -VPP separator (Figure 5.11). As a result, The  $t_{Li^+}$  of the pure routine PP/ $Li_2S_6$  electrolyte system was calculated to be 0.45, which is agree with the reported values. Replacing the PP membrane with a pre-treated  $S_6^{2-}$ -VPP separator, the  $t_{Li^+}$  was prominently enhanced to 0.71, which is not only ascribed to the restriction of polysulfide diffusion (electrostatic repulsion) but also resulted from the acceleration of Li ions hopping (electrostatic attraction). The enhanced  $Li^+$  transference number is beneficial for a higher attainable charge state at high rate, where a large and constant current would be indispensable to quickly charge the battery.<sup>150, 151</sup>

#### 5.3.4 Electrochemical performance of lithium-sulfur batteries

As is known that the free polysulfide species are generally electrochemically activity. Therefore, to verify whether the polysulfides anchored on the VPP membrane is activity, we firstly designed and assembled a cell with a  $S_6^{2-}$ -VPP membrane as separator and a carbon paper without S as cathode and tested its electrochemical performance (Figure 5.12a). From the Figures 5.12b and 5.12c, we can see that no obvious characteristic charging and discharging plateaus of Li-S cell can be observed even after a long-term cycling upon 200 cycles, demonstrating that the polysulfides anchored by VPP were inactive and can't contribute any additional capacity.

The electrochemical performance was evaluated by Li-S coin cells with various separators. The inner structure of the Li-S coin cell is presented as Figure 5.13. The cathode was prepared by coating a mixed slurry of RGO@S (sulfur content: 87 wt%), carbon black and PVDF with mass ratio of 8:1:1 on the aluminum foil. The sulfur loading in every cathode is about  $1 \text{ mg cm}^{-2}$ . The anodes were prepared by directly pressing Li

metal foils on stainless steel foils. The electrolyte was 1 M LiTFSI in DOL/DME (1:1) with 2 wt% LiNO<sub>3</sub>. The separator is commercial Celgard 2400 (PP) or the as-prepared flexible S<sub>6</sub><sup>2-</sup>-VPP membranes. It should be noted that the S<sub>6</sub><sup>2-</sup>-VOPO<sub>4</sub> coating layer is faced to sulfur cathode. Reference Li-S cells with pure PP membranes and untreated a pure PP membrane as separator were also assembled for comparison.

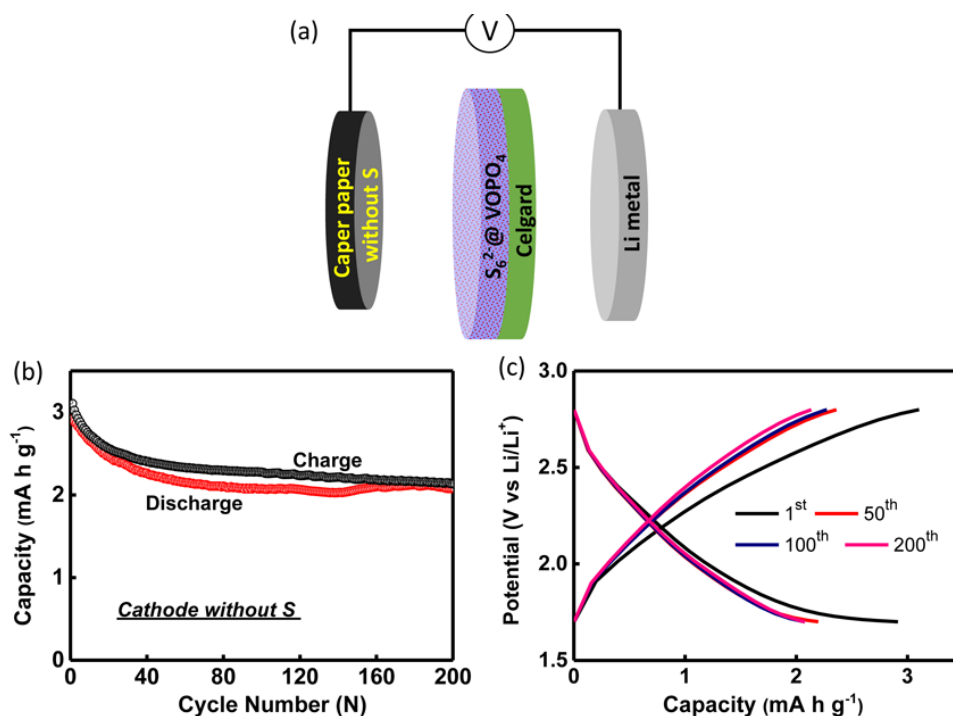


Figure 5.12 (a) The inner structure, (b) cycling performance, and (c) corresponding charge/discharge curves at 0.1 C of the cell with a S<sub>6</sub><sup>2-</sup>-VPP membrane as separator and a carbon paper without S as cathode.

The rate performance assessed at different current densities is shown in Figure 5.14a. The initial capacity at 0.1 C of the Li-S cell with a PP separator is 1259 mA h g<sup>-1</sup>, while the discharge capacity was decreased rapidly as the current density increased. When the current density increased to 5 C, the PP-cell maintains a very low reversible capacity of 122 mA h g<sup>-1</sup>. After introducing a S<sub>6</sub><sup>2-</sup>-VPP membrane to build a “polysulfides-phobic” interface between sulfur cathode and routine PP separator, the Li-S cell exhibits

a higher initial discharge capacity of  $1310 \text{ mA h g}^{-1}$ , about 78.2% of the theoretical value, indicating a high utilization of sulfur. With the increase of the discharge rate, the Li-S cell still can deliver high capacities of 1199, 1082, 967, 868, 728, 640 and  $415 \text{ mA h g}^{-1}$  at the current densities of 0.2, 0.5, 1, 2, 3, 4 and 5 C, respectively. In particular, when the current density suddenly decreased from 5 C to 0.1 C, an ultra-high discharge capacity of  $1188 \text{ mA h g}^{-1}$  was recovered, demonstrating a good reversibility of the cell after introducing a “polysulfides-phobic” interface.

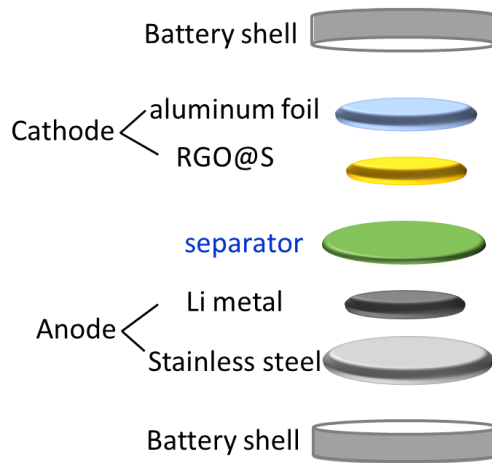


Figure 5.13 The inner structure of the assembled Li-S coin cell.

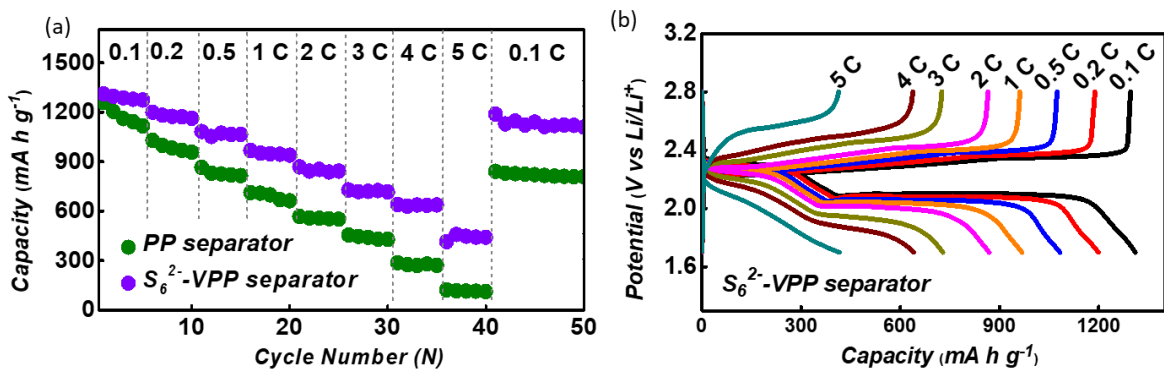


Figure 5.14 (a) The rate performance of Li-S cells with different separators. (b) Voltage profiles of Li-S cell with a  $\text{S}_6^{2-}$ -VPP separator.

The corresponding voltage profiles are shown in Figure 5.14b. All the voltage profiles at various current densities exhibit two typical discharge plateaus. The plateau at high potential around 2.3 V was attributed to the reduction of element S to long-chain polysulfides ( $\text{Li}_2\text{S}_x$ ,  $4 \leq x \leq 8$ ), involving a fast kinetic process, while the plateau at relative lower potential nearly 2.1 V was contributed by the further reduction of generated long-chain polysulfides to insoluble  $\text{Li}_2\text{S}_2/\text{Li}_2\text{S}$ , referring to a slow kinetic process. During the subsequent charging process, the final discharging products  $\text{Li}_2\text{S}_2/\text{Li}_2\text{S}$  were reconverted to elemental S through formation of polysulfides intermediates, obtaining a complete cycle. In especial, when the current density reached up to an ultra-high rate of 3 C, stable and flat charging/discharging plateaus still can be observed from the voltage profiles, further demonstrating that the incorporation of a  $\text{S}_6^{2-}$ -VPP separator facilitated a good rate performance. The excellent rate performance was basically attributed to following factors: (1) the good electrolyte accessibility and the thin thickness of  $\text{VOPO}_4$  layer facilitate free ion transport; (2) the effective restriction of polysulfides diffusion significantly improved the reutilization of active materials; (3) the enhanced  $\text{Li}^+$  transference number was beneficial for a higher attainable charge state at high rates, where a large and constant current is indispensable to quickly charge the battery.<sup>150, 151</sup>

The cycling performance of Li-S cells with various separators are presented in Figure 5.15a, which were tested by galvanostatic charge/discharge at a low current density of 0.2 C within a potential range of 1.7~2.8 V versus  $\text{Li}/\text{Li}^+$ . It can be observed that the discharge capacity of the cell with a routine PP separator decayed rapidly under a continuous charging/discharging process, especially in the first few cycles, suffering from the adverse polysulfides shuttle. After 300 cycles, its capacity decreased to  $310 \text{ mA h g}^{-1}$ , exhibiting a very low capacity retention of 28.1%. After introducing a  $\text{S}_6^{2-}$ -VPP separator, the cell realized a high reversible capacity of  $840 \text{ mA h g}^{-1}$  after 300 cycles,

corresponding to 75.3% capacity retention with a low capacity decay rate of 0.082%. The excellent cycling performance of the Li-S cell was attributed to the effective inhibition of polysulfides migration by the polysulfide-phobic  $S_6^{2-}$ -VPP separator via coulomb repulsion. The detailed electrochemical behaviour of the cell with a  $S_6^{2-}$ -VPP separator was further investigated by CV (Figure 5.15b). Two characteristic peaks appearing at cathodic scan were ascribed to the two reduction processes of elemental sulfur while the peak at the subsequent anodic scan was assigned to formation of  $S_8$ , which are consistent with the charging/discharging curves. The nearly overlapped peak position of the selected curves at various cycles further prove the high reversibility and good stability of the Li-S cell endowed by  $S_6^{2-}$ -VPP separator.

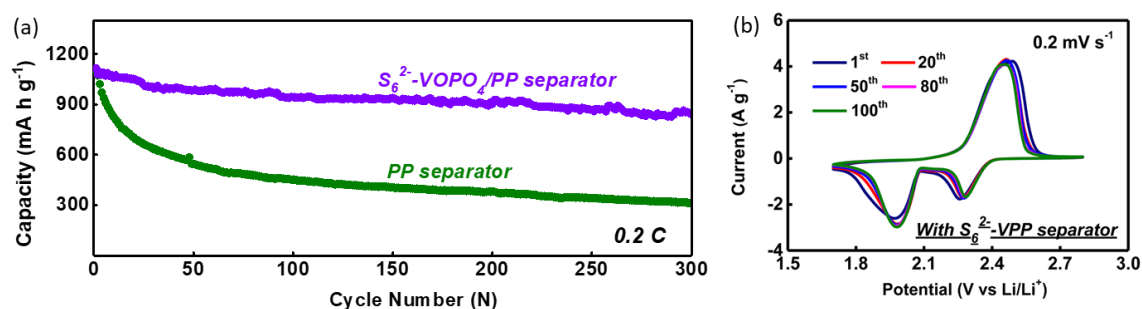


Figure 5.15 (a) Comparison of cycling performance of Li-S cells with different separators. (b) Selective CV curves of Li-S cells with a  $S_6^{2-}$ -VPP separator at  $0.2 \text{ mV s}^{-1}$ .

The PXRD of  $S_6^{2-}$ -VPP membranes after cycling was also performed to verify the structure stability of  $S_6^{2-}$ -VOPO<sub>4</sub> in a Li-S cell. From the PXRD patterns shown in Figure 5.16, we can see that the VOPO<sub>4</sub> sheets still maintain a typical layered structure after cycling. In addition, the FE-SEM image presented inset of Figure 5.16 shows dense distribution of VOPO<sub>4</sub> sheets, further confirming a good stability of the  $S_6^{2-}$ -VPP separators.

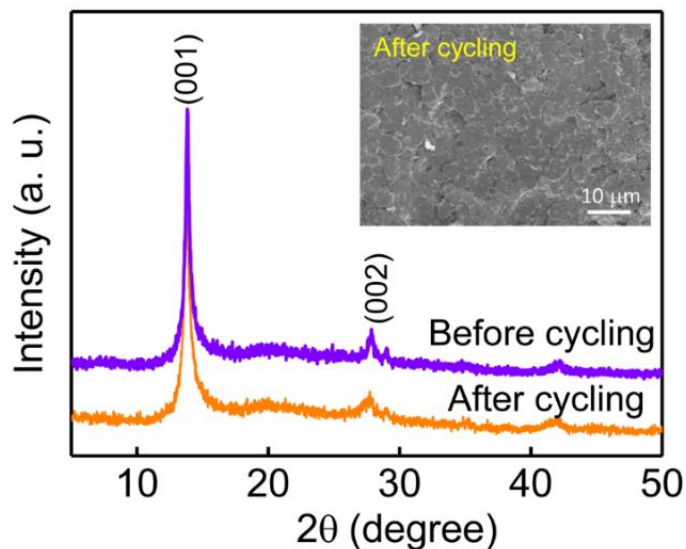


Figure 5.16 PXRD patterns of  $S_6^{2-}$ -VPP separator before and after cycling. Inset presents the FE-SEM image of  $S_6^{2-}$ -VPP separator after cycling.

## 5.4 Summary

In summary, we proposed and developed a novel polysulfide-phobic strategy to restrain polysulfides shuttle in Li-S batteries. The  $VOPO_4$  sheets with adequate active sites were used to immobilize the polysulfides via formation of V-S bonds. Owing to the electronegativity of polysulfides, the  $VOPO_4$  sheets anchored with polysulfides can evolve into a polysulfide-phobic surface driven by Coulomb repulsion. This adsorption-induced “self-defence” mechanism was convincingly proved by the evidences from the time/space-resolved operando Raman observation. In addition, the enhanced electrochemical performance of Li-S batteries with polysulfides-treated separators proved the reliability and practicability of the polysulfide-phobic strategy. Fundamental understanding of the interaction between the soluble polysulfide anions and anchored polysulfides provides new insights and opportunities to construct high quality separators for advanced Li-S batteries.

# Chapter 6. Fabricating a tri-layer separator to restrain shuttle effect and inhibit lithium dendrites growth

## 6.1 Introduction

In chapter 5, we have built a “polysulfide-phobic” surface by anchoring the polysulfides on the polar materials. The collected Raman information also evidently demonstrated that the anchored polysulfides have strong repulsion effect on the approaching polysulfides. However, despite constructing a “polysulfide-phobic” surface can effectively inhibit the polysulfides shuttle, the fatal effects aroused by uncontrolled growth of lithium dendrites still seriously affects the durability and security of Li-S batteries (Figure 6.1a). In this case, a multi-functional separator that can simultaneously suppress the polysulfides shuttle and lithium dendrites growth is still needed to be further developed.

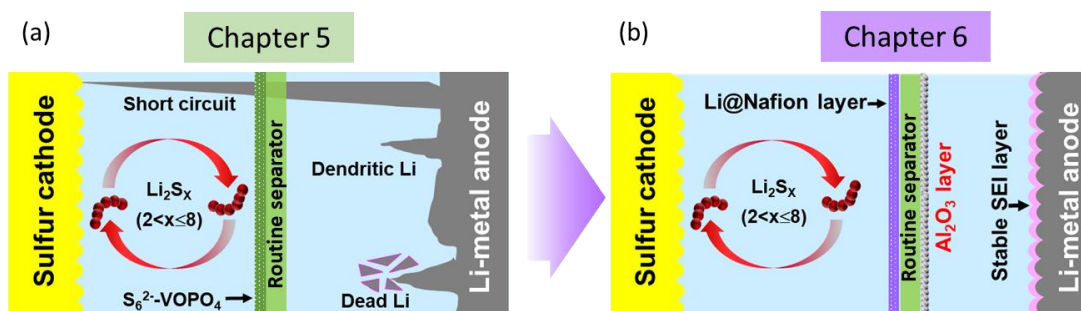


Figure 6.1 (a) Building a “polysulfide-phobic” surface to prevent the diffusion of polysulfides in chapter 5. (b) Building a “polysulfide-phobic” surface by Li@Nafion and introducing an  $\text{Al}_2\text{O}_3$  layer to simultaneously restrain the polysulfides shuttle and lithium dendrites growth in chapter 6.

In accordance with this line of thinking, it can be concluded that an ideal separator for Li-S batteries should have the attributes as follows<sup>10, 11</sup>: (1) electronic insulation to

avoid internal short; (2) good chemical and electrochemical stability that can withstand the strong oxidizing and reducing circumstances in the batteries; (3) functional layers to inhibit the polysulfides shuttle and lithium dendrites growth; (4) good electrolyte wettability to facilitate the adsorption of liquid electrolyte; (5) porous structure with appropriate porosity to retain adequate electrolyte for achieving low internal resistance as well as high ionic conductivity; (6) robust mechanical strength for improving the practicability and security of batteries.

To meet these requirements, here we designed a triple-layered membrane as multifunctional separator for Li-S batteries. The triple-layered separator was fabricated by respectively coating a thin lithiated Nafion (Li@Nafion) layer and an Al<sub>2</sub>O<sub>3</sub> nanoparticles layer on the two sides of a routine polymer membrane (polypropylene/polyethylene/ polypropylene, PEP) (Figure 6.1b). The thin Li@Nafion towards sulfur cathode acts as an ionic shield that can effectively restrain the polysulfides migration but facilitate the Li ions hopping via Coulombic interactions. It should be noted that using the Li@Nafion instead of S<sub>6</sub><sup>2-</sup>-VOPO<sub>4</sub> to construct “polysulfide-phobic” surface is because of two factors: on one hand, Li@Nafion composed of tetrafluoroethylene and perfluoro-vinyl-ether with sulfonate-ended perfluoroalkyl ether groups, which make it allow the hopping of positively charged ions (Li<sup>+</sup>) but reject the diffusion of negatively charged ions (polysulfides); on the other hand, the pre-treatment of S<sub>6</sub><sup>2-</sup>-VOPO<sub>4</sub> needs a lot of steps, while a “polysulfide-phobic” surface built by Li@Nafion just needs directly drop the Li@Nafion solution on the PEP substrate, thus greatly cutting down the time costs of fabrication. With respect of the layer composed of Al<sub>2</sub>O<sub>3</sub> nanoparticles, their porous structure with a narrow pore size distribution is beneficial to control the uniformity of Li ions plating, suppressing the growth of lithium dendrites.<sup>152, 153</sup> As a result, the Li-S batteries cooperating with a Li@Nafion/PEP/Al<sub>2</sub>O<sub>3</sub>

(LNPA) separator achieved high capacity, excellent rate performance as well as remarkable cyclic stability.

## 6.2 Experiment and characterization

### 6.2.1 Chemicals and materials

Nafion 117 solution (~5% in a mixture of lower aliphatic alcohols and water) was from Sigma-Aldrich. Aluminium oxide ( $\text{Al}_2\text{O}_3$ ), sulfur ( $\text{S}_8$ ), and 1, 3-dioxolane (DOL, >99.9%) were purchased from Tokyo Chemical Industry Co., Ltd. 1,2 dimethoxymethane (DME, >99.9%) were obtained from FUJIFILM Wako Pure Chemical Corporation. lithium sulfide ( $\text{Li}_2\text{S}$ , 99.9% purity), lithium bis(trifluoromethanesulfonyl) imide (LiTFSI) and lithium nitrate ( $\text{LiNO}_3$ ) were purchased from Sigma-Aldrich. Polypropylene/polyethylene/polypropylene (PEP)/ $\text{Al}_2\text{O}_3$  membranes were obtained from Liaoyuan Hongtu LIBS Technology CO., LTD. Carbon paper was obtained from the Chemours Company.

### 6.2.2 Synthesis of $\text{Li}_2\text{S}_6$ in DOL/DME

The detailed preparation process of  $\text{Li}_2\text{S}_6$  DOL/DME solution has been described in section 5.2.2.

### 6.2.3 Fabrication of Li@Nafion/PEP/ $\text{Al}_2\text{O}_3$ membranes

Nafion 117 solution (~5% in a mixture of lower aliphatic alcohols and water) was firstly lithiated and neutralized by 0.5 M LiOH to pH~7. Then the lithiated Nafion (Li@Nafion) was directly dripped on the PEP surface of PEP/ $\text{Al}_2\text{O}_3$  membrane. The Li@Nafion liquid drops can spread along the surface of PEP substrate to form a uniform layer. The coating amounts of Li@Nafion layer were adjusted to 0.3, 1.0, and 2.9  $\text{mg cm}^{-2}$ . For comparison, the Li@Nafion/PEP (with Li@Nafion coating amount of 1.0  $\text{mg cm}^{-2}$ )

cm<sup>-2</sup>) membranes were also fabricated. The Li@Nafion/PEP, PEP/Al<sub>2</sub>O<sub>3</sub> and Li@Nafion/PEP/Al<sub>2</sub>O<sub>3</sub> membranes in this work are abbreviated as LNP, PA and LNPA, respectively.

#### 6.2.4 Li//Li symmetric cells assembly

All Li//Li symmetric cells were assembled under the protection of Argon. Standard 2032 coin cells were used to evaluate the Li plating/stripping performance of Li//Li symmetric batteries. The electrodes were prepared by directly pressing Li metal foils with diameter of 12 mm on stainless steel foils. The electrolyte was prepared by dissolving 1 M LiTFSI and 2 wt% LiNO<sub>3</sub> in a mixture of DOL and DME (1:1 by volume). The addition amount of electrolyte in every cell was about 50  $\mu$ L. The PEP, PEP/Al<sub>2</sub>O<sub>3</sub> (PA), Li@Nafion/PEP (LNP), and Li@Nafion/PEP/Al<sub>2</sub>O<sub>3</sub> (LNPA) membranes with diameter of 16 mm were used as separators.

#### 6.2.5 Lithium-sulfur cells assembly

The Li-S coin cells were assembled in an Argon filled glove box. The cathode was prepared by coating a mixed slurry of RGO@S and PVDF with a mass ratio of 9:1 on the carbon paper. The anodes were prepared via directly pressing Li metal foils on stainless steel foils. The electrolyte was 1 M LiTFSI with 2 wt% LiNO<sub>3</sub> in DOL/DME (1:1). The addition amount of electrolyte in every cell was about 30  $\mu$ L. The PEP, PEP/Al<sub>2</sub>O<sub>3</sub> (PA), Li@Nafion/PEP (LNP), and Li@Nafion/PEP/Al<sub>2</sub>O<sub>3</sub> (LNPA) membranes with diameter of 16 mm were used as separators. It should be noted that the Li@Nafion layer was faced to cathode side and the Al<sub>2</sub>O<sub>3</sub> layer was towards the lithium metal anodes. Standard 2032 coin cells were used to evaluate the electrochemical performance of Li-S batteries.

## 6.2.6 Characterization and electrochemical measurements

LEO Gemini Supra 35 system and SU8020 field-emission scanning electron microscopy (FE-SEM) was used to reveal the morphologies of the samples. The test method of ionic conductivity was shown as in 5.2.8. The measurement and calculation of  $\text{Li}^+$  transference was shown in 5.2.9. The corresponding separator was changed to PEP, PEP/ $\text{Al}_2\text{O}_3$  (PA), Li@Nafion/PEP (LNP), or Li@Nafion/PEP/ $\text{Al}_2\text{O}_3$  (LNPA) membranes. The electrochemical measurements can be referenced 5.2.10.

## 6.3 Results and discussions

### 6.3.1 Properties of Li@Nafion/PEP/ $\text{Al}_2\text{O}_3$ membrane

The morphologies of each component were revealed by FE-SEM. It can be seen that the commercial PEP membrane presents a flat surface with three-dimensional channels throughout whole membrane (Figure 6.2a), which are in favour of rapid transportation of lithium ions but hardly reserve the polysulfide ions. After coating a thin Li@Nafion layer with amount of  $1 \text{ mg cm}^{-2}$ , the channels in the PEP membrane completely covered (Figure 6.2b), which is beneficial to block the diffusion of dissolved polysulfides. On another side of the PEP membrane, an  $\text{Al}_2\text{O}_3$  layer was formed by 50 nm  $\text{Al}_2\text{O}_3$  particles (Figure 6.2c). The total thickness of the LNPA membrane is about 15  $\mu\text{m}$ , and the thicknesses of the thin Li@Nafion layer and  $\text{Al}_2\text{O}_3$  layer are about 1 and 4  $\mu\text{m}$ , respectively (Figure 6.2d). It is noteworthy that the loading amount of Li@Nafion plays an important role in the electrochemical performance of Li-S batteries. When the loading amount of Li@Nafion is too low ( $0.3 \text{ mg cm}^{-2}$ ), it cannot form a complete film to cover the channels throughout the PEP membrane (Figure 6.2e). However, a high Li@Nafion loading ( $2.9 \text{ mg cm}^{-2}$ ) will lead to a high transfer resistance and low ion conductivity (Figure 6.2f).

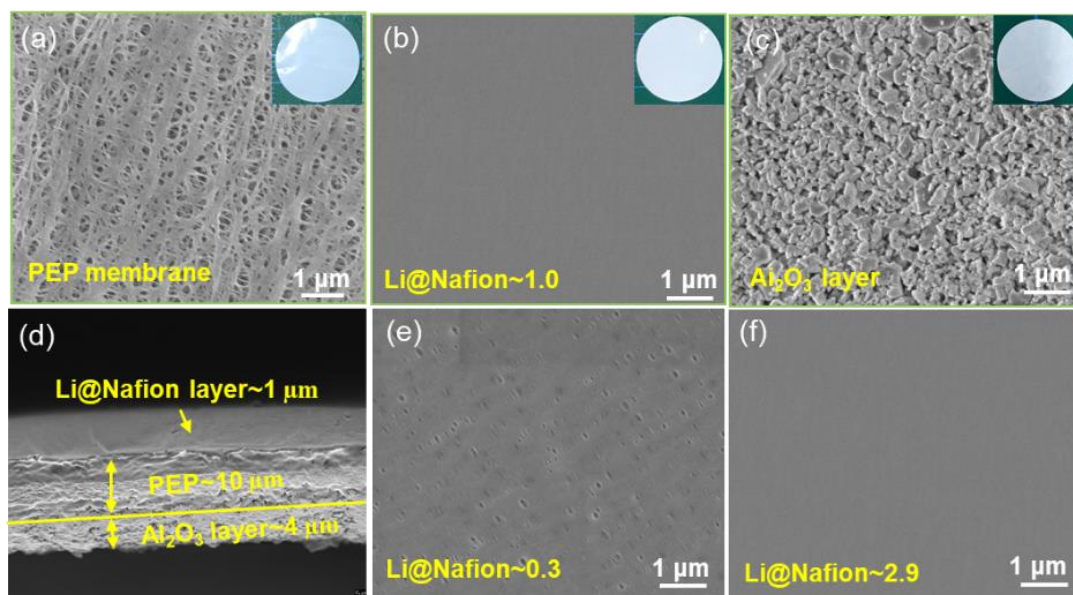


Figure 6.2 SEM images of (a) PEP membrane, (b) Li@Nafion layer with loading of  $1.0 \text{ mg cm}^{-2}$ , and (c)  $\text{Al}_2\text{O}_3$  layer. (d) Cross-section SEM image of Li@Nafion/PEP/ $\text{Al}_2\text{O}_3$  with Li@Nafion loading of  $1.0 \text{ mg cm}^{-2}$ . SEM images of Li@Nafion layer with loading of (e)  $0.3$  and (f)  $2.9 \text{ mg cm}^{-2}$ .

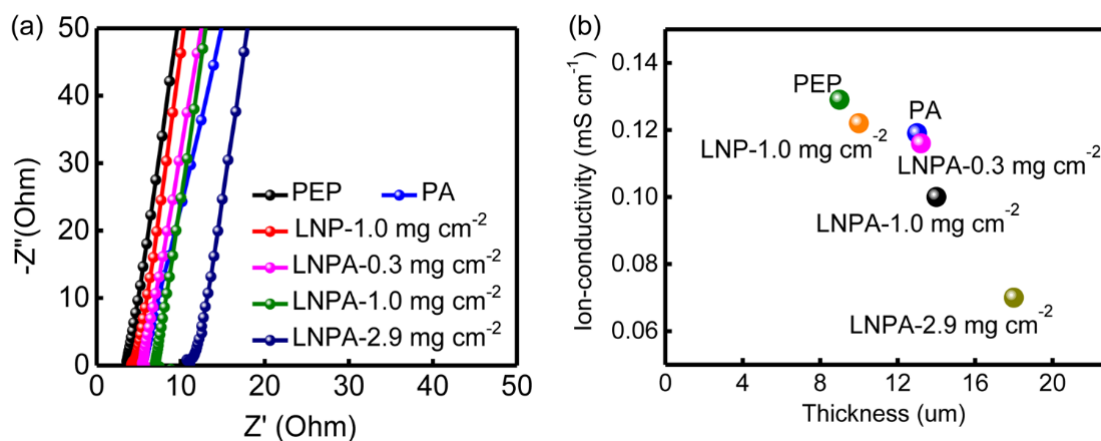


Figure 6.3 (a) Electrochemical impedance spectra and (b) corresponding ion conductivities of various separators.

The ion conductivities of various separators were carried out by using stainless steel/stainless steel symmetric coin cells. As shown in Figure 6.3, the pure PEP separator exhibits an ion conductivity of  $0.129 \text{ mS cm}^{-1}$ . After coating a Li@Nafion layer ( $1.0 \text{ mg}$

cm<sup>-2</sup>) and an Al<sub>2</sub>O<sub>3</sub> layer respectively, the ion conductivities slightly decreased to 0.122 and 0.119 mS cm<sup>-1</sup>. When simultaneously coated the Li@Nafion layer and the Al<sub>2</sub>O<sub>3</sub> layer on the two sides of PEP membrane, the ion conductivities for the tri-layer separator with Li@Nafion loading of 0.3 and 1.0 mg cm<sup>-2</sup> are 0.116 and 0.105 mS cm<sup>-1</sup>, suggesting to introduce a Al<sub>2</sub>O<sub>3</sub> layer and a Li@Nafion layer with appropriate thickness almost have no influence on the transport of lithium ions. While when the Li@Nafion loading increased to 2.9 mg cm<sup>-2</sup>, the ion conductivity of the LNPA separator decreased to 0.699 mg cm<sup>-2</sup>, indicating that the too high Li@Nafion loading would affect the lithium ion diffusion. The Li@Nafion loading in the following study is 1.0 mg cm<sup>-2</sup>.

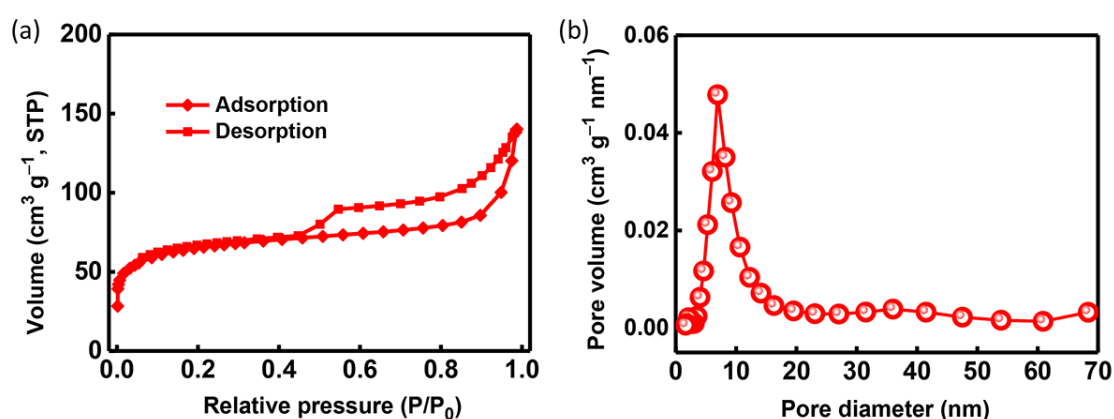


Figure 6.4 (a) N<sub>2</sub> adsorption/desorption isotherms and (b) corresponding pore size distributions of Al<sub>2</sub>O<sub>3</sub> layer.

The porous structure of Al<sub>2</sub>O<sub>3</sub> composite layer was investigated by N<sub>2</sub> adsorption/desorption test (Figure 6.4). The obtained isotherm belongs to type IV, revealing the mesoporous properties of the Al<sub>2</sub>O<sub>3</sub>. The specific surface area of Al<sub>2</sub>O<sub>3</sub> composite layer was determined to be 279 m<sup>2</sup> g<sup>-1</sup>. The pore-size distribution curve shows that the composite layer possesses a narrow pore size distribution located at  $\approx$ 8 nm, which is not only able to store a large amount of liquid electrolyte, but also beneficial for aiding to form homogeneous Li-ion fluxes, achieving stable electrodeposition of lithium.

Moreover, due to the porous structure and hydrophilic of  $\text{Al}_2\text{O}_3$  particles, the LNPA exhibits favourable electrolyte wettability (Figure 6.5), which is conducive to obtain a low internal resistance to achieve superior battery performance.<sup>154</sup>

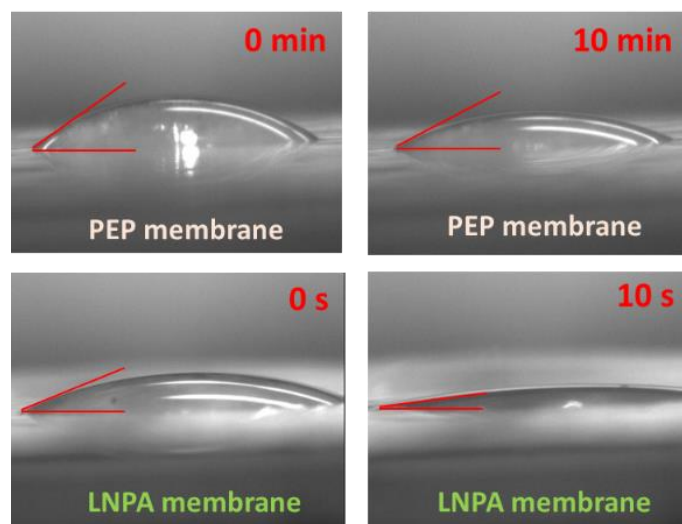


Figure 6.5 The optical photographs of various separators with the liquid electrolyte after different time.

### 6.3.2 Ionic selectivity of $\text{Li}@$ Nafion/PEP/ $\text{Al}_2\text{O}_3$ membranes

Visualized V-type glass device was designed and assembled to evaluate the blocking effect of each separator on the polysulfides diffusion (Figure 6.6). The inside of the left chamber is DOL/DME solvent with  $\text{Li}_2\text{S}_6$  while the inside of the right chamber is the pure solvent without  $\text{Li}_2\text{S}_6$ . The two chambers were separated by different separators. In the V-type device with a pristine PEP separator, it can be seen that the red brown high-order polysulfides gradually passed through the separator from left chamber to right chamber and reached a high level after 10 h, indicating that the pure PEP separator hardly prevent the diffusion of polysulfides. To the contrary, no obvious diffusion phenomenon of polysulfides was observed from the V-type device with a LNPA separator even after 48 h rest, proving that the LNPA separator can effectively inhibit the

polysulfides shuttle. To understand the main functional components of the LNPA in blocking polysulfides, the V-type glass devices with LNP and PA separators were also assembled, respectively. We can see that although an  $\text{Al}_2\text{O}_3$  layer can postpone the diffusion of polysulfides, it cannot fully reserve the polysulfides in the left chamber. For the PEP membrane with a thin Li@Nafion layer, it can effectively restrain the transfer of polysulfides, demonstrating that the Li@Nafion layer on the LNPA membrane play the crucial role in blocking the polysulfides shuttle.

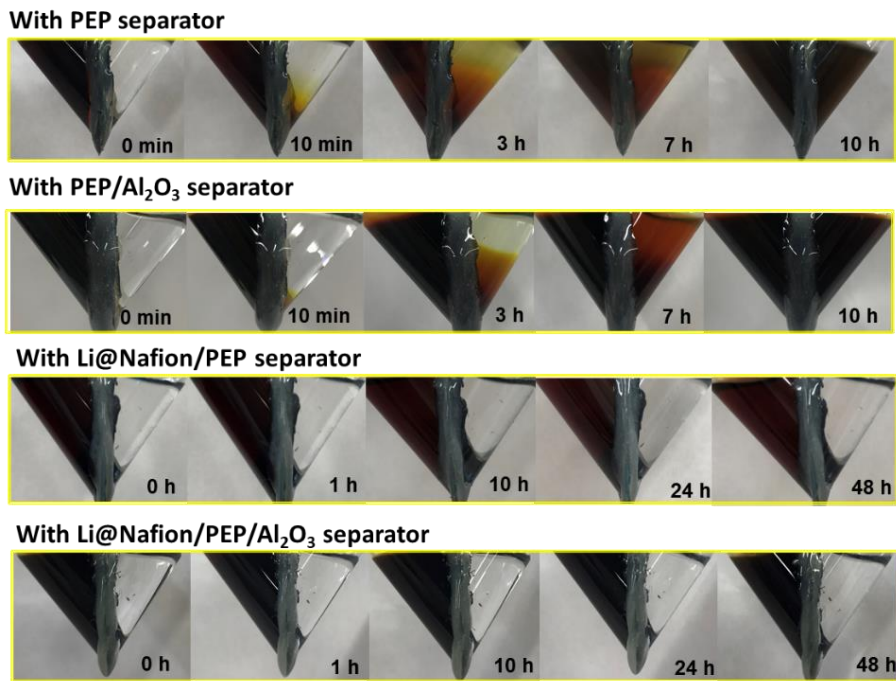


Figure 6.6 The visualized V-type glass devices with various separators. The insides of the left and right chambers are DOL/DME with and without  $\text{Li}_2\text{S}_6$ , respectively.

The lithium ions transference number ( $t_{\text{Li}^+}$ ) associated with 1 M LiTFSI in DOL/DME was further measured to verify the ionic selectivity of LNPA separator. As shown in Figure 6.7, the  $t_{\text{Li}^+}$  of LNPA/LiTFSI liquid electrolyte system was calculated to be 0.91, which is quite higher than that of a PEP/LiTFSI DME/DOL liquid electrolyte system (0.3~0.5),<sup>155-157</sup> indicating that the strong repulsion effect

of Li@Nafion layer on the negatively charged species. Such a high Li<sup>+</sup> transference number is in favour of a higher attainable charge state at high rate, where a large and constant current would be indispensable to quickly charge the battery.<sup>150, 151</sup>

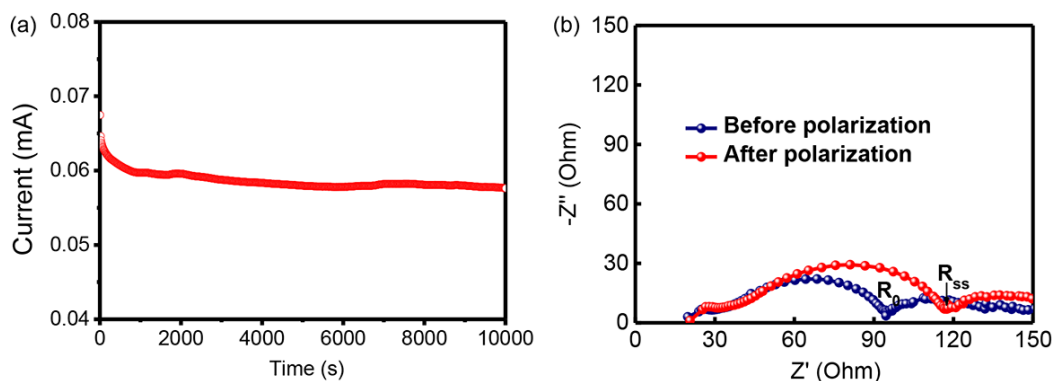


Figure 6.7 The characteristic of Li<sup>+</sup> transference number. (a) The potentiostatic polarization curve of Li-S cell with a LNPA separator. (b) The electrochemical impedance spectra before and after polarization.

### 6.3.3 Lithium plating/stripping stability

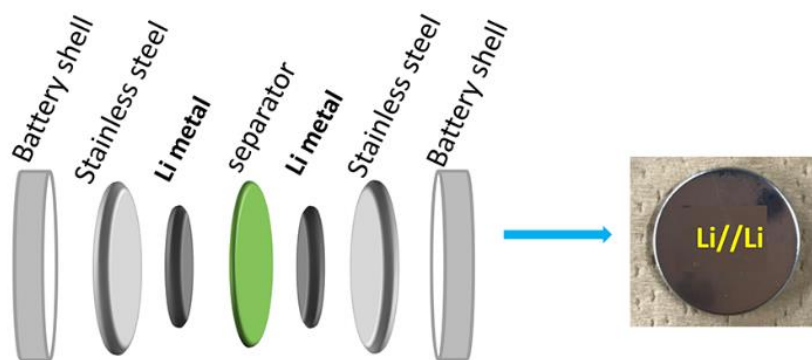


Figure 6.8 Schematic diagram of the inner structure of Li//Li symmetric cell.

The effect of various separators on the Li metal stability during Li plating/stripping was investigated by Li//Li symmetric cells (Figure 6.8). Operated at a current density of 2 mA cm<sup>-2</sup> with corresponding areal capacity of 1 mA h cm<sup>-2</sup>, the PEP-cell revealed a low overpotential about 40 mV at the first few cycles (Figure 6.9).

However, after a continuously stable Li plating/tripping process last for 150 h, the overpotential gradually increased as the cycle time increased, and reached up to 340 mV after 600 h cycle (Figure 6.9a), which was nearly nine-fold increase compared to initial value. The severe polarization was mainly caused by the porous and uneven structured lithium dendrites, which prolong the transfer pathway of electrolyte ions.<sup>158</sup> In addition, the overgrown lithium dendrites also enlarged the reactive surface area of the possible parasitic reactions between lithium metal and electrolyte, and the formed solid electrolyte interface (SEI) layer would wrap the fresh lithium metal. In this way the wrapped lithium metal may out of approachability to current collectors, resulting in electrochemically inert dead Li and premature failure of the electrodes.<sup>57</sup> After introducing a Li@Nafion layer on the PEP membrane, the period of stable Li plating/tripping process can be prolonged to about 650 h (Figure 6.9b). Using a ceramic layer composing of porous Al<sub>2</sub>O<sub>3</sub> nanoparticles instead of Li@Nafion layer, a stable Li plating/tripping process with a low average overpotential (~49 mV) was achieved (Figure 6.9c). The effective inhibition of lithium dendrites growth is attributed to the uniform porosity of the Al<sub>2</sub>O<sub>3</sub> nanoparticles, which can aid in regulating homogeneous Li ions flux, realizing a stable Li plating/stripping process.<sup>152, 153</sup> As a result, integrating both Li@Nafion layer and Al<sub>2</sub>O<sub>3</sub> layer on the PEP membrane, the LNPA-cell with a separator maintain a stable overpotential even after an ultralong duration of cycle over 1000 h (Figure 6.9d).

Furthermore, the potential of LNPA for practical applications was further evaluated at a high current density of 5 mA cm<sup>-2</sup> with areal capacity of 2.5 mA h cm<sup>-2</sup>. As shown in Figure 6.9e, a slight fluctuation was observed from the initial several cycles, generally because the symmetric cell plated/stripped at such a high rate need an activation process. The overpotential gradually became stable and maintained at ~96 mV. No obvious short circuit occurred during such a long cycling

process of 1000 h, forcefully indicating the LNPA separator can effectively inhibit the growth of Li dendrites. The high efficiency Li metal anode has great potential to achieve high theoretical specific capacity and be employed in next-generation energy storage systems.

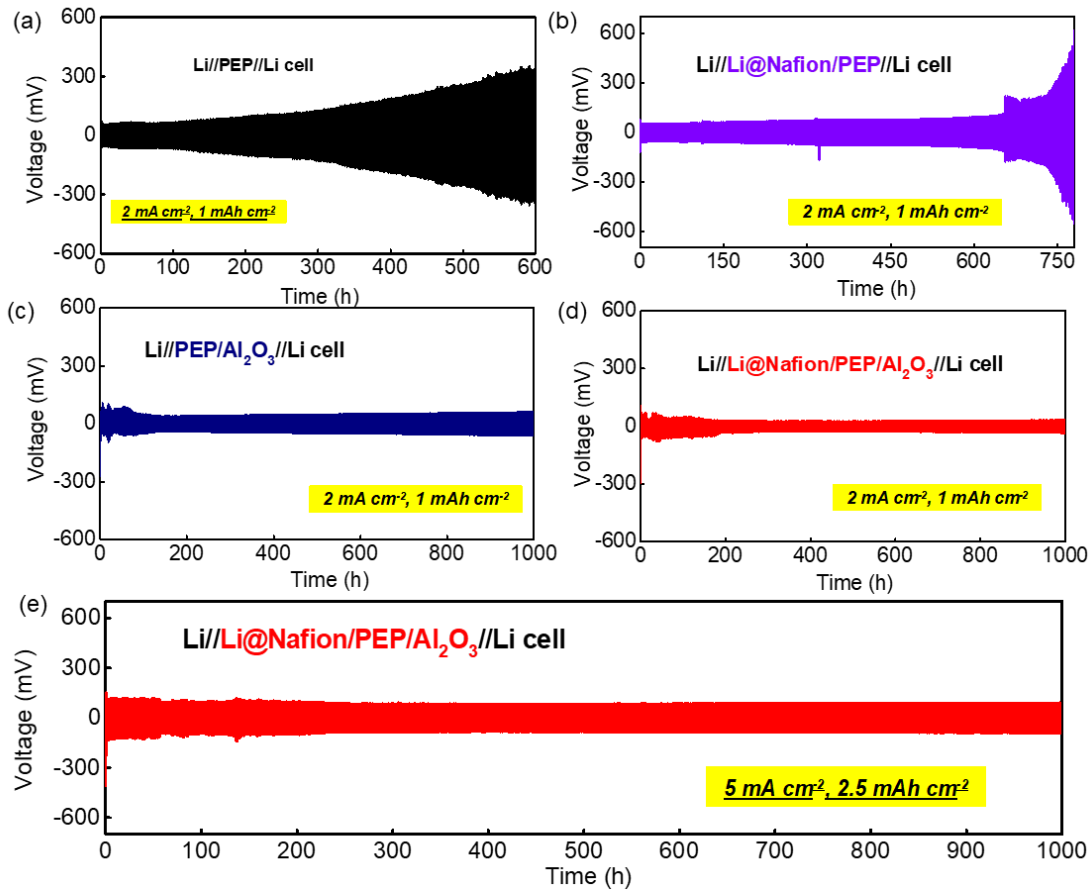


Figure 6.9 Li stripping/plating performance in Li//Li symmetric cells at  $2 \text{ mA cm}^{-2}$  ( $1 \text{ mA h cm}^{-2}$ ) with different separators. (a) PEP, (b) Li@Nafion/PEP, (c) PEP/ $\text{Al}_2\text{O}_3$ , and (d) Li@Nafion/PEP/ $\text{Al}_2\text{O}_3$ . (e) Li plating/stripping behaviour of cell with a Li@Nafion/PEP/ $\text{Al}_2\text{O}_3$  separator at high current-density of  $5 \text{ mA cm}^{-2}$  ( $2.5 \text{ mA h cm}^{-2}$ ).

The Li//Li symmetric cells after cycling 1000 h at  $2 \text{ mA cm}^{-2}$  were detached to observe the status of Li electrodes. As shown in Figure 6.10a and 6.10c, it can be seen that the cycled Li metal electrodes from PEP-cell and LNP-cell display a rough surface

with numerous dendrites. The erosion of Li metal reached nearly 150  $\mu\text{m}$  (Figure 6.10b and 6.10d), implying that plenty of fresh Li was consumed by the undesirable side reaction between electrolyte and Li dendrites. On the contrary, the cycled Li metal electrodes detached from PA-cell and LNPA-cell show flat and compact surface with uniform and stable SEI layers (Figure 6.10e-h), further demonstrating that introducing a  $\text{Al}_2\text{O}_3$  layer onto the separator can facilitate a homogeneous electrodeposition of Li ions, which fundamentally inhibits the growth of lithium dendrites.

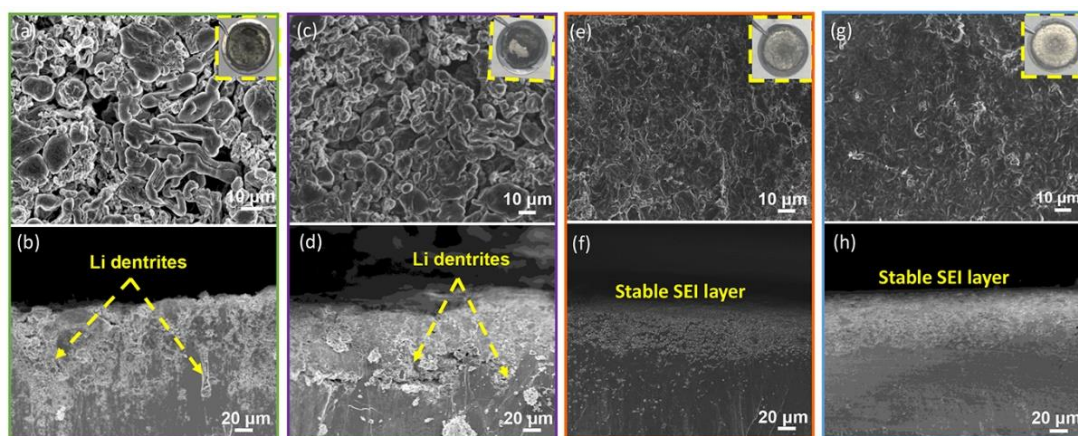


Figure 6.10 The cycled lithium metal electrodes from the cells with various separators: (a, b) PEP, (c, d) Li@Nafion/PEP, (e, f) PEP/ $\text{Al}_2\text{O}_3$ , and (g, h) Li@Nafion/PEP/ $\text{Al}_2\text{O}_3$ .

### 6.3.4 Electrochemical performance of lithium-sulfur batteries

The electrochemical performance was evaluated by Li-S coin cells with various separators. The cathode was prepared by coating a mixed slurry of RGO@S and PVDF with mass ratio of 9:1 on the carbon paper. The sulfur loading in every cathode is about  $1 \text{ mg cm}^{-2}$ . The anodes were prepared by directly pressing Li metal foils on stainless steel foils. It should be noted that the Li@Nafion layer and the  $\text{Al}_2\text{O}_3$  layer are respectively faced to sulfur cathode and lithium anode.

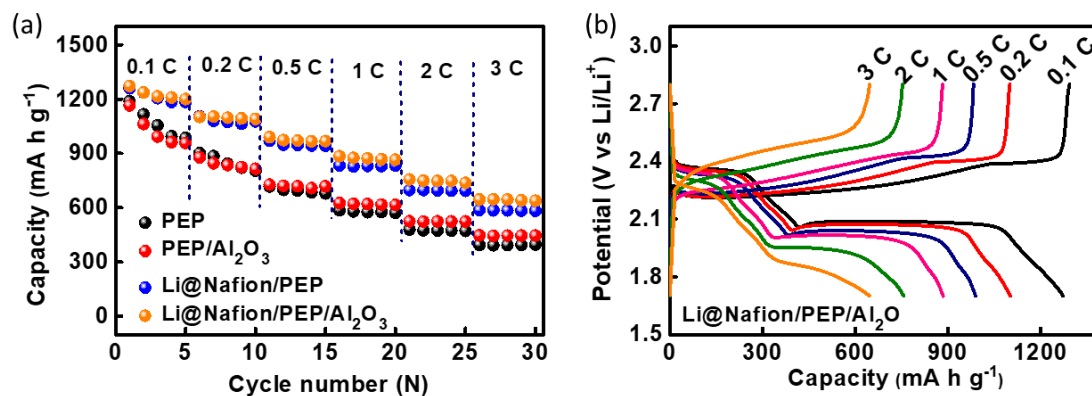


Figure 6.11 (a) The rate performance of Li-S cells with different separators. (b) Voltage profiles of Li-S cell with a Li@Nafion/PEP/Al<sub>2</sub>O<sub>3</sub> separator.

Galvanostatic charging/discharging at various rates from 0.1 C to 3 C were firstly performed to evaluate the rate performance (Figure 6.11a). The initial capacities of the cells with Li@Nafion/PEP and Li@Nafion/PEP/Al<sub>2</sub>O<sub>3</sub> separators (1259 and 1272 mA h g<sup>-1</sup>) are relatively higher than that of the cells with PEP and PEP/Al<sub>2</sub>O<sub>3</sub> separators (1187 and 1164 mA h g<sup>-1</sup>), indicating the restraint of polysulfides shuttle can effectively enhance the utilization of active materials. With the increase of the current density, the capacities of cells with PEP and PEP/Al<sub>2</sub>O<sub>3</sub> separators decreased rapidly, while the cell with Li@Nafion/PEP and Li@Nafion/PEP/Al<sub>2</sub>O<sub>3</sub> separators can still deliver high capacities of 587 and 645 mA h g<sup>-1</sup> even at 3 C. The charge/discharge profiles at various rates of the cell with Li@Nafion/PEP/Al<sub>2</sub>O<sub>3</sub> separator are shown in Figure 6.11b. All of them present two discharge plateaus, corresponding to two typical reduction stages that the conversion of elemental sulfur to long-chain polysulfide species and eventually to insoluble sulfide species (Li<sub>2</sub>S<sub>2</sub>/Li<sub>2</sub>S). The excellent rate performance of the cell with a Li@Nafion/PEP/Al<sub>2</sub>O<sub>3</sub> separator is mainly contributed by the following factors: (1) the good electrolyte wettability is favourable for absorbing and retaining a large amount of electrolyte to realize low internal resistance and high ionic conductivity;<sup>10</sup> (2) the high

Li<sup>+</sup> transference number is beneficial for a higher attainable state of charge at high rates, where a large and constant current is requisite to fast charge the battery;<sup>150, 151</sup> (3) the effective mitigation of polysulfides shuttle and Li dendrites growth significantly accelerate the reutilization of active materials.

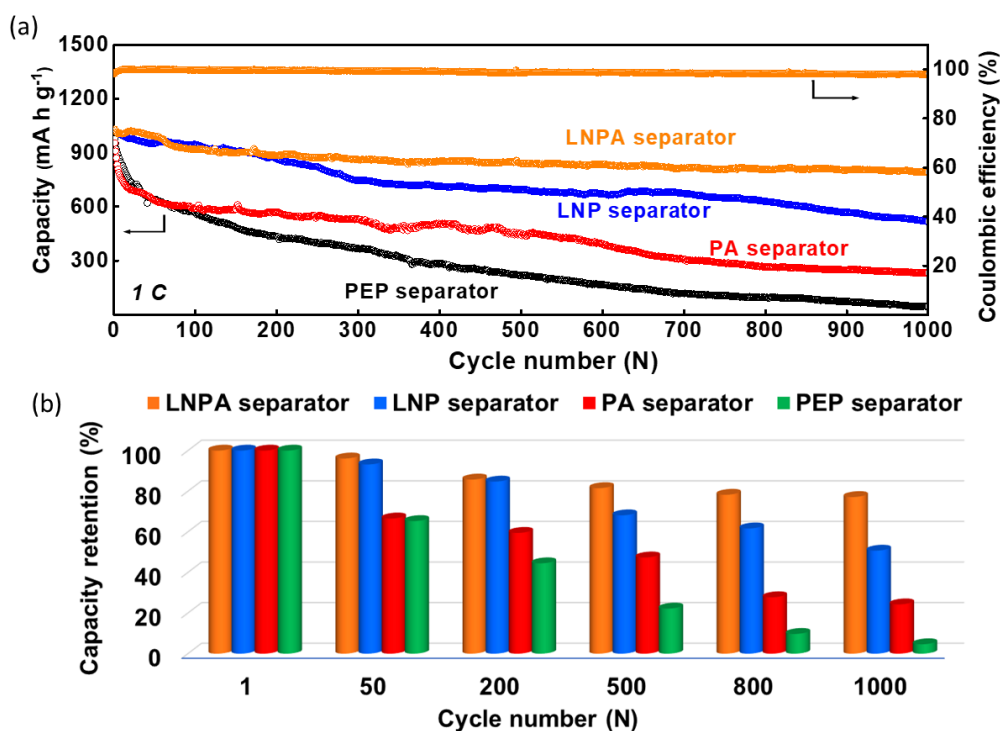


Figure 6.12 (a) The discharge capacities and (b) capacity retentions of the Li-S cells with various separators.

In order to further prove the availability of the LNPA separator for inhibiting the polysulfides shuttle and Li dendrites growth, long-term cycling performance of the batteries was evaluated at 1 C. As shown in Figure 6.12, the capacity of the cell with a pure PP separator decreased rapidly as the increase of the cycle number, especially in the first 200 cycles. After 1000 cycles, it can merely deliver a capacity of 45 mA h g<sup>-1</sup> with an ultralow capacity retention of 4.6%, which was caused by the adverse effects of polysulfides shuttle and uncontrolled growth of lithium dendrites. Introducing an Al<sub>2</sub>O<sub>3</sub>

layer on the pristine PEP separator, the capacity retention increased to 24.2%, indicating that the  $\text{Al}_2\text{O}_3$  layer also can mitigate the polysulfides shuttle via physical absorption. Using a Li@Nafion coating layer instead of the  $\text{Al}_2\text{O}_3$  layer, both the initial discharge capacity ( $1021 \text{ mA h g}^{-1}$ ) and the capacity retention (50.7%) obviously enhanced, implying that the shuttle effect is the main factor in causing a poor cycling performance in the case of low sulfur loading. When design a ternary separator simultaneously incorporating a Li@Nafion layer and an  $\text{Al}_2\text{O}_3$  layer on the two sides of PEP membrane, the cyclic stability of the Li-S cell greatly improved, achieving an ultrahigh capacity retention (77.2%) along with a low capacity decay rate (0.022% per cycle) after 1000 cycles. The significant enhancement in cycling performance of the cell with the LNPA separator can attributed to two respects: on the one hand, the remarkable suppression of the polysulfides shuttle via electrostatic repulsion of the Li@Nafion layer effectively store the active species within the cathode region to achieve high sulfur reutilization; on the other hand, the available inhibition of lithium dendrites growth by  $\text{Al}_2\text{O}_3$  layer prominently stabilize the lithium plating/stripping progress to prolong service life the lithium metal anode.

Additionally, in order to evaluate the feasibility of the LNPA separator in practical application, the sulfur loading was augmented to 4.8 and 7.6  $\text{mg cm}^{-2}$  (Figure 6.13). Excitingly, the cells were still able to deliver high initial capacities of  $1344 \text{ mA h g}^{-1}$  (4.8  $\text{mg cm}^{-2}$ ) and  $1322 \text{ mA h g}^{-1}$  (7.6  $\text{mg cm}^{-2}$ ) at 0.05 C, corresponding to high areal capacities of 6.4 and 10.0  $\text{mA h cm}^{-2}$ , respectively. After activation at 0.05 C, the cells with high sulfur loading were cycling at a low rate of 0.2 C. Both of them maintained considerable capacity retentions after long-term cycling. The pronounced cyclic performance of the Li-S cells illustrates the practicability and reliability of the ternary designed LNPA membrane as a multifunctional separator.

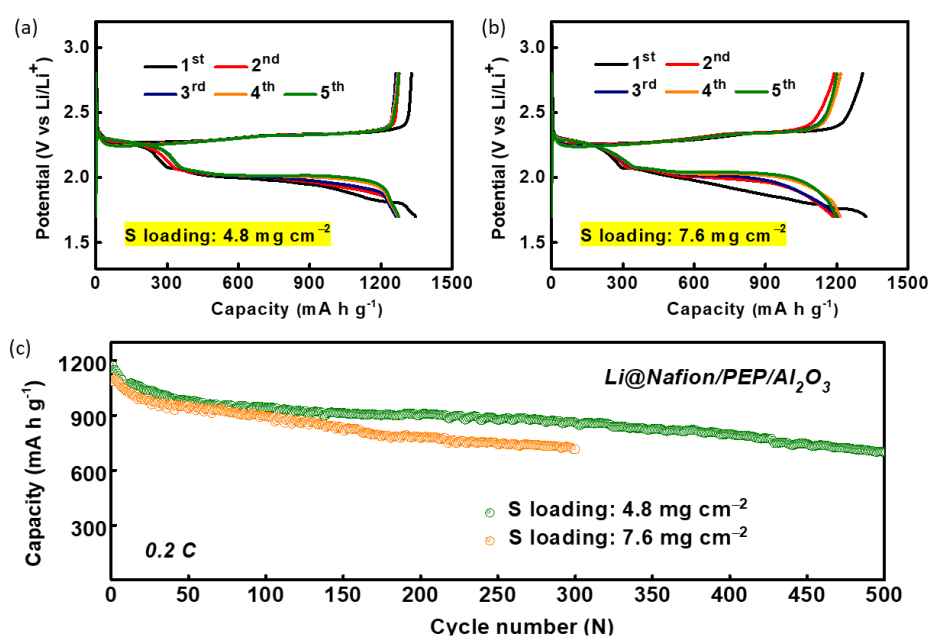


Figure 6. 13 The initial charge/discharge profiles of the Li-S cells with Li@Nafion/PEP /Al<sub>2</sub>O<sub>3</sub> separators with high sulfur loadings of (a) 4.8 and (b) 7.6 mg cm<sup>-2</sup> at 0.05 C. (c) The cycling performance of the cell with high sulfur loadings at 0.2 C.

## 6.4 Summary

In summary, we rationally constructed a ternary separator by integrating a Li@Nafion layer and an Al<sub>2</sub>O<sub>3</sub> nanoparticles layer on the two sides of PEP membrane for Li-S batteries. The Li@Nafion layer with negatively charged -SO<sub>3</sub><sup>-</sup> can effectively inhibit the polysulfides diffusion via Coulombic interactions, while the Al<sub>2</sub>O<sub>3</sub> layer with a narrow pore size window can acquire a dendrite-free metallic-lithium anode by regulating a uniformity of Li ions. Moreover, the porous Al<sub>2</sub>O<sub>3</sub> nanoparticles further improved the electrolyte wettability and thermal stability of the ternary layered LNPA separator. As a result, the Li-S cell cooperating with a LNPA separator exhibited high capacity, excellent rate performance and outstanding cyclic stability. In particular, the good electrochemical performance of Li-S batteries with a high sulfur loadings (4.8 and 7.6 mg cm<sup>-2</sup>) further

demonstrated the practicability and reliability of the ternary designed LNPA membrane as a multifunctional separator. This work provides a new way of thinking to design functional separators for Li-S batteries.

# Chapter 7. Developing a free-standing membrane to simultaneously inhibit shuttle effect and Li dendrites growth

## 7.1 Introduction

In chapter 6, we have prepared a ternary-layered Li@Nafion/PEP/Al<sub>2</sub>O<sub>3</sub> separator to inhibit the polysulfides shuttle and lithium dendrites growth. However, in this work, in order to achieve the multi-functions, we need to introduce a Li@Nafion layer to restrain the polysulfides shuttle, an Al<sub>2</sub>O<sub>3</sub> layer to inhibit the growth of lithium dendrites, and a PEP membrane as the substrate to support the two layers (Figure 7.1a). The excessive raw materials for fabricating a separator may cause high cost. In this case, a novel material that can prepare a free-standing separator with multi-functions still needs to be further developed.

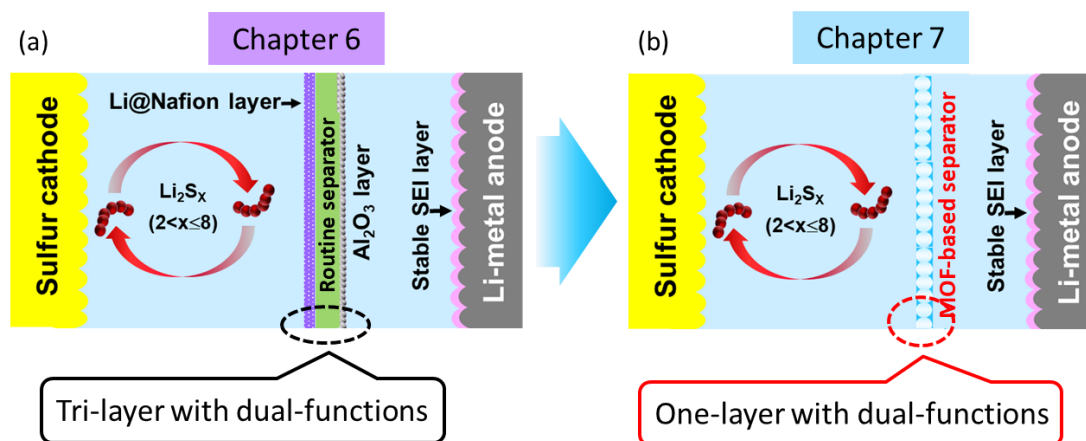


Figure 7.1 Developing (b) a free-standing MOF@PVDF-HFP separator instead of (a) the tri-layered separator to simultaneously inhibit shuttle effect and lithium dendrites growth.

Metal-organic frameworks (MOFs), with highly ordered pore structures, controllable pore sizes and topologies, show multiple advantages in constructing functional separators for Li-S batteries. Our group fabricated a metal-organic

framework@graphene oxide (MOF@GO) separator as an ionic sieve for Li-S batteries.<sup>136</sup> It is known that the length of every S-S chain of lithium polysulfide ( $\text{Li}_2\text{S}_n$ ,  $4 < n \leq 8$ ) in the range of 2.09 Å ~ 2.39 Å. The MOF@GO separator with small pore sizes (9 Å) allowed the shuttle of Li ions but suppress the migration of polysulfides. However, because of the electron conductivity of GO sheets, it may cause self-discharge of cells. What's worse, the intrinsic mechanical brittleness of the MOF resulted in a poor mechanical strength of the MOF@GO membrane, thus they hardly meet the high requirements of durability and stability in practical pouch Li-S cells. Therefore, it is still a big challenge to develop a functional separator, which should not only restrain the issues of polysulfides shuttle and lithium dendrites, but also is able to support the practical batteries for long-term work.

Herein, a flexible metal organic framework-based membrane (MOF@PVDF-HFP) was fabricated by employing the HKUST-1 nanoparticles as assemble units and the PVDF-HFP as binder. As shown in Figure 7.1b, attributed to the small pore size of MOF nanoparticles, the MOF@PVDF-HFP separator is able to prevent the diffusion of the polysulfide anions from cathode side to anode side via physical barrier. Furthermore, the uniform pore size distribution of MOF@PVDF-HFP separator can aid in to obtain homogenous  $\text{Li}^+$  flux, achieving stable Li plating/stripping and inhibiting the growth of lithium dendrites.

## 7.2 Experiment and characterization

### 7.2.1 Chemicals and materials

1,3,5 benzenetricarboxylic acid ( $\text{C}_9\text{H}_6\text{O}_6$ , 99.5%) and Cupric nitrate trihydrate ( $\text{Cu}(\text{NO}_3)_2 \cdot 3\text{H}_2\text{O}$ ) were from Tokyo Chemical Industry Co., Ltd. Poly(vinylidene fluoride-co-hexafluoropropylene) (PVDF-HFP, Mw 455000) , lithium sulfide ( $\text{Li}_2\text{S}$ ,

99.9% purity), lithium bis(trifluoromethanesulfonyl) imide (LiTFSI) and lithium nitrate ( $\text{LiNO}_3$ ) were purchased from Sigma-Aldrich.

### 7.2.2 Synthesis of $\text{Li}_2\text{S}_6$ in DOL/DME

The detailed preparation process of  $\text{Li}_2\text{S}_6$  DOL/DME solution has been described in section 5.2.2.

### 7.2.3 Fabrication of MOF@PVDF-HFP membranes

Preparation of HKUST-1 nanoparticles. The HKUST-1 nanoparticles precursor solution was prepared according a reported method<sup>159</sup>: 1.75 g (7.2 mmol)  $\text{Cu}(\text{NO}_3)_2 \cdot 3\text{H}_2\text{O}$  was dissolved in 50 mL ethanol and 0.84 g (4.0 mmol)  $\text{C}_9\text{H}_6\text{O}_6$  was dissolved in 50 mL ethanol. Then the  $\text{Cu}(\text{NO}_3)_2 \cdot 3\text{H}_2\text{O}$  ethanol solution and  $\text{C}_9\text{H}_6\text{O}_6$  ethanol solution were mixed under continuously stirring for 2 h. Then the color of the mixture changed from a blue clear state to a cloudy one.

Fabrication of MOF@PVDF-HFP membranes. The flexible HKUST-1 @PVDF-HFP membranes were fabricated through a self-assembled process. In detail, 10 ml HKUST-1 precursor solution was firstly filtered through a conventional Celgard 2400 filter membrane. Then turn off the filter pump but keep it at a vacuum state, and it was followed by the addition of PVDF-HFP/acetone solution (0.5 mL,  $0.05 \text{ g mL}^{-1}$ ). Repeating the previous two steps three times to make a compact combination between the HKUST-1 particles. A flexible MOF@PVDF-HFP membrane was finally obtained after peeling off from the Celgard 2400 filter membrane. The obtained MOF@PVDF-HFP membranes were dried at  $80 \text{ }^\circ\text{C}$  for 12 h in a vacuum oven before using.

### 7.2.4 Li//Li symmetric cells assembly

The detailed assembly process of Li//Li symmetric cells has been described in

section 6.2.4. In this chapter, the commercial Celgard 2400 (PP) membranes and MOF@PVDF-HFP-sandwiched Celgard membranes were used as separators.

### 7.2.5 Lithium-sulfur coin cells assembly

All Li-S coin cells were also assembled under the protection of Argon. Standard 2032 coin cells were also used to evaluate the electrochemical performance of Li-S batteries. The cathode materials were prepared by mixed of RGO@S and PVDF (9:1 by weight) in NMP. Then obtained mixed slurry was coated on the carbon paper. After drying at 60 °C for 10 h in a vacuum oven, the mixture coated carbon paper was cut into wafers with diameter of 12 mm and used as cathodes, with mass loading of sulfur around 1~1.5 mg cm<sup>-2</sup>. The anodes were prepared by directly pressing Li metal foils with diameter of 12 mm on stainless steel foils. The electrolyte is 1 M LiTFSI and 2 wt% LiNO<sub>3</sub> in DOL and DME (1:1 by volume). The addition amount of electrolyte in every cell was about 50 μL. The commercial PP membranes and MOF@PVDF-HFP membranes with diameter of 16 mm were used as separators. It should be noted that the MOF can react with polysulfides to form Cu-S bonds, which is an irreversible process. So the MOF@PVDF-HFP membranes were immersed in Li<sub>2</sub>S<sub>6</sub> electrolyte for 48 h to avoid the vacancies of vacancies of copper metal sites. After treated with Li<sub>2</sub>S<sub>6</sub> electrolyte, the MOF@PVDF-HFP membranes were also washed several times by immersing in pure DME solvent to remove the redundant Li<sub>2</sub>S<sub>6</sub> in the MOF, and finally were dried by vacuum valve before using. The amount of inactive sulfur species combined with HKUST-1 to form Cu-S bonds was calculated to be 5 wt%~ 10 wt% of the total mass of sulfur in every cell.

### 7.2.6 H-type lithium-sulfur glass cells assembly

Li-S H-type glass cells were assembled under the same conditions with Li-S coin

cells. It should be pointed out that the sulfur loading of cathode was increased to 3 mg cm<sup>-2</sup>. The electrolyte in each chamber was about 3.5 mL. The Al-strip and Ni-strip were used to bring out the cathode and anode current collectors from the cells.

### 7.2.7 Lithium-sulfur pouch cells assembly

The Li-S pouch cell was assembled by using same cathode materials, electrolyte and anodes with coin cells, while the current collector of cathode was using carbon cloth instead of carbon paper, and the sulfur loading was increased to 5.8 mg cm<sup>-2</sup>. The inner cross structure of the pouch cells is shown as Figure 7.17a. The package material was Al-plastic film. The Ni-strip and Al-strip were used to bring out the current collectors of anode and cathode from the pouch cells.

### 7.2.8 Characterization and electrochemical measurements

The specific test conditions and parameters of SEM, XRD, FT-IR AND XPS are referenced 5.2.7. The test method of ionic conductivity was shown as in 5.2.8. The Li<sup>+</sup> transference number was evaluated by a potentiostatic polarization method shown in 5.2.9. The corresponding separator was changed to PP or MOF@PVDF-HFP membranes. The electrochemical measurements can be referenced 5.2.10.

## 7.3 Results and discussions

### 7.3.1 The morphology and structure of MOF@PVDF-HFP membranes

The MOF@PVDF-HFP membrane was fabricated by a vacuum filtration method (Figure 7.2). The MOF particles solution was firstly filtered through a polyethylene (PP) separator, then a small amount of PVDF-HFP gel solution was introduced. On the one hand, the PVDF-HFP acted as binder to link the MOF particles; on the other hand, the PVDF-HFP with good ductility can fill the void spaces between MOF particles to form a

dense MOF membrane. After repeating the foregoing process three times, a free-standing MOF@PVDF-HFP membrane was obtained. As shown in Figure 7.3a, the as-prepared MOF@PVDF-HFP membrane exhibits good flexibility, which is beneficial for assembling practical pouch cells. The morphology of the MOF@PVDF-HFP was observed by FE-SEM. From the obtained image (Figure 7.3b), it can be seen that the membrane exhibits flat and smooth surface. The corresponding elemental maps of Cu and F imply the uniform distribution of MOF particles and PVDF-HFP. The cross-section SEM image (Figure 7.3c) exhibits that the thickness of the MOF@PVDF-HFP membrane is around 28  $\mu\text{m}$ .

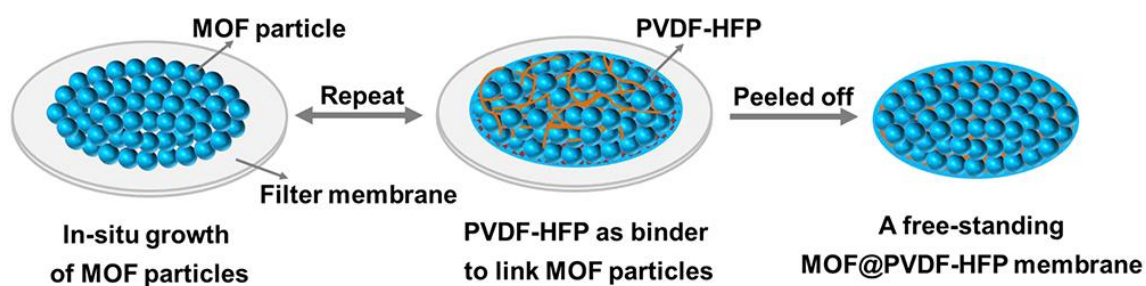


Figure 7.2 Schematic illustration of the preparation process of a free-standing MOF@PVDF-HFP membrane.

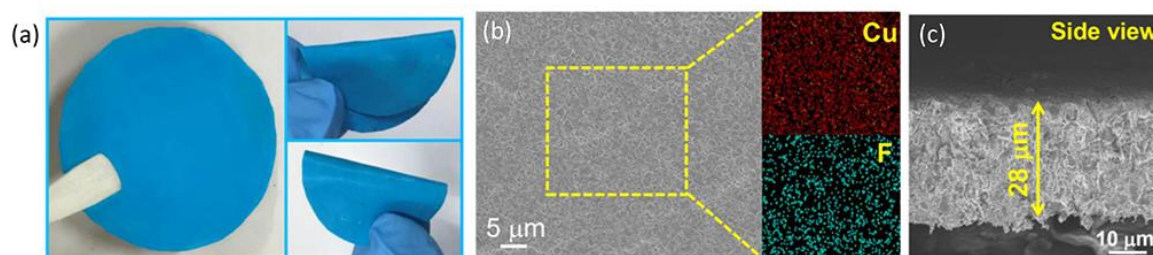


Figure 7.3 (a) Digital photos, (b) FE-SEM image with elemental maps of Cu and F, and (c) cross-section FE-SEM image of MOF@PVDF-HFP separator.

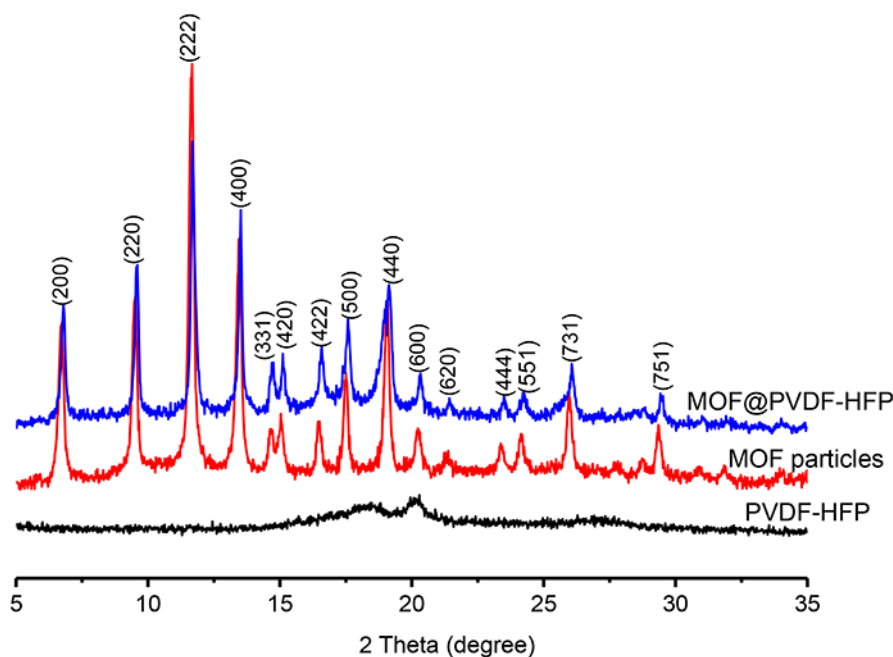


Figure 7.4 PXRD patterns of PVDF-HFP, MOF particles and MOF@PVDF-HFP.

The crystal structures of the pure PVDF-HFP, MOF particles and MOF@PVDF-HFP membrane were revealed by the Powder X-ray diffraction (PXRD) (Figure 7.4). The pure PVDF-HFP shows two broad diffraction peaks located at  $2\theta=18.2^\circ$  and  $20.1^\circ$ , suggesting a semi-crystalline structure of PVDF-HFP.<sup>160, 161</sup> As to the MOF particles, it shows a series of obvious characteristic diffraction peaks, corresponding to the cubic structure of crystalline HKUST-1.<sup>159, 162, 163</sup> The MOF@PVDF-HFP membrane presents a series of same characteristic peaks with that of the MOF precursors, implying a high purity of HKUST-1 crystals in MOF@PVDF-HFP membrane. There are no obvious characteristic diffraction peaks of PVDF-HFP can be observed from the PXRD pattern of MOF@PVDF-HFP membrane, which is mainly because the peaks of PVDF-HFP are overlapped by the peaks of MOFs.

The Fourier transform infrared (FT-IR) technique was further employed to investigate the as-prepared materials. As shown in Figure 7.5, the characteristic peaks of MOF@PVDF-HFP membrane are overlapped with that of pure MOF and PVDF-HFP,

indicating a good combination of MOF with PVDF-HFP. Specifically, the two absorption peaks located at 1072 and 1402  $\text{cm}^{-1}$  are associated with the  $\alpha$  phase of PVDF-HFP, and the peaks around 840 and 879  $\text{cm}^{-1}$  are assigned to  $\beta$  phase of PVDF-HFP, suggesting that the PVDF-HFP in the composite membrane is mainly composed of  $\alpha$ - and  $\beta$ -crystalline phases.<sup>164-166</sup> For the MOF particles, the absorption peaks located at 1450 and 1649  $\text{cm}^{-1}$  are resulted from the  $\text{COO-Cu}_2$  stretching and the peaks located at 1373 and 1570  $\text{cm}^{-1}$  are assigned to the  $-\text{C}=\text{C}-$  stretching.<sup>167, 168</sup> At the same time, the peaks at 730 and 760  $\text{cm}^{-1}$  are attributed to  $\text{C-CO}_2$  stretching, and the vibration at 517  $\text{cm}^{-1}$  is ascribed to the  $-\text{Cu-O}$  stretching vibration.<sup>136, 168</sup>

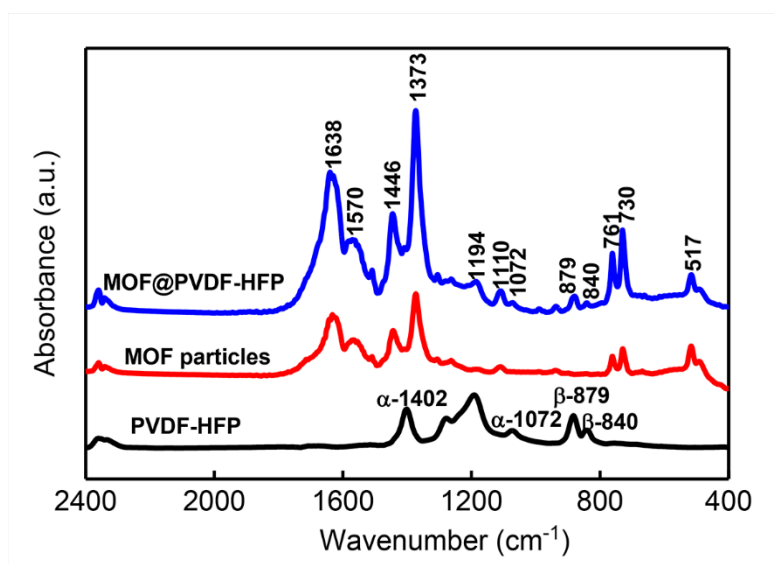


Figure 7.5 FT- IR spectra of PVDF-HFP, MOF particles and MOF@PVDF-HFP.

TGA was used to analyse the respective content of PVDF-HFP and MOF in the composite membrane. The obtained TGA plots of various materials are shown in Figure 7.6. The pure MOF particles show a weight loss in the range of 30~120  $^{\circ}\text{C}$ , which is caused by the evaporation of water or guest molecules. Subsequently weight decrease from ~300  $^{\circ}\text{C}$  is owing to the degradation of BTC linkers, and the remained products is  $\text{CuO}$ .<sup>159</sup> The MOF@PVDF-HFP membrane exhibits a similar decomposition process

with the pure MOF particles except a sudden weight loss (~29.7) at ~430 °C, which is resulted from the PVDF-HFP degradation. The TGA results indicate the good thermal stability of as-prepared MOF@PVDF-HFP, and the mass ratio of PVDF-HFP to MOF in MOF@PVDF-HFP is about 3:7.

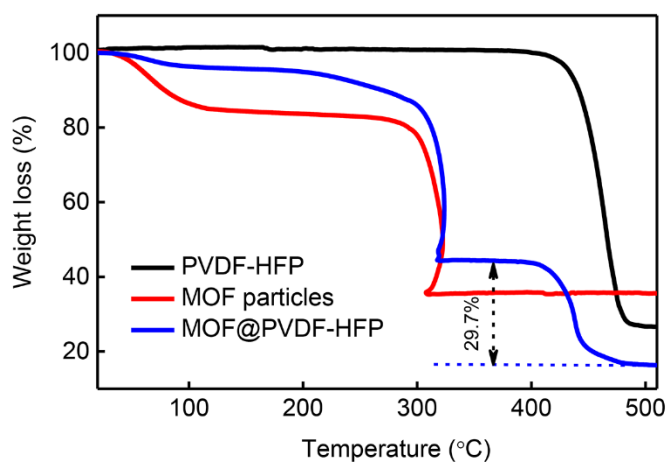


Figure 7.6 TGA curves PVDF-HFP, MOF particles and MOF@PVDF-HFP.

The N<sub>2</sub> adsorption/desorption test was used to investigate the porous structure of the obtained materials. As shown in Figure 7.7, both the isotherms of the MOF particles and MOF@PVDF-HFP membrane belong to type I, suggesting their microporous properties. The specific surface area of pure MOF precursors is determined to be 1206 m<sup>2</sup> g<sup>-1</sup>. After introducing the PVDF-HFP binder, the specific surface area of MOF@PVDF-HFP membrane is decreased to 709 m<sup>2</sup> g<sup>-1</sup>, indicating that partial pores of MOF particles were covered by PVDF-HFP. Nevertheless, the MOF@PVDF-HFP membranes still possess a porous structure with pore size of ~9 Å. The small and uniform pore size of MOF@PVDF-HFP membrane not only can built a physical barrier to inhibit the polysulfides diffusion, but also can aid in forming homogeneous Li-ion fluxes to obtain stable Li electrodeposition, fundamentally suppressing the growth of lithium dendrites.

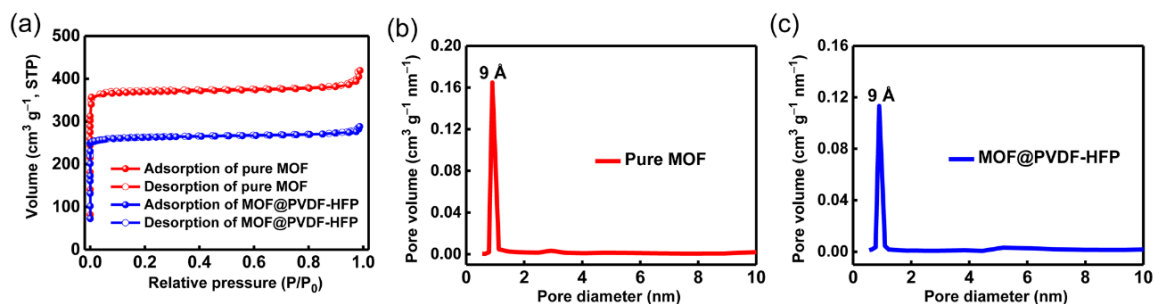


Figure 7.7 (a) N<sub>2</sub> adsorption/desorption isotherms with the corresponding pore size distributions of (b) pure MOF particles and (c) MOF@PVDF-HFP membranes.

### 7.3.2 MOF@PVDF-HFP membrane as an ionic sieve

To verify the availability of MOF@PVDF-HFP membrane for preventing the diffusion of polysulfides, visualized H-type glass Li-S cells were designed and assembled with different separators. As shown in Figure 7.8a, the cathode was prepared by directly coating the sulfur composites on the carbon paper, and the sulfur loading is about 3 mg cm<sup>-2</sup>. The anode was composed of lithium plate and Cu mesh. The Al strip and Ni strip were used for cathode and anode to contact with external circuit separately. The cells were performed at a low current density of 0.1 C from 2.8 to 1.7 V. During the initial discharging process, it can be seen that the rufous long-chain lithium polysulfide species (Li<sub>2</sub>S<sub>x</sub>, 6 ≤ x ≤ 8) were gradually produced in the cathode side (left chamber) of the two visible cells. With the increase of discharging time, the red brown electrolyte was gradually turned to a yellow-green one, which was resulted from the reduction of long chain polysulfides to relative lower chain polysulfides species (Li<sub>2</sub>S<sub>x</sub>, 2 < x ≤ 4). At the same time, in the cell with a routine PP separator (Figure 7.8b), it can be seen that the dissolved polysulfides gradually passed through the separator from left chamber to right chamber after 4 h discharging, and finally reached a high level after 10 h. The phenomenon suggests that the PP separator is unable to prevent the polysulfides

diffusion. On the contrary, no obvious polysulfide species can be observed from the anode side (right chamber) in the cell with a MOF@PVDF-HFP separator during the whole discharging process (Figure 7.8c), convincingly demonstrating that the MOF@PVDF-HFP membrane can effectively block the migration of polysulfides.

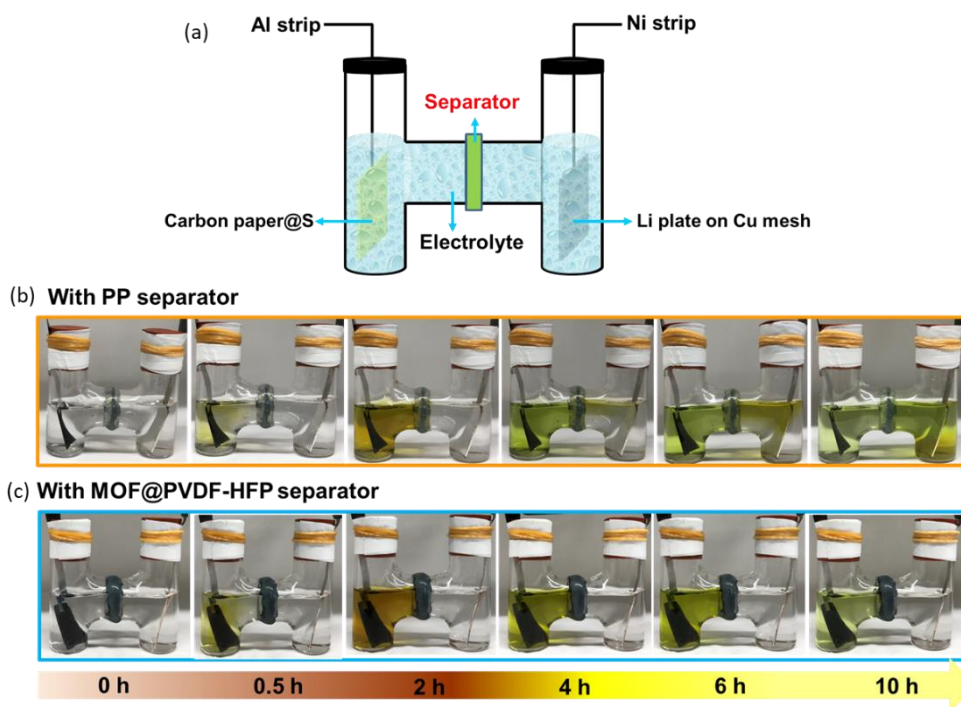


Figure 7.8 (a) The schematic image of H-type Li-S glass cell. Optical images of visible H-type cells with (b) PP separator and (c) MOF@PVDF-HFP separator during a discharging process.

To further prove the ionic selectivity of MOF@PVDF-HFP separators, the  $\text{Li}^+$  transference number ( $t_{\text{Li}^+}$ ) was measured. As shown in Figure 7.9, it can be seen that the system with a routine PP separator shows a  $t_{\text{Li}^+}$  around 0.41, which agree with the value reported from the previous literatures. After introducing a MOF@PVDF-HFP separator, the  $t_{\text{Li}^+}$  of the system is significantly increased to 0.76. The enhancement of  $t_{\text{Li}^+}$  further implies that the MOF@PVDF-HFP separator allows the transfer of  $\text{Li}^+$  while prevents the diffusion of polysulfide ions.

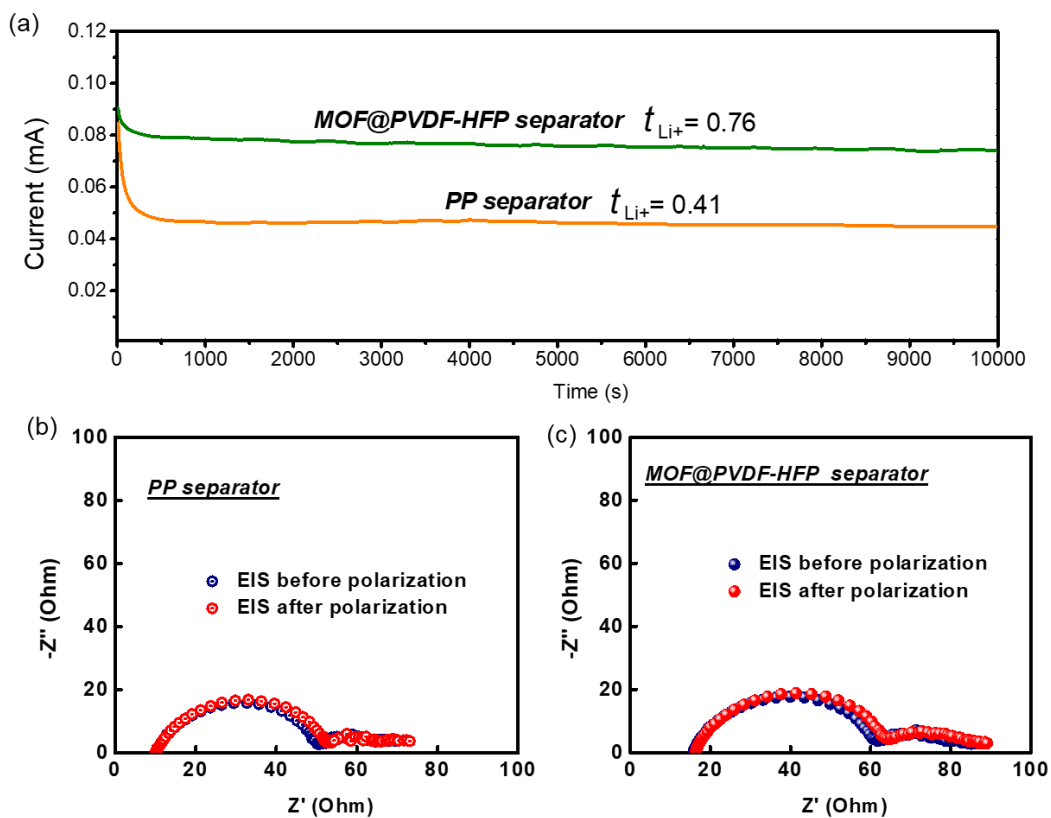


Figure 7.9 (a) The characteristic of  $\text{Li}^+$  transference number: polarization curves of symmetric cells with different separators. The EIS spectra of the cell with (b) a PP separator and (c) a MOF@PVDF-HFP separator before and after polarization.

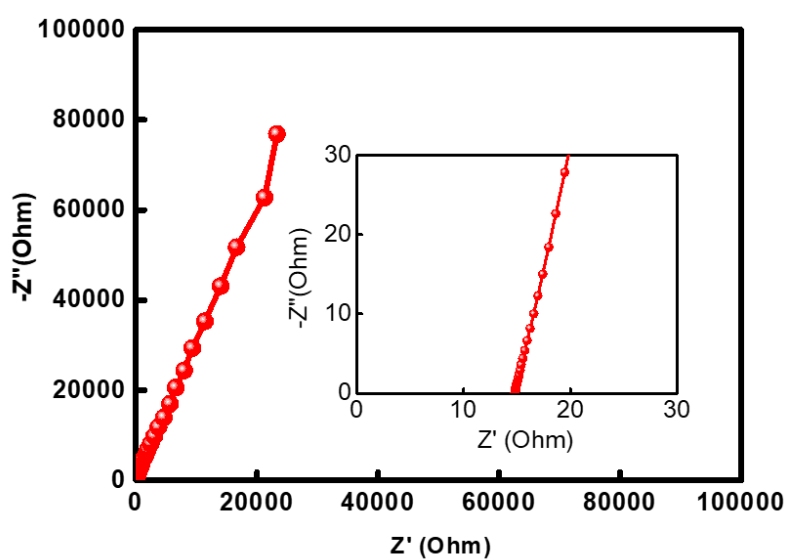


Figure 7. 10 Electrochemical impedance spectra of MOF@PVDF-HFP separator.

The ion conductivity of MOF@PVDF-HFP was carried out by a symmetric coin cell with two stainless steel electrodes at room temperature. As shown in Figure 7.10, the ion conductivity of MOF@PVDF-HFP is calculated to be  $0.094 \text{ mS cm}^{-1}$ , which is just slightly lower than that of a PP separator ( $0.138 \text{ mS cm}^{-1}$ ). The high ion conductivity suggests that although the MOF@PVDF-HFP can effectively block the diffusion of polysulfide anions, it almost has no negative influences on the transport of lithium ions.

### 7.3.3 Lithium plating/stripping stability

To evaluate the availability of MOF@PVDF-HFP for inhibiting the growth of lithium dendrites, the lithium plating/stripping stability was investigated by Li//Li symmetric cells with different separators. As is shown in Figure 7.11a, the Li//Li cell with a PP separator shows an average overpotential around 30 mV at a current density of  $2 \text{ mA cm}^{-2}$  with areal capacity of  $1 \text{ mA h cm}^{-2}$  in the first few cycles. The stable lithium plating/stripping process lasted about 150 h. Then the overpotential of the cell was gradually increased as the increase of the cycle number. After 618 cycles, the overpotential reached to 2 V, which is the cut off voltage. The premature failure of Li//PP//Li symmetric cell was mainly caused by the overgrown lithium dendrites, which gave rise to rapid consumption of both fresh lithium metal and electrolyte, aggravated side reactions and high polarization. For the Li//Li symmetric cell with a MOF@PVDF-HFP separator, the overpotential of the cell slightly higher than the cell with a PP separator, this may be because a little thicker of the MOF@PVDF-HFP membrane. With the increase of cycle number, the overpotential of the cell remains stable and shows a low overpotential of 45 mV even after 1000 h cycling, indicating the introduction of MOF@PVDF-HFP separator can achieve a stable lithium plating/stripping process.

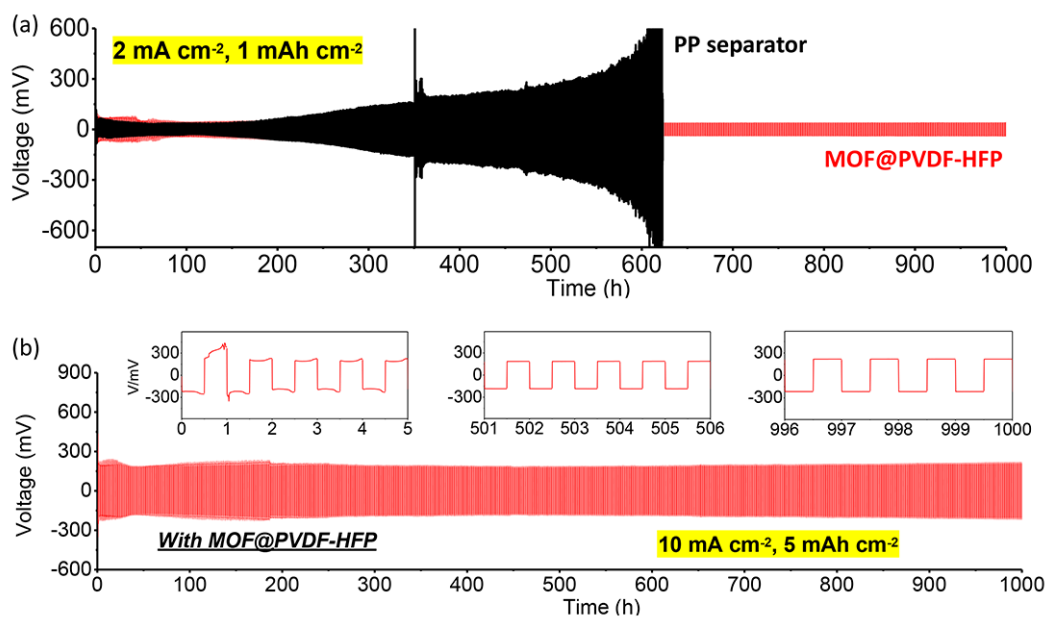


Figure 7.11 (a) Lithium plating/stripping stability of the symmetric cell with PP separator and MOF@PVDF-HFP separator. (b) Lithium plating/stripping stability of the cell with a MOF@PVDF-HFP separator at a high current density of  $10 \text{ mA cm}^{-2}$  with selected voltage profiles insets.

To further evaluate the reliability of MOF@PVDF-HFP for the high requirements of fast charging/discharging in practical applications, the current density was increased to ultra-high current density of  $10 \text{ mA cm}^{-2}$  with areal capacity of  $5 \text{ mA h cm}^{-2}$ . The obtained voltage profiles are shown as Figure 7.11b, it can be seen that the overpotential exhibits a slight fluctuation in the initial few cycles. This is probably caused by the original unstable composites on the surface of lithium metal, which makes the cell need an activation process in the case of cycling at such a high rate. Subsequently, the overpotential of the cell gradually became stable and maintained at about 185 mV. No obvious circuit phenomenon was observed during the whole discharging/charging process, further demonstrating that the potential possibility of MOF@PVDF-HFP membrane for practical applications.

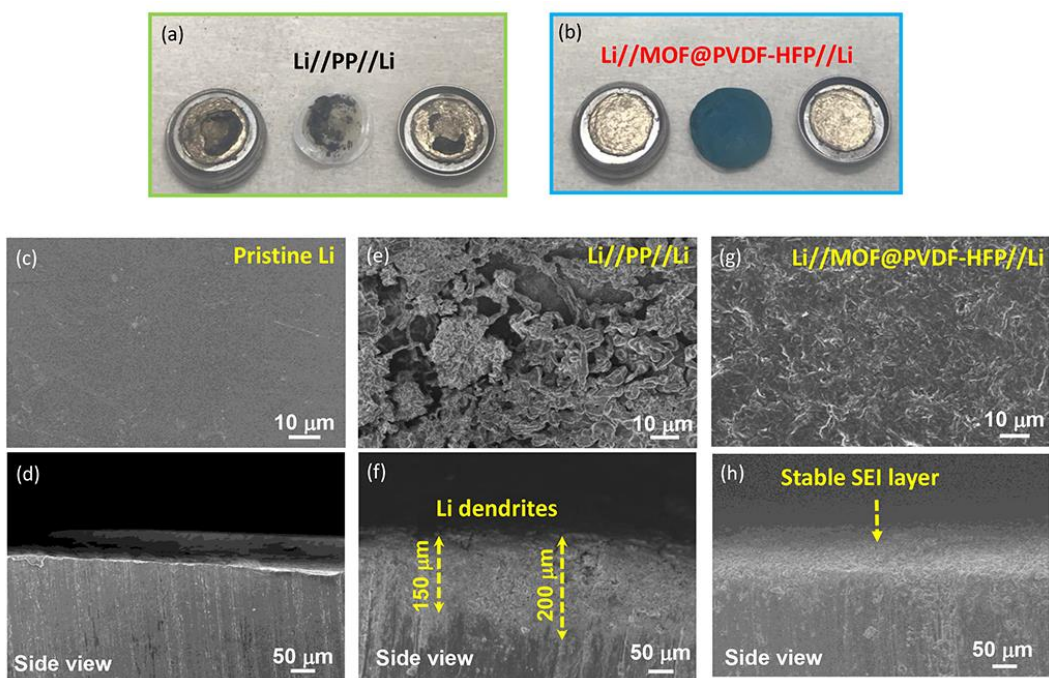


Figure 7.12 Digital photos of the detached Li//Li symmetric cells with (a) a PP separator and (b) a MOF@PVDF-HFP separator after cycling. SEM images of (c, d) pristine lithium metal, (e, f) from the PP-cell, and (g, h) from the MOF@PVDF-HFP cell.

To reveal the state of the lithium metal anodes after cycling, the symmetric cells with different separators tested at the current density of  $2 \text{ mA cm}^{-2}$  were detached. From Figure 7.12a, it can be seen that the lithium metal electrodes from the cell with a PP separator has been seriously destroyed, and a large proportion of the metals have been pulverized. On the contrary, the both lithium metal anodes from the cell with a MOF@PVDF-HFP separator still showed flat surface, which have bright metallic luster (Figure 7.12b). The microstructures of Li metal electrodes after cycling were further observed by FE-SEM. For the pristine Li metal, it exhibits a smooth and flat surface (Figure 7.12c, d). After cycling in a Li//PP//Li cell, the lithium metal became loose with a lot of lithium dendrites on the surface (Figure 7.12e). The cross-section SEM image revealed the corrosion of electrode by the side reaction between lithium metal and

electrolyte reached nearly 200  $\mu\text{m}$  (Figure 7.12f), indicating of a large amount of fresh lithium metal was consumed. For the lithium metal electrode from a cycled cell with MOF@PVDF-HFP separator (Figure 7.12g), it still maintained a flat and compact surface, and no obvious cracks can be observed. Its cross-section SEM image shows a dense interface with a uniform SEI layer on the lithium electrode surface (Figure 7.12h), further confirming that the MOF@PVDF-HFP membrane can effectively inhibit the growth of lithium dendrites.

### 7.3.4 Electrochemical performance of lithium-sulfur batteries

The electrochemical performance of Li-S batteries was firstly evaluated by coin cells, which used the RGO@S (S content of 87 wt%) as cathode materials, lithium metal foils as anodes, and PP or MOF@PVDF-HFP membranes as separators. The  $\text{Li}^+$  diffusion coefficient ( $D_{\text{Li}^+}$ ) was evaluated by cyclic voltammogram (CV) at various scan rates from 0.1 to 0.4  $\text{mV s}^{-1}$ . (Figure 7.13a, b). All CV curves presented two characteristic reduction peaks around 2.3 and 2 V (assigned as  $\beta$  and  $\gamma$ ), corresponding to the reduction the sulfur to long-chain polysulfide species at the higher potential and the further reduction of long-chain polysulfides to  $\text{Li}_2\text{S}_2/\text{Li}_2\text{S}$  at the lower potential.<sup>121</sup> The peaks around 2.5 V (assigned as  $\alpha$ ) were contributed to the oxidation of  $\text{Li}_2\text{S}_2/\text{Li}_2\text{S}$  to element sulfur. From the linear fitting of the peak currents (Figure 7.13c, d), we calculated the  $D_{\text{Li}^+}$  by the classical Randles-Sevick equation.<sup>169, 170</sup> According to the slope of the linear fit, the diffusion coefficients at different CV voltage regions for the cell with routine PP separator were calculated to be  $D_{\text{Li}^+(\alpha_1)} = 4.25 \times 10^{-8} \text{ cm}^2\text{s}^{-1}$ ,  $D_{\text{Li}^+(\beta_1)} = 2.87 \times 10^{-8} \text{ cm}^2\text{s}^{-1}$ , and  $D_{\text{Li}^+(\gamma_1)} = 5.41 \times 10^{-9} \text{ cm}^2\text{s}^{-1}$ , respectively. After incorporating with a MOF@PVDF-HFP membrane, the diffusion coefficients were determined to be  $D_{\text{Li}^+(\alpha_2)} = 3.28 \times 10^{-8} \text{ cm}^2\text{s}^{-1}$ ,  $D_{\text{Li}^+(\beta_2)} = 1.15 \times 10^{-8} \text{ cm}^2\text{s}^{-1}$ , and  $D_{\text{Li}^+(\gamma_2)} = 5.61 \times 10^{-9} \text{ cm}^2\text{s}^{-1}$ , respectively,

sufficiently illustrating that the introduction of MOF@PVDF-HFP did not impact on the diffusion of the  $\text{Li}^+$ .

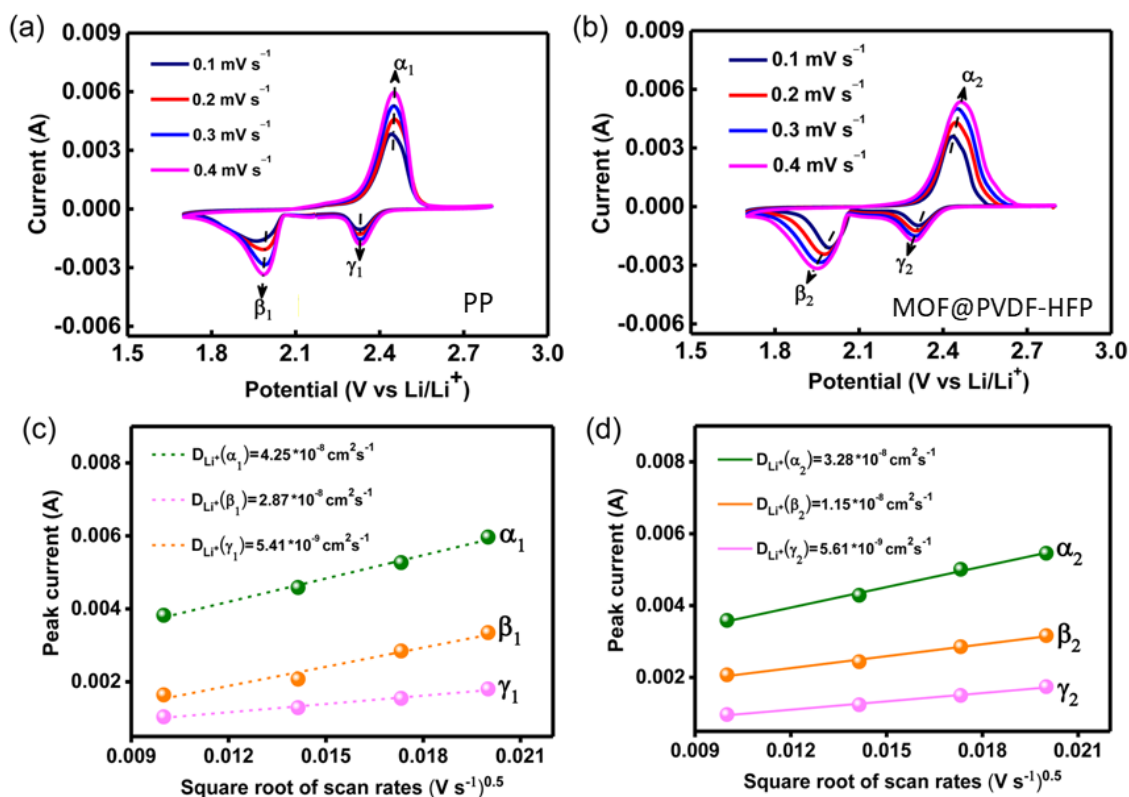


Figure 7.13 Cyclic voltammograms profiles at different scan rates of Li-S coin cells: (a) PP separator and (b) MOF@PVDF-HFP separator. The linear fits of the peak currents for cells with (c) PP separator and (d) MOF@PVDF-HFP separator.

The rate performance was tested from 0.1 C to 3 C. The cell with a PP separator shows an initial discharge capacity of  $1231 \text{ mA h g}^{-1}$  at 0.1 C (Figure 7.14a), which is  $91 \text{ mA h g}^{-1}$  lower than that of a MOF@PVDF-HFP-cell ( $1322 \text{ mA h g}^{-1}$ ), indicating that the MOF@PVDF-HFP separator can enhance the utilization of active materials. Then the capacity decreased rapidly as the rate increased. When the rate increased to 3 C, only  $373 \text{ mA h g}^{-1}$  discharge capacity was delivered. For the cell with a MOF@PVDF-HFP separator, when the current density gradually increased from 0.2 C to 3 C, it still exhibited high discharge capacities of 1123, 1001, 916, 776, and  $633 \text{ mA h g}^{-1}$ , indicating good

reversibility and stability of the MOF@PVDF-HFP-cell. The corresponding charge/discharge profiles are shown as Figure 7.14b. All of them present two discharge plateaus, attributing to the two typical reduction stages, which agree with the CV curves. Even the current density increased to 3 C, it still maintained flat and stable charge/discharge plateaus with a low difference between discharge and charge plateau (0.63 V), further demonstrating that the MOF@PVDF-HFP membrane is beneficial for achieving an outstanding rate performance. The enhanced rate performance of the Li-S cell with MOF@PVDF-HFP separator was attributed to following factors: (1) the efficient suppression of polysulfides shuttle and Li dendrites growth greatly enhanced the reutilization of active species; (2) the high  $\text{Li}^+$  transference number was in favour of a higher attainable state of charge at high rates, where a large and constant current was essential to quickly charge the battery;<sup>150, 151</sup> (3) the porous structure of the membrane made free diffusion of electrolyte ions even at a high rate.

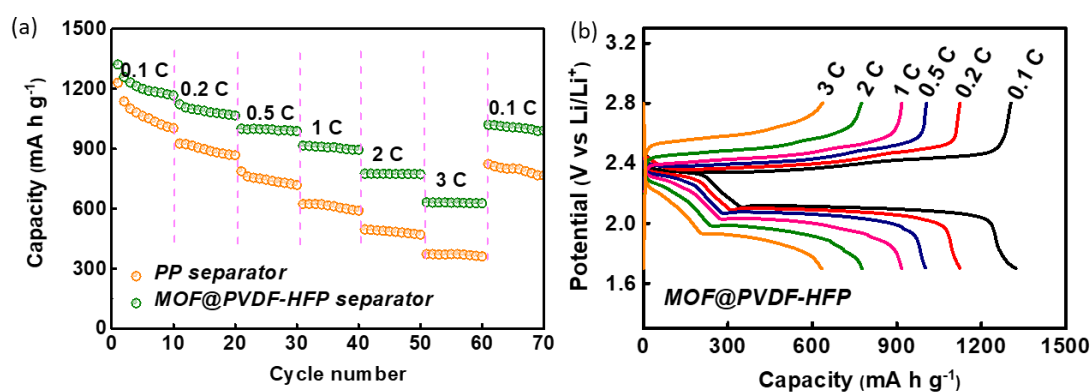


Figure 7. 14 (a) The comparison of rate performance of Li-S cells assembled by different separators at various current densities. (b) Voltage profiles of Li-S cell assembled by a MOF@PVDF-HFP separator.

The cycling performance were conducted at 0.5 C. As shown in Figure 7.15a, the initial discharge capacity of the cell assembled by a PP separator is 1118 mA h g<sup>-1</sup>. With the increase of the cycle number, the capacity decreased quickly. After 600 cycles, the

cell with a PP separator just maintains a low reversible capacity of  $304 \text{ mA h g}^{-1}$ . The average capacity decay rate is as high as 0.121% per cycle. For the Li-S cell with a MOF@PVDF-HFP separator, it can be seen that it shows a higher initial discharge capacity of  $1196 \text{ mA h g}^{-1}$ , indicating a higher utilization of sulfur. Furthermore, after 600 cycles, the cell still can deliver a high reversible capacity of  $802 \text{ mA h g}^{-1}$ , with a low capacity decay rate of 0.059% per cycle. The capacity retention was enhanced by approximately 40%. The outstanding cyclic stability of the Li-S cell is attributed to the effective inhibition of polysulfides shuttle and lithium dendrites growth by the MOF@PVDF-HFP separator. It should be noted that the thickness of the MOF@PVDF-HFP membrane plays an important role for the electrochemical of the Li-S cell. The MOF@PVDF-HFP separators with thickness of 20, 28 and  $45 \mu\text{m}$  were prepared and used to assemble Li-S cells. Their cycling performance were evaluated at a current of 1 C (Figure 7.15b). The cell with a  $28 \mu\text{m}$ -MOF@PVDF-HFP separator shows a nearly initial discharge capacity with that of the cell with a  $20 \mu\text{m}$ -MOF@PVDF-HFP separator, while is much higher than that of the cell with a  $45 \mu\text{m}$ -MOF@PVDF-HFP separator. This is because the too thick separator would lead to a high polarization. Besides, we can see that if the separator is too thin, it is difficult to prevent the polysulfides shuttle for too long time. Therefore, designing an appropriate thickness of MOF@PVDF-HFP separator is significant for the electrochemical performance of Li-S batteries.

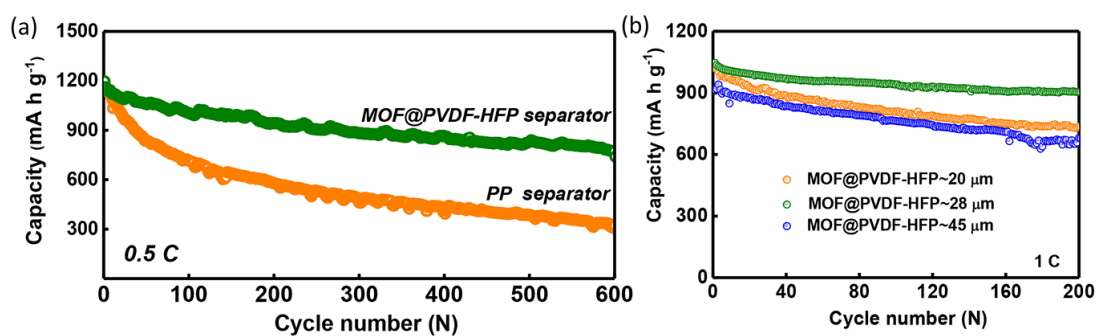


Figure 7.15 (a) The cycling performance of Li-S cells with different separators. (b) Cycle stability of Li-S cell with MOF@PVDF-HFP membranes with different thickness.

The cell with a MOF@PVDF-HFP separator was further carried out at a high rate of 2 C (Figure 7.16). It can be seen that the cell delivered a relatively low capacity at in the initial cycles, and then it gradually increased to 913 mA h g<sup>-1</sup>. This is because the cell charged/discharged at a high current density need an active process. As the continually charging/discharging, more and more sulfur participated in the electrochemical reactions. Some representative charge/discharge profiles of 1-5, 996-1000, and 1996-2000 cycles are shown below of Figure 7.16, it can be seen that the polarization gradually reduced with the increase of the cycle number. As a result, the cell achieves an ultralow average capacity fading rate of 0.015% per cycle after a long-term cycle of 2000 cycles. The comprehensive electrochemical performance of Li-S cell assembled by a MOF@PVDF-HFP separator is superior than most of recent the state of art Li-S batteries using composited sulfur cathodes, protective lithium anodes, as well as the functional separators (Table 7.1).<sup>68, 136, 149, 171-180</sup>

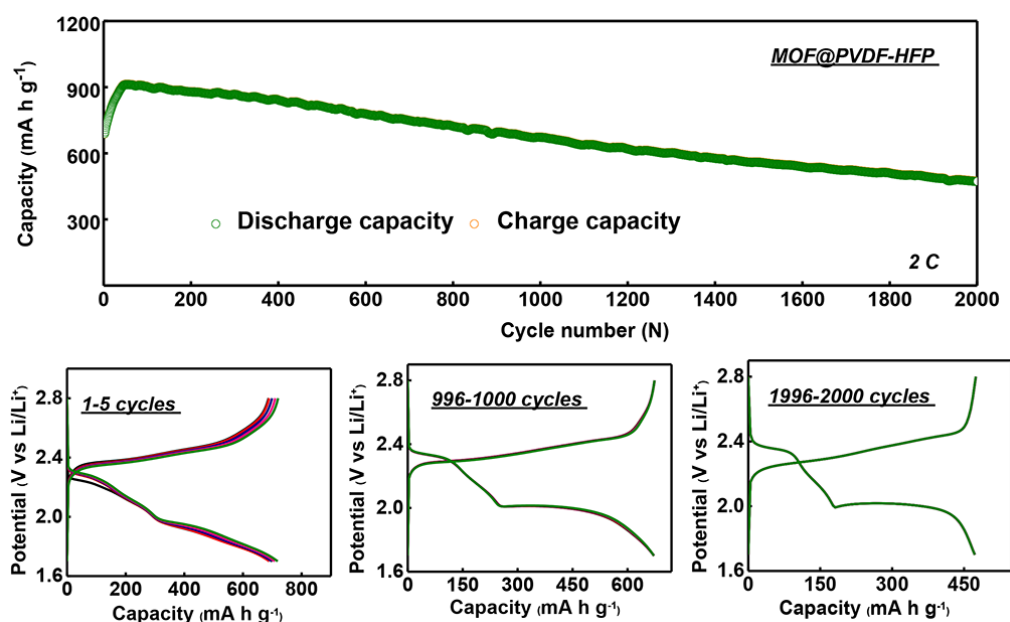


Figure 7.16 Ultralong-term cycling performance with selected voltage profiles of Li-S cell with a MOF@PVDF-HFP separator at 2 C.

Table 7.1 Comparison of Li-S cell in this work with other Li-S batteries.

Cathode	Anode	Separator	Maximum Capacity (mA h g <sup>-1</sup> )	Rate Capacity (mA h g <sup>-1</sup> )	Cycling Performance			Ref.
					Rate	Cycle Number	Fading Rate/Cycle	
MOF-525(Cu)/S	Li metal	pp	1200 (0.5 C)	400 (5 C)	0.5 C	200	0.070%	174
h-CNT/S/ZrO <sub>2</sub>	Li metal	PP	1176 (0.1 C)	658 (2 C)	0.5 C	200	0.114%	175
ZIF-8/S	Li metal	PP	1055 (0.1 C)	710 (1 C)	0.5 C	300	0.08%	176
GNS-MIL-101/S	Li metal	PP	1193 (0.1 C)	500 (3 C)	0.1 C	40	0.32%	177
Covalent triazine/S	Li metal	PP	670 (0.05 C)	383 (2 C)	1 C	300	0.047%	178
Ni-MOF/S	Li metal	PP	689 (0.1 C)	287 (2 C)	0.1 C	100	0.11%	179
Carbon@S	Li <sub>3</sub> N/Li	PP	1200 (0.2 C)	1087 (0.5 C)	0.5 C	500	0.058%	68
Carbon cloth@S	Al <sub>2</sub> O <sub>3</sub> /Li	PP	1200 (0.1 C)	-	0.1 C	100	0.030%	180
Carbon@S	Li metal	Ni <sub>3</sub> (HITP) <sub>2</sub> /PP	1186 (0.2 C)	589 (5 C)	1.0 C	500	0.032%	181
Carbon@S	Li metal	Red phosphorus/PP	1287 (0.1 C)	809 (2 C)	1.0 C	500	0.036%	182
Super P@S	Li metal	Gum Arabic/CNF	1256 (0.2 C)	568 (3 C)	1.0 C	250	0.024%	183
Carbon@S	Li metal	NiFe LDH	1192 (0.05 C)	709 (2 C)	2.0 C	1000	0.060%	150
CMK-3@S	Li metal	HKUST-1@GO	1072 (0.2 C)	488 (3 C)	1.0 C	1500	0.019%	137
<b>RG0@S</b>	<b>Li metal</b>	<b>MOF@PVDF-HFP</b>	<b>1322 (0.1 C)</b>	<b>633 (3 C)</b>	<b>2 C</b>	<b>2000</b>	<b>0.015%</b>	<b>This work</b>

Additionally, a flexible Li-S pouch cell (2.5 cm × 2.5 cm) was also assembled to further evaluate the practicability of MOF@PVDF-HFP membrane (Figure 7.17a, b). The sulfur loading of the pouch cell was increased to 5.8 mg cm<sup>-2</sup>. Initially, the pouch cell delivers a discharge capacity of 1269 mA h g<sup>-1</sup> at 0.1 C, corresponding to an areal capacity of 7.46 mA h cm<sup>-2</sup>, suggesting a high utilization of sulfur. Then the Li-S pouch cell was cycled continuously at various degrees bending state. As shown in Figure 7.17c, the charge and discharge capacities were almost not influenced by the bending of pouch cells. Even after 200 cycles, a high reversible capacity of 936 mA h g<sup>-1</sup> still can be achieved. Besides the effective suppression of polysulfides shuttle and lithium dendrites growth, such an outstanding electrochemical performance of the Li-S pouch cell is also attributed to the good flexibility of MOF@PVDF-HFP separator. The results further demonstrated that the MOF@PVDF-HFP membrane has great potential for developing high-performance practical Li-S cells.

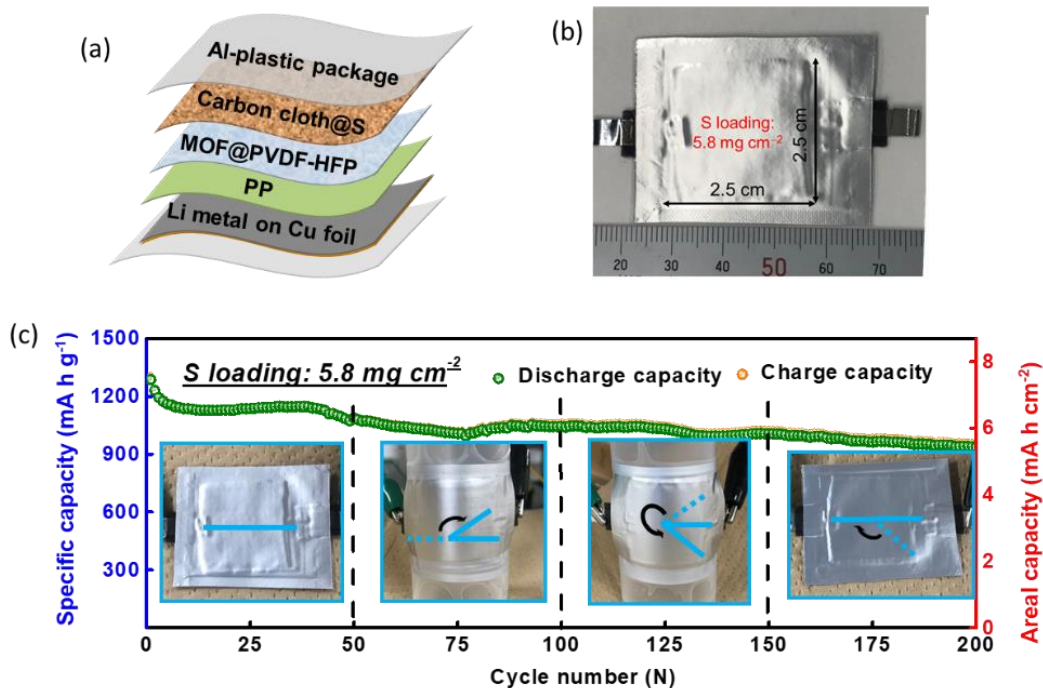


Figure 7. 17 (a) Schematic of the inner structure and (b) digital photograph of a Li-S pouch cell with a MOF@PVDF-HFP separator. (c) Cyclic stability of the Li-S pouch cell at 0.1 C under various degrees bending state.

### 7.3.5 The characterization of MOF@PVDF-HFP after cycling

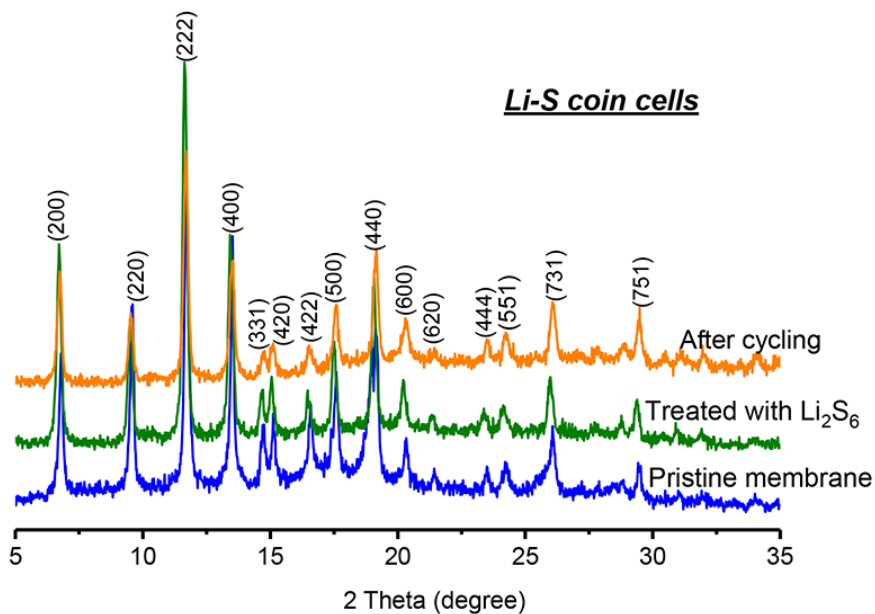


Figure 7. 18 PXRD patterns of MOF@PVDF-HFP membranes at different stages.

The PXRD was used to investigate the structure stability of the MOF crystals in the Li-S battery systems (Figure 7.18). The almost same PXRD patterns of MOF@PVDF-HFP membranes after different treatments imply that the MOFs remained well crystal phase and structural skeleton no matter being treated in a polysulfides-contained electrolyte or cycling in a Li-S cell. For the FT-IR spectra (Figure 7.19), it can be seen that an obvious absorption peak at  $613\text{ cm}^{-1}$  appears after treating in  $\text{Li}_2\text{S}_6$  solution and after cycling. This is because some polysulfides were anchored by the open copper metal sites of HKUST-1 to form Cu-S bonds.<sup>181, 182</sup> Nevertheless, it is unnecessary to concern about the destruction of MOF structure during the discharging/charging process, since most copper metal sites in the MOF have been occupied by oxygen groups, and only few open copper metal sites are available for forming the Cu-S bonds.<sup>136, 183</sup> The FE-SEM image of MOF@PVDF-HFP with corresponding elements maps of Cu, F, and S are shown in Figure 7.20. It can be seen that the MOF@PVDF-HFP separator after cycling still maintained a stable structure with a flat surface. The maps of Cu, F indicates the with MOFs and PVDF-HFP are distributed uniformly across the entire separator. Additionally, sparse distribution of element S implies is because the available vacancies of copper metal sites can anchor the polysulfides through the formation of Cu-S bonds.

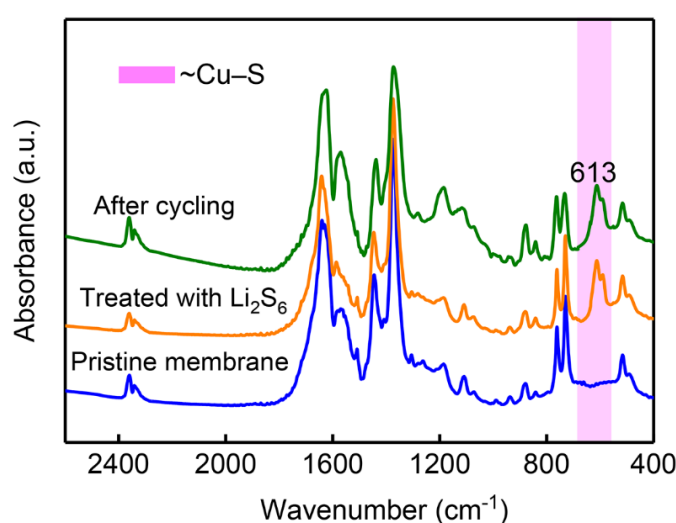


Figure 7.19 FT-IR spectra of MOF@PVDF-HFP at different stages.

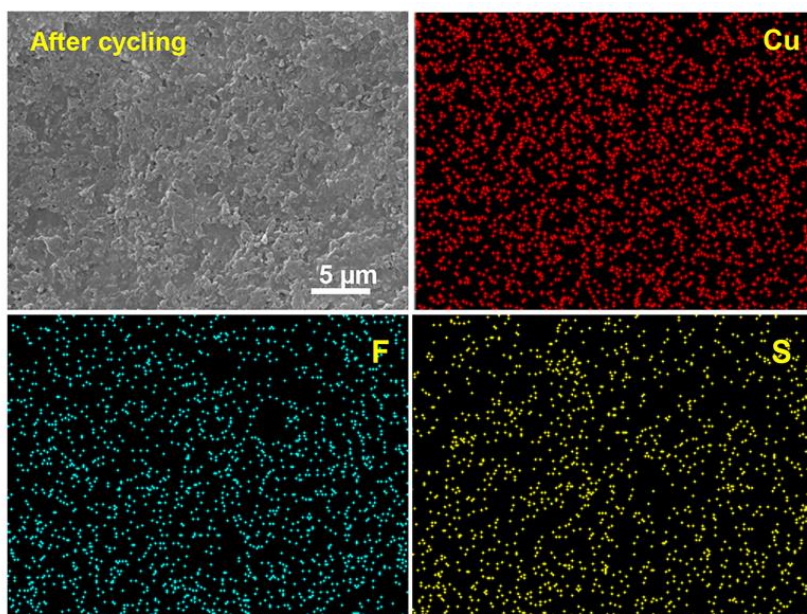


Figure 7.20 FE-SEM image with the corresponding elemental maps of Cu, F and S of MOF@PVDF-HFP membrane after cycling in Li-S coin cell.

X-ray photoelectron spectroscopy (XPS) was also employed to analyse the chemical environment within the MOF@PVDF-HFP separator after cycling (Figure 7.21). For the Figure 7.21a, it can be seen that obvious S 2s and S 2p peaks appear after cycling, which is resulted from the combination of polysulfides and MOF. Additionally, the shift of Cu 2p peaks at 953.9 eV ( $2p_{1/2}$ ) and 933.6 eV ( $2p_{3/2}$ ) to lower binding energies at 952.9 and 933.1 eV further suggests that a new local environment of Cu was formed after cycling<sup>184, 185</sup> (Figure 7.21b). Besides, the Cu 2p splitting peak shows three splitting peaks at 932.7, 933.7 and 952.9 eV, which are corresponded to  $\text{Cu}^+$   $2p_{3/2}$ ,  $\text{Cu}^{2+}$   $2p_{3/2}$  and  $\text{Cu}^{2+}$   $2p_{1/2}$ , respectively.<sup>184, 186</sup> As to the splitting peak of S 2p, the peaks located at 162.6 and 163.5 eV are attributed to terminal sulfur ( $\text{S}_T^{-1}$ ) and bridging sulfur ( $\text{S}_B^0$ ) and respectively.<sup>149, 187</sup> Compared to the previous report,<sup>188</sup> the shift of the  $\text{S}_T^{-1}$  bond at 162.6 eV to 163.5 eV is caused by the formation of Cu-S bond. At the same time, the peaks located at 169.0 and 167.8 eV suggest the formation of thiosulfate and polythionate.<sup>184, 186</sup>

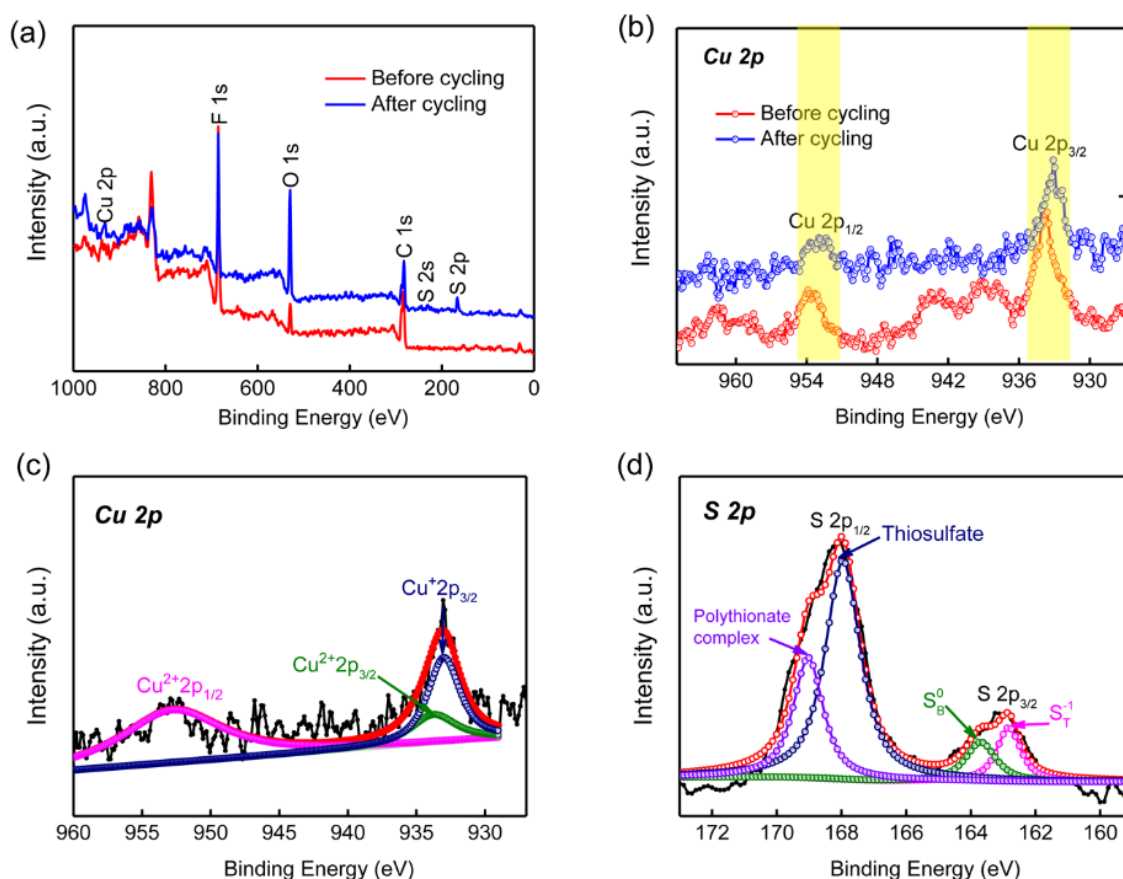


Figure 7.21 (a) Survey XPS and (b) Cu 2p XPS spectra of MOF@PVDF-HFP before and after cycling. (c) Cu 2p and (d) S 2p XPS spectra of MOF@PVDF-HFP membrane after cycling. In (c) and (d), (-●-) represents experimental XPS curve, where (-○-) represents the fitted XPS curve by using Gaussian-Lorentzian function after performing a Shirley background correction.

## 7.4 Summary

In summary, a flexible and free-standing MOF@PVDF-HFP membrane was fabricated via a facial and simple vacuum filtration method. The highly ordered pore structure and uniformly distributed pore size of MOF particles can aid in forming even Li<sup>+</sup> flux, thus the growth of lithium dendrites was fundamentally inhibited. The Li/Li symmetric cell assembled by a MOF@PVDF-HFP membrane showed good lithium

plating/stripping stability even increased the current density to  $10 \text{ mA cm}^{-2}$ . Besides, benefitting from the small pore size of MOF nanoparticles, the MOF@PVDF-HFP membrane acted as a physical barrier to prevent the diffusion of polysulfides. As a result, the Li-S cell achieved an ultralong long cycle life over 2000 cycles with low capacity fading of 0.015 % per cycle at 2 C. Moreover, in the case of a high sulfur loading of  $5.8 \text{ mg cm}^{-2}$ , the flexible Li-S pouch cell with a MOF@PVDF-HFP separator still delivered a high capacity ( $1269 \text{ mA h g}^{-1}$ ) and excellent cycling performance ( $936 \text{ mA h g}^{-1}$  after 200 cycles) at various bending states, further demonstrating the potential of MOF@PVDF-HFP membrane for the development of practical energy storage devices.

## Chapter 8. Conclusions

Separator is an essential component in rechargeable Li-S batteries, since it not only can act as an isolator to prevent the electrical contact between the cathode and anode, but also can serve as a reserve of liquid electrolyte to regulate the diffusion of ions. In the present research, to address the issues of polysulfides shuttle and lithium dendrites growth in Li-S batteries, we have fabricated three-types functional separators and made a series of investigations and analyses towards the feasibility and electrochemical performance.

Main results obtained are as follows:

(1) We built a “polysulfide-phobic” interface by introducing polysulfides on the surface of polar VOPO<sub>4</sub> hosts. The time/space-resolved operando Raman evidences convectively suggested that the constructed “polysulfide-phobic” surface produce strong repulsion effect on the free polysulfide anions in the bulk solution via Coulombic interactions. At the same time, the permeation experiment conducted by visible V-type devices showed that the separator with a “polysulfide-phobic” layer can effectively prevent the diffusion of polysulfides. When applied the “polysulfide-phobic” strategy in Li-S batteries, a high capacity retention of 75.3% with a low average capacity fading of 0.082% at 0.2 C was achieved;

(2) Introducing a Li@Nafion layer with negatively charged -SO<sub>3</sub><sup>-</sup> also can construct a “polysulfide-phobic” surface to inhibit the polysulfides diffusion. Besides, coating an Al<sub>2</sub>O<sub>3</sub> layer with a narrow pore size window can acquire a dendrite-free metallic-lithium anode by regulating uniform Li ions flux. Moreover, the porous structure of Al<sub>2</sub>O<sub>3</sub> nanoparticles are beneficial for improving the electrolyte wettability of the separator. As a result, the Li-S cell assembled with a Li@Nafion/PEP/Al<sub>2</sub>O<sub>3</sub> separator exhibited an ultrahigh capacity retention (77.2%) along with a low capacity decay rate

(0.022% per cycle) after 1000 cycles at 1 C. Furthermore, the good electrochemical performance of Li-S coin cell with high sulfur loadings (4.8 and 7.6 mg cm<sup>-2</sup>) further demonstrated the practicability and reliability of the ternary separator;

(3) A free-standing MOF@PVDF-HFP membrane with good flexibility was fabricated via a facial vacuum filtration strategy. The highly ordered pore structure and narrow pore size window can simultaneously suppress the polysulfides shuttle and inhibit the growth of lithium dendrites. By employing the MOF@PVDF-HFP membrane as separator, the Li-S coin cell realized an ultralong long cycle life over 2000 cycles with low capacity fading of 0.015 % per cycle at a high rate of 2 C. Moreover, the practical Li-S pouch cell with a high sulfur loading of 5.8 mg cm<sup>-2</sup> can still deliver a high capacity (1269 mA h g<sup>-1</sup>) and excellent cycling performance (936 mA h g<sup>-1</sup> after 200 cycles) at various bending states. The results demonstrate the reliability and practicability of MOF@PVDF-HFP membrane for developing high-performance Li-S batteries.

According to the obtained results, we summarized the properties of the three types of separators (Table 8.1) and made several significant conclusions as follows:

Table 8.1 Summary of the properties of the three types of separators.

<b>Separators</b>	<b>Advantages</b>	<b>Disadvantages</b>
<b>S<sub>6</sub><sup>2-</sup>-VOPO<sub>4</sub>/PP</b>	low cost, good flexibility, adjustable thickness, inhibiting the polysulfides shuttle	complex preparation process, small size of the separator, can't inhibit the Li dendrites growth
<b>Li@Nafion/PEP/Al<sub>2</sub>O<sub>3</sub></b>	good flexibility, adjustable thickness, easy to scale up, simultaneously inhibiting polysulfides shuttle and Li dendrites growth	introducing too much materials
<b>MOF@PVDF-HFP</b>	facile preparation process, good flexibility, adjustable thickness, simultaneously inhibiting polysulfides shuttle and Li dendrites growth	small size of the separator

(1) For suppressing the polysulfides shuttle, both the repulsion effect by Coulombic interactions and the blocking effect by physical barriers can effectively mitigate the diffusion of polysulfide anions. However, constructing a “polysulfides-phobic” interface via Coulombic interactions may need a series of pre-treatment operations, while building a physical barrier just need choose a stable material with smaller pore size than the chain size of polysulfides. In this case, it seems that employing the physical barrier to prevent the polysulfides diffusion will be more efficient;

(2) As to inhibiting the growth of lithium dendrites, it can be realized by introducing a functional layer composed of porous materials with uniform pore size distribution, which can aid in regulating the uniform electrodeposition of lithium ions. Employing the materials with smaller size is better than the one with bigger size, since properly small size can confine the transport of anions to facilitate high mobility of lithium ions, which is in favour of a higher attainable state of charge at high rates. Certainly, the pore size of the materials should bigger than the size of lithium ions to avoid the negative influence on the transfer of lithium ions.

(3) From a practical point of view, the materials with small and uniform pore size seem to be more reliable to develop the multifunctional separators for Li-S batteries, as they can simultaneously inhibit polysulfides shuttle by physical barrier and suppress the lithium dendrites growth through facilitating homogenous Li-ion fluxes. In this case, the MOF-based separator is the best one for the practical Li-S batteries. However, the MOF-based membranes prepared by filtration method have small size, which is limited by the experimental facility. Considering the practical applications, efficient, low cost and easy to scale up technologies for preparing high quality separators should be further developed.

To sum up, the fundamental understanding with substantial evidences of this research provides a new way of thinking to develop advanced Li-S batteries.

# List of research results

## **JOURNAL PAPER**

First-author related to this Ph.D. thesis

- [1] **He Yibo**, Qiao Yu, Chang Zhi, Cao Xin, Jia Min, He Ping, and Zhou Haoshen,\*  
Developing a “polysulfide-phobic” strategy to restrain shuttle effect in lithium-sulfur  
batteries. *Angewandte Chemie International Edition*, 2019, DOI:  
10.1002/anie.201906055 and 10.1002/ange.201906055
- [2] **He Yibo**, Chang Zhi, Wu Shichao, Qiao Yu, Bai Songyan, Jiang Kezhu, He Ping,  
and Zhou Haoshen,\* Simultaneously inhibiting lithium dendrites growth and  
polysulfides shuttle by a flexible MOF-based membrane in Li-S batteries. *Advanced  
Energy Materials*, 2018, 8, 1802130.
- [3] **He Yibo**, Wu Shichao, Qi Li, and Zhou Haoshen,\* Designing a multifunctional  
separator for high-performance lithium-sulfur batteries. Submitted to *Small*.

Other publications

- [1] **He Yibo**, Qiao Yu, Chang Zhi, and Zhou Haoshen,\* The potential of electrolyte filled  
MOF membranes as ionic sieves in rechargeable batteries. *Energy & Environmental  
Science*, 2019, DOI: 10.1039/C8EE03651A
- [2] **He Yibo**, Chang Zhi, Wu Shichao, and Zhou Haoshen,\* Effective strategies for long-  
cycle life lithium-sulfur batteries. *Journal of Materials Chemistry A*, 2018, 6, 6155-  
6182.
- [3] **He Yibo**, Qiao Yu, and Zhou Haoshen,\*Recent advances in functional modification  
of separators in lithium-sulfur batteries. *Dalton Transactions*, 2018, 47, 6881-6887.
- [4] **He Yibo**, Bai Songyan, Chang Zhi, Li Qi, Qiao Yu, and Zhou Haoshen,\* Porous

- hybrid aerogels with ultrahigh sulfur loading for lithium-sulfur batteries. *Journal of Materials Chemistry A*, 2018, 6, 9032-9040.
- [5] Qiao Yu,<sup>†</sup> **He Yibo**,<sup>†</sup> Jiang Kezhu, Liu Yang, Li Xiang, Jia Min, Guo Shaohua, and Zhou Haoshen,\* High-voltage Li-ion full-cells with ultralong term cycle life at elevated temperature. *Advanced Energy Materials*, 2018, 8, 1802322. († contributed equally)
- [6] Qiao Yu,<sup>†</sup> **He Yibo**,<sup>†</sup> Wu Shichao, Jiang Kezhu, Li Xiang, Guo Shaohua, He Ping, and Zhou Haoshen,\* MOF-based separator in an Li-O<sub>2</sub> battery: an effective strategy to restrain the shuttling of dual redox mediators. *ACS Energy Letters*, 2018, 3, 463-468. († contributed equally)
- [7] Chang Zhi, **He Yibo**, Deng Han, Li Xiang, Wu Shichao, Qiao Yu, Zhou Haoshen,\* A multi-functional silly-putty nanocomposite spontaneously repairs cathode composite for advanced Li-S batteries. *Advanced Functional Materials*, 2018, 28, 1804777.
- [8] Wu Shichao, Qiao Yu, Jiang Kezhu, **He Yibo**, Guo Shaohua, and Zhou Haoshen,\* Tailoring sodium anodes for stable sodium-oxygen batteries. *Advanced Functional Materials*, 2018, 28, 1706374.
- [9] Wu Shichao, Qiao Yu, Deng Han, **He Yibo**, and Zhou Haoshen,\* Minimizing the abnormal high-potential discharge process related to redox mediators in lithium-oxygen batteries. *The Journal of Physical Chemistry Letters*, 2018, 9, 6761-6766.
- [10] Bai Songyan, Sun Yang, Yi Jin, **He Yibo**, and Zhou Haoshen,\* High-power Li-metal anode by metal-organic framework modified electrolyte. *Joule* 2018, 2, 2117-2132.
- [11] Qiao Yu, Jiang Kezhu, Li Xiang, Deng Han, **He Yibo**, and Zhou Haoshen,\* A hybrid electrolytes design for capacity-equivalent dual-graphite battery with superior long-term cycle life. *Advanced Energy Materials*, 2018, 8, 1801120.

## Acknowledgements

When I first came to the University of Tsukuba in 2016, I felt three years was a long time and I also worried deeply about my doctoral research. Unconsciously, the study of doctoral candidate is coming to end now. Looking back over the past three year, although I met a lot of difficulties in both study and life, I also get some good results, which can't achieve without the kind help of many people. At the final moments of preparing this thesis, I would like to express my heartfelt gratitude to all those who have helped me generously during the three years.

First and foremost, I would like to sincerely appreciate my doctoral supervisor Prof. Haoshen Zhou (a professor of University of Tsukuba and a principle investigator of National Institute of Advanced Industrial Science and Technology), who spent countless hours training and guiding me, offering help as much as possible when needed. During the past three years, Prof. Zhou's patience, encouragement and support greatly encouraged me. Without his illuminating instructions and expert guidance, the thesis is difficult to reach its present form. Furthermore, Prof. Zhou always shared his wealth of knowledge and experience to every student, which undoubtedly benefit me a lot and also will be a huge treasure in my career.

I would also express my heartfelt appreciations to my sub-supervisors Prof. Masayoshi Ishida, Assistant Prof. Hirohisa Aki, and Assistant Prof. Nobuko Hanada, from university of Tsukuba. When I entered the University of Tsukuba, all of them offered their selfless assistance to my study. In addition, many thanks for the valuable suggestions from Prof. Keiichi Okajima, Prof. Masayoshi Ishida and Assistant Prof. Hirohisa Aki of University of Tsukuba as wel as Dr. Hirokazu Kitaura of AIST in the presentation of this graduation thesis.

I feel sincerely grateful to all my group members: Dr. Yarong Wang, Dr. Shaohua Guo, Dr Jin Yi, Dr. Yang Sun, Dr. Shichao Wu, Dr. Songyan Bai, Dr. Qi Li, Dr. Yang

Liu, Dr. Yu Qiao, Mr. Xiang Li, Ms. Min Jia, Mr. Han Deng, Mr. Zhi Chang, Mr. Xin Cao and Mr. Huijun Yang. All of them gave their kind help to me in both study and life. In particular, I sincerely appreciate Dr. Shaohua Guo and Dr. Qi Li, since they gave me a lot of valuable advices and kind help when I applied to the University of Tsukuba. At the same time, I would also keep on my special thanks to Dr. Songyan Bai and Dr. Shichao Wu, who helped me start my initial experimental researches on lithium-sulfur batteries and made progress in my research work. In addition, many thanks to the help from my classmate, Mr. Xiang Li. We entered the University of Tsukuba together in 2016 to pursue our PhD degrees under the supervision of Prof. Haoshen Zhou.

Many thanks are wished to give the members, Dr. Hirofumi Matsuda, Dr. Hirokazu Kitaura, Dr. Eunjoo Yoo, Mr. Jun Okagaki and Okita-san, who come from the Energy Interface Technology Group of National Institute of Advanced Industrial Science and Technology (AIST). When I had difficulties in the experiment, they always offered me friendly help.

I would like to express my thanks to Mr. Kezhu Jiang, Ms. Lingling Wang, Mr. Feilong Qiu and Mr. Pengfei Wang from Nanjing University as well as Mr. Kai Han from Northwestern Polytechnical University to help me obtain XPS and Zeta potential data. Dr. Shengyao Wang from National Institute for Materials Science (NIMS) is also grateful for helping me to obtain BET data.

I would also sincerely appreciate financial support by the SPRING-ALCA from the Japan Science and Technology Agency (JST) and scholarship from China Scholarship Council (201606870051).

Last, but definitely not least, I am extremely grateful for my parents. Their support and understanding inspire me all through these years and also will give me more confidence in future life.

## REFERENCES

1. A. Manthiram, Y. Fu, S.-H. Chung, C. Zu and Y.-S. Su, *Chem. Rev.*, 2014, **114**, 11751-11787.
2. H. Danuta and U. Juliusz, *Journal*, 1962. U.S. Patent No. 3043896.
3. M. Armand and J.-M. Tarascon, *Nature*, 2008, **451**, 652.
4. Y. X. Yin, S. Xin, Y. G. Guo and L. J. Wan, *Angew. Chem. Int. Ed.*, 2013, **52**, 13186-13200.
5. B. Dunn, H. Kamath and J.-M. Tarascon, *Science*, 2011, **334**, 928-935.
6. S. Evers and L. F. Nazar, *Accounts Chem. Res.*, 2012, **46**, 1135-1143.
7. Y. Yue and H. Liang, *Small Methods*, 2018, **2**, 1800056.
8. T. Tao, S. Lu, Y. Fan, W. Lei, S. Huang and Y. Chen, *Adv. Mater.*, 2017, **29**, 1700542.
9. R. Cao, W. Xu, D. Lv, J. Xiao and J. G. Zhang, *Adv. Energy Mater.*, 2015, **5**, 1402273.
10. H. Lee, M. Yanilmaz, O. Toprakci, K. Fu and X. Zhang, *Energy Environ. Sci.*, 2014, **7**, 3857-3886.
11. P. Arora and Z. Zhang, *Chem. Rev.*, 2004, **104**, 4419-4462.
12. J. Scheers, S. Fantini and P. Johansson, *J. Power Sources*, 2014, **255**, 204-218.
13. J. B. Goodenough and Y. Kim, *Chem. Mater.*, 2009, **22**, 587-603.
14. G. Li, Z. Li, B. Zhang and Z. Lin, *Front. Energy Res.*, 2015, **3**, 5.
15. L. Yuan, J. Feng, X. Ai, Y. Cao, S. Chen and H. Yang, *Electrochem. Commun.*, 2006, **8**, 610-614.
16. Y. Yan, Y.-X. Yin, S. Xin, J. Su, Y.-G. Guo and L.-J. Wan, *Electrochim. Acta*, 2013, **91**, 58-61.

17. J.-W. Park, K. Yamauchi, E. Takashima, N. Tachikawa, K. Ueno, K. Dokko and M. Watanabe, *J. Phys. Chem. C*, 2013, **117**, 4431-4440.
18. H.-S. Ryu, H.-J. Ahn, K.-W. Kim, J.-H. Ahn and J.-Y. Lee, *J. Power Sources*, 2006, **153**, 360-364.
19. J. Hassoun and B. Scrosati, *Angew. Chem. Int. Ed.*, 2010, **49**, 2371-2374.
20. J. Przystyluski, M. Siekierski and W. Wieczorek, *Electrochim. Acta*, 1995, **40**, 2101-2108.
21. T. Kobayashi, Y. Imade, D. Shishihara, K. Homma, M. Nagao, R. Watanabe, T. Yokoi, A. Yamada, R. Kanno and T. Tatsumi, *J. Power Sources*, 2008, **182**, 621-625.
22. T. Yamada, S. Ito, R. Omoda, T. Watanabe, Y. Aihara, M. Agostini, U. Ulissi, J. Hassoun and B. Scrosati, *J. Electrochem. Soc.*, 2015, **162**, A646-A651.
23. A. Hayashi, T. Ohtomo, F. Mizuno, K. Tadanaga and M. Tatsumisago, *Electrochem. Commun.*, 2003, **5**, 701-705.
24. S.-H. Chung and A. Manthiram, *Adv. Mater.*, 2019, **0**, 1901125.
25. Y. Yang, G. Zheng and Y. Cui, *Chem. Soc. Rev.*, 2013, **42**, 3018-3032.
26. D.-W. Wang, Q. Zeng, G. Zhou, L. Yin, F. Li, H.-M. Cheng, I. R. Gentle and G. Q. M. Lu, *J. Mater. Chem. A*, 2013, **1**, 9382-9394.
27. R. Fang, S. Zhao, Z. Sun, D. W. Wang, H. M. Cheng and F. Li, *Adv. Mater.*, 2017, **29**, 1606823.
28. H.-J. Peng, J.-Q. Huang, X.-B. Cheng and Q. Zhang, *Adv. Energy Mater.*, 2017, **7**, 1700260.
29. L. Luo, S.-H. Chung and A. Manthiram, *Adv. Energy Mater.*, 2018, **8**, 1801014.
30. S.-H. Chung, C.-H. Chang and A. Manthiram, *ACS Nano*, 2016, **10**, 10462-10470.
31. L. Ji, M. Rao, H. Zheng, L. Zhang, Y. Li, W. Duan, J. Guo, E. J. Cairns and Y. Zhang, *J. Am. Chem. Soc.*, 2011, **133**, 18522-18525.

32. R. Fang, S. Zhao, Z. Sun, D.-W. Wang, H.-M. Cheng and F. Li, *Adv. Mater.*, 2017, **29**, 1606823.
33. S. Moon, Y. H. Jung, W. K. Jung, D. S. Jung, J. W. Choi and D. K. Kim, *Adv. Mater.*, 2013, **25**, 6547-6553.
34. Y. Fu, Y.-S. Su and A. Manthiram, *Angew. Chem. Int. Ed.*, 2013, **52**, 6930-6935.
35. R. Yu, S.-H. Chung, C.-H. Chen and A. Manthiram, *J. Mater. Chem. A*, 2018, **6**, 24841-24847.
36. G. Li, S. Wang, Y. Zhang, M. Li, Z. Chen and J. Lu, *Adv. Mater.*, 2018, **30**, 1705590.
37. X. Yang, X. Li, K. Adair, H. Zhang and X. Sun, *Electrochem. Energy Rev.*, 2018, **1**, 239-293.
38. S. H. Chung, C. H. Chang and A. Manthiram, *Adv. Funct. Mater.*, 2018, **28**, 1801188.
39. M. Liu, F. Ye, W. Li, H. Li and Y. Zhang, *Nano Res.*, 2016, **9**, 94-116.
40. Y. He, Z. Chang, S. Wu and H. Zhou, *J. Mater. Chem. A*, 2018, **6**, 6155-6182.
41. Y. He, Y. Qiao and H. Zhou, *Dalton Trans.*, 2018, **47**, 6881-6887.
42. S. H. Chung, P. Han, R. Singhal, V. Kalra and A. Manthiram, *Adv. Energy Mater.*, 2015, **5**, 1500738.
43. Y. V. Mikhaylik and J. R. Akridge, *J. Electrochem. Soc.*, 2003, **150**, A306-A311.
44. Y. V. Mikhaylik and J. R. Akridge, *J. Electrochem. Soc.*, 2004, **151**, A1969-A1976.
45. S.-H. Chung, R. Singhal, V. Kalra and A. Manthiram, *J. Phys. Chem. Lett.*, 2015, **6**, 2163-2169.
46. M. A. Pope and I. A. Aksay, *Adv. Energy Mater.*, 2015, **5**, 1500124.
47. J. Gao, M. A. Lowe, Y. Kiya and H. c. D. Abruña, *J. Phys. Chem. C*, 2011, **115**, 25132-25137.
48. Q. Zhang, F. Li, J. Q. Huang and H. Li, *Adv. Funct. Mater.*, 2018, **28**, 1804589.

49. D. Bresser, S. Passerini and B. Scrosati, *Chem. Commun.*, 2013, **49**, 10545-10562.
50. L. Luo, S.-H. Chung and A. Manthiram, *J. Mater. Chem. A*, 2018, **6**, 7659-7667.
51. J. Sun, Y. Huang, W. Wang, Z. Yu, A. Wang and K. Yuan, *Electrochem. Commun.*, 2008, **10**, 930-933.
52. L. Chen and L. L. Shaw, *J. Power Sources*, 2014, **267**, 770-783.
53. S.-H. Chung and A. Manthiram, *Joule*, 2018, **2**, 710-724.
54. S. H. Chung, K. Y. Lai and A. Manthiram, *Adv. Mater.*, 2018, **30**, 1805571.
55. S. H. Chung and A. Manthiram, *Adv. Mater.*, 2018, **30**, 1705951.
56. M. S. Whittingham, *Science*, 1976, **192**, 1126-1127.
57. X. B. Cheng, R. Zhang, C. Z. Zhao and Q. Zhang, *Chem. Rev.*, 2017, **117**, 10403-10473.
58. X. Ji, K. T. Lee and L. F. Nazar, *Nat. Mater.*, 2009, **8**, 500.
59. C. Zhang, H. B. Wu, C. Yuan, Z. Guo and X. W. Lou, *Angew. Chem. Int. Ed.*, 2012, **51**, 9592-9595.
60. C. Hu, H. Chen, Y. Shen, D. Lu, Y. Zhao, A. H. Lu, X. Wu, W. Lu and L. Chen, *Nat. Commun.*, 2017, **8**, 479.
61. L. Kong, X. Chen, B. Q. Li, H. J. Peng, J. Q. Huang, J. Xie and Q. Zhang, *Adv. Mater.*, 2018, **30**, 1705219.
62. Z. Yuan, H.-J. Peng, T.-Z. Hou, J.-Q. Huang, C.-M. Chen, D.-W. Wang, X.-B. Cheng, F. Wei and Q. Zhang, *Nano Lett.*, 2016, **16**, 519-527.
63. X. Gu, C.-j. Tong, B. Wen, L.-m. Liu, C. Lai and S. Zhang, *Electrochim. Acta*, 2016, **196**, 369-376.
64. E. T. Kim, J. Park, C. Kim, A. G. Simmonds, Y.-E. Sung, J. Pyun and K. Char, *ACS Macro Lett.*, 2016, **5**, 471-475.
65. W. J. Chung, J. J. Griebel, E. T. Kim, H. Yoon, A. G. Simmonds, H. J. Ji, P. T. Dirlam, R. S. Glass, J. J. Wie and N. A. Nguyen, *Nat. Chem.*, 2013, **5**, 518.

66. H. Kim, J. Lee, H. Ahn, O. Kim and M. J. Park, *Nat. Commun.*, 2015, **6**, 7278.
67. W. Li, H. Yao, K. Yan, G. Zheng, Z. Liang, Y.-M. Chiang and Y. Cui, *Nat. Commun.*, 2015, **6**, 7436.
68. G. Ma, Z. Wen, M. Wu, C. Shen, Q. Wang, J. Jin and X. Wu, *Chem. Commun.*, 2014, **50**, 14209-14212.
69. X. Chen, T.-Z. Hou, B. Li, C. Yan, L. Zhu, C. Guan, X.-B. Cheng, H.-J. Peng, J.-Q. Huang and Q. Zhang, *Energy Storage Mater.*, 2017, **8**, 194-201.
70. K. Leung, Y. Qi, K. R. Zavadil, Y. S. Jung, A. C. Dillon, A. S. Cavanagh, S.-H. Lee and S. M. George, *J. Am. Chem. Soc.*, 2011, **133**, 14741-14754.
71. Y. Lu, K. Korf, Y. Kambe, Z. Tu and L. A. Archer, *Angew. Chem. Int. Ed.*, 2014, **53**, 488-492.
72. Y. Lu, S. K. Das, S. S. Moganty and L. A. Archer, *Adv. Mater.*, 2012, **24**, 4430-4435.
73. Y. Lu, Z. Tu and L. A. Archer, *Nat. Mater.*, 2014, **13**, 961.
74. G. Zheng, S. W. Lee, Z. Liang, H. W. Lee, K. Yan, H. Yao, H. Wang, W. Li, S. Chu and Y. Cui, *Nat. Nanotechnol.*, 2014, **9**, 618-623.
75. A. C. Kozen, C. F. Lin, A. J. Pearse, M. A. Schroeder, X. Han, L. Hu, S. B. Lee, G. W. Rubloff and M. Noked, *ACS Nano*, 2015, **9**, 5884-5892.
76. W. Sun, X. Ou, X. Yue, Y. Yang, Z. Wang, D. Rooney and K. Sun, *Electrochim. Acta*, 2016, **207**, 198-206.
77. J.-Q. Huang, Q. Zhang, H.-J. Peng, X.-Y. Liu, W.-Z. Qian and F. Wei, *Energy Environ. Sci.*, 2014, **7**, 347-353.
78. H. Yao, K. Yan, W. Li, G. Zheng, D. Kong, Z. W. Seh, V. K. Narasimhan, Z. Liang and Y. Cui, *Energy Environ. Sci.*, 2014, **7**, 3381-3390.
79. S.-H. Chung and A. Manthiram, *Adv. Funct. Mater.*, 2014, **24**, 5299-5306.

80. H. Wang, W. Zhang, H. Liu and Z. Guo, *Angew. Chem. Int. Ed.*, 2016, **55**, 3992-3996.
81. J. Zhu, Y. Ge, D. Kim, Y. Lu, C. Chen, M. Jiang and X. Zhang, *Nano Energy*, 2016, **20**, 176-184.
82. Z. A. Ghazi, X. He, A. M. Khattak, N. A. Khan, B. Liang, A. Iqbal, J. Wang, H. Sin, L. Li and Z. Tang, *Adv. Mater.*, 2017, **29**, 1606817.
83. W. Cai, G. Li, F. He, L. Jin, B. Liu and Z. Li, *J. Power Sources*, 2015, **283**, 524-529.
84. S. H. Chung, P. Han, R. Singhal, V. Kalra and A. Manthiram, *Adv. Energy Mater.*, 2015, **5**, 1500738.
85. Q. Wang, Z. Wen, J. Yang, J. Jin, X. Huang, X. Wu and J. Han, *J. Power Sources*, 2016, **306**, 347-353.
86. Z. Wang, J. Zhang, Y. Yang, X. Yue, X. Hao, W. Sun, D. Rooney and K. Sun, *J. Power Sources*, 2016, **329**, 305-313.
87. Y. Yang, W. Sun, J. Zhang, X. Yue, Z. Wang and K. Sun, *Electrochim. Acta*, 2016, **209**, 691-699.
88. J. Wang, Y. Yang and F. Kang, *Electrochim. Acta*, 2015, **168**, 271-276.
89. Z. Zhang, G. Wang, Y. Lai and J. Li, *J. Alloys Compounds*, 2016, **663**, 501-506.
90. G. Zhou, L. Li, D. W. Wang, X. Y. Shan, S. Pei, F. Li and H. M. Cheng, *Adv. Mater.*, 2015, **27**, 641-647.
91. J.-Q. Huang, T.-Z. Zhuang, Q. Zhang, H.-J. Peng, C.-M. Chen and F. Wei, *ACS Nano*, 2015, **9**, 3002-3011.
92. X. Wang, Z. Wang and L. Chen, *J. Power Sources*, 2013, **242**, 65-69.
93. W. Liu, J. Jiang, K. R. Yang, Y. Mi, P. Kumaravadivel, Y. Zhong, Q. Fan, Z. Weng, Z. Wu and J. J. Cha, *Pro. National Academy Sci.*, 2017, **114**, 3578-3583.

94. J. Zhu, C. Chen, Y. Lu, J. Zang, M. Jiang, D. Kim and X. Zhang, *Carbon*, 2016, **101**, 272-280.
95. R. Zhang, X. B. Cheng, C. Z. Zhao, H. J. Peng, J. L. Shi, J. Q. Huang, J. Wang, F. Wei and Q. Zhang, *Adv. Mater.*, 2016, **28**, 2155-2162.
96. X. Zhou, Q. Liao, J. Tang, T. Bai, F. Chen and J. Yang, *J. Electroanal. Chem.*, 2016, **768**, 55-61.
97. Y.-S. Su and A. Manthiram, *Nat. Commun.*, 2012, **3**, 1166.
98. W. Li, J. Hicks-Garner, J. Wang, J. Liu, A. F. Gross, E. Sherman, J. Graetz, J. J. Vajo and P. Liu, *Chem. Mater.*, 2014, **26**, 3403-3410.
99. T. Lee, W.-K. Kim, Y. Lee, M.-H. Ryou and Y. M. Lee, *Macromolecular Res.*, 2014, **22**, 1190-1195.
100. J. Lee, C.-L. Lee, K. Park and I.-D. Kim, *J. Power Sources*, 2014, **248**, 1211-1217.
101. K. Dong, S. Wang, H. Zhang and J. Wu, *Mater. Research Bulletin*, 2013, **48**, 2079-2083.
102. Y. Choi, B. Jung, D. Lee, J. Jeong, K. Kim, H. Ahn, K. Cho and H. Gu, *Physica Scripta*, 2007, **2007**, 62.
103. Z. Zhang, Y. Lai, Z. Zhang, K. Zhang and J. Li, *Electrochim. Acta*, 2014, **129**, 55-61.
104. R. Song, R. Fang, L. Wen, Y. Shi, S. Wang and F. Li, *J. Power Sources*, 2016, **301**, 179-186.
105. Z. W. Seh, Q. Zhang, W. Li, G. Zheng, H. Yao and Y. Cui, *Chem. Sci.*, 2013, **4**, 3673-3677.
106. Z. Jin, K. Xie, X. Hong, Z. Hu and X. Liu, *J. Power Sources*, 2012, **218**, 163-167.
107. Z. Hao, L. Yuan, Z. Li, J. Liu, J. Xiang, C. Wu, R. Zeng and Y. Huang, *Electrochim. Acta*, 2016, **200**, 197-203.
108. X. Yu, J. Joseph and A. Manthiram, *J. Mater. Chem. A*, 2015, **3**, 15683-15691.

109. J. Conder, S. Urbonaite, D. Streich, P. Novák and L. Gubler, *RSC Adv.*, 2015, **5**, 79654-79660.
110. J. Conder, A. Forner-Cuenca, E. M. Gubler, L. Gubler, P. Novak and S. Trabesinger, *ACS Appl. Mater. Interfaces*, 2016, **8**, 18822-18831.
111. M. Gu, J. Lee, Y. Kim, J. S. Kim, B. Y. Jang, K. T. Lee and B.-S. Kim, *RSC Adv.*, 2014, **4**, 46940-46946.
112. W. Li, Q. Zhang, G. Zheng, Z. W. Seh, H. Yao and Y. Cui, *Nano Lett.*, 2013, **13**, 5534-5540.
113. G. Ma, Z. Wen, Q. Wang, C. Shen, P. Peng, J. Jin and X. Wu, *J. Power Sources*, 2015, **273**, 511-516.
114. Y. Cui, Z. Wen, X. Liang, Y. Lu, J. Jin, M. Wu and X. Wu, *Energy Environ. Sci.*, 2012, **5**, 7893-7897.
115. G. Ma, Z. Wen, J. Jin, M. Wu, X. Wu and J. Zhang, *J. Power Sources*, 2014, **267**, 542-546.
116. Y. He, Y. Bai, X. Yang, J. Zhang, L. Kang, H. Xu, F. Shi, Z. Lei and Z.-H. Liu, *J. Power Sources*, 2016, **317**, 10-18.
117. P. G. Bruce, S. A. Freunberger, L. J. Hardwick and J.-M. Tarascon, *Nat. Mater.*, 2012, **11**, 19.
118. R. F. Service, *Science*, 2018, **359**, 1080.
119. Z. W. Seh, Y. Sun, Q. Zhang and Y. Cui, *Chem. Soc. Rev.*, 2016, **45**, 5605-5634.
120. Y. Zhao, Y. Ye, F. Wu, Y. Li, L. Li and R. Chen, *Adv. Mater.*, 2019, **31**, 1806532.
121. G. Zhou, S. Pei, L. Li, D. W. Wang, S. Wang, K. Huang, L. C. Yin, F. Li and H. M. Cheng, *Adv. Mater.*, 2014, **26**, 625-631.
122. R. Fang, S. Zhao, Z. Sun, D. W. Wang, H. M. Cheng and F. Li, *Adv. Mater.*, 2017, **29**, 1606823.

123. C. C. Su, M. He, R. Amine, Z. Chen and K. Amine, *Angew. Chem. Int. Ed.*, 2018, **130**, 12209-12212.
124. W. Chen, T. Lei, W. Lv, Y. Hu, Y. Yan, Y. Jiao, W. He, Z. Li, C. Yan and J. Xiong, *Adv. Mater.*, 2018, **30**, 1804084.
125. H. Yang, C. Guo, J. Chen, A. Naveed, J. Yang, Y. Nuli and J. Wang, *Angew. Chem. Int. Ed.*, 2019, **13**, 801-809.
126. A. Shyamsunder, W. Beichel, P. Klose, Q. Pang, H. Scherer, A. Hoffmann, G. K. Murphy, I. Krossing and L. F. Nazar, *Angew. Chem. Int. Ed.*, 2017, **56**, 6192-6197.
127. H. Pan, J. Chen, R. Cao, V. Murugesan, N. N. Rajput, K. S. Han, K. Persson, L. Estevez, M. H. Engelhard and J.-G. Zhang, *Nat. Energy*, 2017, **2**, 813.
128. X. Li and X. Sun, *Adv. Funct. Mater.*, 2018, **28**, 1801323.
129. Z. Xu, J. Wang, J. Yang, X. Miao, R. Chen, J. Qian and R. Miao, *Angew. Chem. Int. Ed.*, 2016, **55**, 10372-10375.
130. G. Hu, Z. Sun, C. Shi, R. Fang, J. Chen, P. Hou, C. Liu, H. M. Cheng and F. Li, *Adv. Mater.*, 2017, **29**, 1603835.
131. J. Zhang, H. Huang, J. Bae, S. H. Chung, W. Zhang, A. Manthiram and G. Yu, *Small Methods*, 2018, **2**, 1700279.
132. X. Gao, X. Yang, M. Li, Q. Sun, J. Liang, J. Luo, J. Wang, W. Li, J. Liang and Y. Liu, *Adv. Funct. Mater.*, 2019, **29**, 1806724.
133. J. Song, M. L. Gordin, T. Xu, S. Chen, Z. Yu, H. Sohn, J. Lu, Y. Ren, Y. Duan and D. Wang, *Angew. Chem. Int. Ed.*, 2015, **127**, 4399-4403.
134. Q. Pang, D. Kundu, M. Cuisinier and L. Nazar, *Nat. Commun.*, 2014, **5**, 4759.
135. R. Demir-Cakan, M. Morcrette, F. Nouar, C. Davoisne, T. Devic, D. Gonbeau, R. Dominko, C. Serre, G. Férey and J.-M. Tarascon, *J. Am. Chem. Soc.*, 2011, **133**, 16154-16160.
136. S. Bai, X. Liu, K. Zhu, S. Wu and H. Zhou, *Nat. Energy*, 2016, **1**, 16094.

137. Z. Chang, Y. He, H. Deng, X. Li, S. Wu, Y. Qiao, P. Wang and H. Zhou, *Adv. Funct. Mater.*, 2018, **28**, 1804777.
138. Y. Cheng, C. He, C. Xiao, J. Ding, X. Zhuang, Y. Huang and X. Chen, *Biomacromolecules*, 2012, **13**, 2053-2059.
139. K. Liu, X. Yao and L. Jiang, *Chem. Soc. Rev.*, 2010, **39**, 3240-3255.
140. K. Liao, P. Mao, N. Li, M. Han, J. Yi, P. He, Y. Sun and H. Zhou, *J. Mater. Chem. A*, 2016, **4**, 5406-5409.
141. Y. He, X. Yang, Y. Bai, J. Zhang, L. Kang, Z. Lei and Z.-H. Liu, *Electrochimica Acta*, 2015, **178**, 312-320.
142. C. Wu, X. Lu, L. Peng, K. Xu, X. Peng, J. Huang, G. Yu and Y. Xie, *Nat. Commun.*, 2013, **4**, 2431.
143. W. Qian, Q. Gao, W. Tian, H. Zhang, Y. Tan and Z. Li, *J. Mater. Chem. A*, 2016, **4**, 15140-15147.
144. J. F. Li, Y. F. Huang, Y. Ding, Z. L. Yang, S. B. Li, X. S. Zhou, F. R. Fan, W. Zhang, Z. Y. Zhou, B. Ren, *Nature*, 2010, **464**, 392;
145. P. G. Bruce, J. Evans and C. A. Vincent, *Solid State Ionics*, 1988, **28**, 918-922.
146. J. Evans, C. A. Vincent and P. G. Bruce, *Polymer*, 1987, **28**, 2324-2328.
147. C. Wu, X. Lu, L. Peng, K. Xu, X. Peng, J. Huang, G. Yu and Y. Xie, *Nat. Commun.*, 2013, **4**, 2431.
148. C. Sourisseau, R. Cavagnat, M. Fouassier, J. L. Tirado, J. Morales, *J. Mol. Struct.* 1995, **348**, 107- 110.
149. H. J. Peng, Z. W. Zhang, J. Q. Huang, G. Zhang, J. Xie, W. T. Xu, J. L. Shi, X. Chen, X. B. Cheng and Q. Zhang, *Adv. Mater*, 2016, **28**, 9551-9558.
150. W. Liu, Y. Mi, Z. Weng, Y. Zhong, Z. Wu and H. Wang, *Chem. Sci.*, 2017, **8**, 4285-4291.

151. K. M. Diederichsen, E. J. McShane and B. D. McCloskey, *ACS Energy Lett.*, 2017, **2**, 2563-2575.
152. E. M. Miner, S. S. Park and M. Dinca, *J. Am. Chem. Soc.*, 2019, **141**, 4422-4427.
153. S. Bai, Y. Sun, J. Yi, Y. He, Y. Qiao and H. Zhou, *Joule*, 2018, **2**, 2117-2132.
154. Q. Xu, C. Wei, L. Fan, S. Peng, W. Xu and J. Xu, *Cellulose*, 2017, **24**, 1889-1899.
155. M. Agostini, B. Scrosati and J. Hassoun, *Adv. Energy Mater.*, 2015, **5**, 1500481.
156. L. Ma, P. Nath, Z. Tu, M. Tikekar and L. A. Archer, *Chem. Mater.*, 2016, **28**, 5147-5154.
157. N. N. Rajput, V. Murugesan, Y. Shin, K. S. Han, K. C. Lau, J. Chen, J. Liu, L. A. Curtiss, K. T. Mueller and K. A. Persson, *Chem. Mater.*, 2017, **29**, 3375-3379.
158. C. M. López, J. T. Vaughey and D. W. Dees, *J. Electrochem. Soc.*, 2009, **156**, A726-A729.
159. K.-S. Lin, A. K. Adhikari, C.-N. Ku, C.-L. Chiang and H. Kuo, *Inter. Hydro. Energy*, 2012, **37**, 13865-13871.
160. A. M. Stephan, K. S. Nahm, M. A. Kulandainathan, G. Ravi and J. Wilson, *European Polymer J.*, 2006, **42**, 1728-1734.
161. D. Saikia and A. Kumar, *Electrochim. Acta*, 2004, **49**, 2581-2589.
162. S. Loera-Serna, M. A. Oliver-Tolentino, M. de Lourdes López-Núñez, A. Santana-Cruz, A. Guzmán-Vargas, R. Cabrera-Sierra, H. I. Beltrán and J. Flores, *J. Alloys Compounds*, 2012, **540**, 113-120.
163. G. G. da Silva, F. Machado, S. A. Junior and E. Padrón-Hernández, *J. Solid State Chem.*, 2017, **253**, 1-5.
164. V. K. Singh and R. K. Singh, *J. Mater. Chem. A*, 2015, **3**, 7305-7318.
165. G. Peng, X. Zhao, Z. Zhan, S. Ci, Q. Wang, Y. Liang and M. Zhao, *RSC Adv.*, 2014, **4**, 16849-16854.

166. Y. Feng, W. Li, Y. Hou, Y. Yu, W. Cao, T. Zhang and W. Fei, *J. Mater. Chem. A*, 2015, **3**, 1250-1260.
167. M. R. Azhar, H. R. Abid, H. Sun, V. Periasamy, M. O. Tadé and S. Wang, *J. Colloid Inter. Sci.*, 2016, **478**, 344-352.
168. T. Toyao, K. Liang, K. Okada, R. Ricco, M. J. Styles, Y. Tokudome, Y. Horiuchi, A. J. Hill, M. Takahashi and M. Matsuoka, *Inorg. Chem. Front.*, 2015, **2**, 434-441.
169. S. Das, S. Majumder and R. Katiyar, *J. Power Sources*, 2005, **139**, 261-268.
170. J. Wang, F. Lin, H. Jia, J. Yang, C. W. Monroe and Y. NuLi, *Angew. Chem. Int. Ed.*, 2014, **53**, 10099-10104.
171. Z. Wang, B. Wang, Y. Yang, Y. Cui, Z. Wang, B. Chen and G. Qian, *ACS Appl. Mater. Interfaces*, 2015, **7**, 20999-21004.
172. Y. Zhou, C. Zhou, Q. Li, C. Yan, B. Han, K. Xia, Q. Gao and J. Wu, *Adv. Mater.*, 2015, **27**, 3774-3781.
173. J. Zhou, R. Li, X. Fan, Y. Chen, R. Han, W. Li, J. Zheng, B. Wang and X. Li, *Energy Environ. Sci.*, 2014, **7**, 2715-2724.
174. Z. Zhao, S. Wang, R. Liang, Z. Li, Z. Shi and G. Chen, *J. Mater. Chem. A*, 2014, **2**, 13509-13512.
175. S. N. Talapaneni, T. H. Hwang, S. H. Je, O. Buyukcakir, J. W. Choi and A. Coskun, *Angew. Chem. Int. Ed.*, 2016, **55**, 3106-3111.
176. J. Zheng, J. Tian, D. Wu, M. Gu, W. Xu, C. Wang, F. Gao, M. H. Engelhard, J.-G. Zhang and J. Liu, *Nano Lett.*, 2014, **14**, 2345-2352.
177. A. C. Kozen, C.-F. Lin, A. J. Pearse, M. A. Schroeder, X. Han, L. Hu, S.-B. Lee, G. W. Rubloff and M. Noked, *ACS Nano*, 2015, **9**, 5884-5892.
178. Y. Zang, F. Pei, J. Huang, Z. Fu, G. Xu and X. Fang, *Adv. Energy Mater.*, 2018, **8**, 1802052.

179. Z. Wang, M. Feng, H. Sun, G. Li, Q. Fu, H. Li, J. Liu, L. Sun, A. Mauger and C. M. Julien, *Nano Energy*, 2019, **59**, 390-398.
180. S. Tu, X. Chen, X. Zhao, M. Cheng, P. Xiong, Y. He, Q. Zhang and Y. Xu, *Adv. Mater.*, 2018, **30**, 1804581.
181. L. Z. Pei, J. F. Wang, X. X. Tao, S. B. Wang, Y. P. Dong, C. G. Fan, Q. F. Zhang, *Mater. Charact.*, 2011, **9**, 354-359.
182. M. Saranya, C. Santhosh, R. Ramachandran, P. Kollu, P. Saravanan, M. Vinoba, A. N. Grace, *Powder Tech.*, 2014, **252**, 25-32.
183. Y. Mao, G. Li, Y. Guo, Z. Li, C. Liang, X. Peng and Z. Lin, *Nat. Commun.*, 2017, **8**, 14628.
184. B. Peng, C. Feng, S. Liu, R. Zhang, *R. Catal. Today*, 2018, **314**, 122-128.
185. S. K. Chawla, N. Sankarraman, J. H. Payer, *J. Electron Spectrosc. Reiat. Phenom.*, 1992, **61**, 1-18.
186. H. Niu, S. Liu, Y. Cai, F. Wu, X. Zhao, *Micropor. Mesopor. Mater.*, 2016, **219**, 48-53.
187. F. Wu, S. Zhao, L. Chen, Y. Lu, Y. Su, Y. L. Bao, J. Wang, S. Chen, R. Chen, *Energy Storage Mater.*, 2018, **14**, 383-391.
188. R. Ponraj, A. G. Kannan, J. H. Ahn, D. W. Kim, *ACS Appl. Mater. Interfaces*, 2016, **8**, 4000-4006.